UNRAVELING PHOTONIC BANDS: CHARACTERIZATION OF SELF-COLLIMATION EFFECTS IN TWO-DIMENSIONAL PHOTONIC CRYSTALS

A Dissertation
Presented to
The Academic Faculty

By

Tsuyoshi Yamashita

In Partial Fulfillment
Of the Requirements for the Degree
Doctor of Philosophy in
Materials Science and Engineering

Georgia Institute of Technology
August, 2005

UNRAVELING PHOTONIC BANDS:
CHARACTERIZATION OF SELF-COLLIMATION EFFECTS IN TWO-DIMENSIONAL PHOTONIC CRYSTALS

Approved by:

Dr. Christopher Summers, Chairman
School of Materials Science and Engineering
Georgia Institute of Technology

Dr. James Meindl
Microelectronics Research Center
Georgia Institute of Technology

Dr. Mo Li
School of Materials Science and Engineering
Georgia Institute of Technology

Dr. Gee-Kung Chang
School of Electrical and Computer Engineering
Georgia Institute of Technology

Dr. Brent Carter
School of Materials Science and Engineering
Georgia Institute of Technology

Dr. Zhong Lin Wang
School of Materials Science and Engineering
Georgia Institute of Technology

Date Approved: June 14, 2005

It is my task to convince you *not* to turn away because you don't understand it. You see my physics students don't understand it... That is because *I* don't understand it. Nobody does.

-Richard P. Feynman, *QED, The Strange Theory of Light and Matter*

This thesis is dedicated to my wife, Zhuqing, who has faithfully and steadfastly supported me throughout the entirety of my pursuit of this degree. Without a doubt, this thesis would not have been possible without her diligent and constant care.

ACKNOWLEDGEMENT

The author would like to acknowledge his advisor, Dr. Christopher Summers, and the members of the committee, Dr. James Meindl, Dr. Gee-Kung Chang, Dr. Brent Carter, and Dr. Mo Li, for their invaluable support and input.

The author also thanks the National Science Foundation for the graduate research fellowship and the United States Army Research Office's Multi University Research Initiative contract DAAA 19-01-1-0603 for providing the funding which made the work in this thesis possible.

Special thanks go out to Dr. Won Park and his student Ethan Schronbrun at the University of Colorado, and Dr. Jeff King and Dr. Elton Graugnard at Georgia Tech for providing the support and facilities necessary to perform measurement on the fabricated structures. Special acknowledgements also go to Curtis Neff and Wenjie Mai for their assistance in the 3-D simulation and atomic force microscopy measurements, respectively.

The author would like to acknowledge the support of the Microelectronics Research Center (MiRC) cleanroom staff for their hard work and dedication for maintaining and servicing the equipment in the cleanroom which has allowed the research in this thesis possible. Special acknowledgement goes out to Vinh Nguyen and Devin Brown.

The author would also like to acknowledge Dr. Susumu Noda and the member's of his research group in the Kyoto University in Japan for hosting an exchange program during the second summer of my research. The experience and knowledge gained as well

as the discussions following the visit have been a continual source of motivation for the current work.

To conclude, the author would like to acknowledge the members of the faculty, staff, and students at Georgia Tech who have provided him support and valuable discussions on the work contained within this thesis.

TABLE OF CONTENTS

LIST OF TABLES

LIST OF FIGURES

SUMMARY

Photonic crystals, periodic dielectric structures that control photons in a similar way that atomic crystals control electrons, present opportunities for the unprecedented control of light. Photonic crystals display a wide gamut of properties, such as the photonic band gap, negative index of refraction, slow or stationary modes, and anomalous refraction and propagation effects. This thesis investigates the modeling, simulation, fabrication, and measurement of two-dimensional square lattice photonic crystals. An effective index model was developed to describe the propagation of electromagnetic waves in the media and applied to characterize the behavior of self-collimated beams to discern the effect of the photonic crystal on the evolution of the amplitude and phase of the propagating beam. Potential applications include optical interconnects and stand alone devices such as filters and lasers. Based on design parameters from the simulations, two dimensional photonic crystals were fabricated on amorphous and single crystal silicon-on-insulator substrates utilizing electron beam lithography and inductively coupled plasma etching. A unique etching process utilizing a combination of Cl_2 and C_4F_6 gases was developed and characterized which displayed a vertical profile with a sidewall angle of under 1 degree from vertical and very smooth sidewalls for features as small as 150 nm. The high quality of the etching was the key to obtaining extremely low loss, low noise structures, making feasible the fabrication of large area photonic crystal devices that are necessary to measure propagation phenomena. Reflectivity measurements were used to directly observe the photonic band structure with excellent correlation with theory. A device was designed and fabricated which successfully verified the prediction of the simulations through measurements of the self-

collimation effect across a broad range of infrared wavelengths. A solid foundation for the necessary components (simulation, modeling, design, fabrication, and measurement) of two-dimensional photonic crystal has been demonstrated. Elements from solid state physics, materials science, optics, and electromagnetics were incorporated to further the understanding of the mechanism of beam propagation in photonic crystals and illuminate the vast potential of research in periodic media.

CHAPTER 1

INTRODUCTION TO PHOTONIC CRYSTALS

Ever since the discovery of atoms and crystals, periodic structures have been an integral part of the understanding of material systems. Recently, research in engineered periodic structures in the same size range as the wavelength of interest has flourished. Electromagnetic waves have garnered the most intense attention beginning with the proposal by Yablonovitch[2] and John[3] on the inhibition of spontaneous emission and the confinement of photons by structures exhibiting a photonic band gap. In addition to electromagnetic crystals, acoustic signals[4] and even water waves[5] have been demonstrated to display band gap properties in structures with a periodic elastic modulus. Artificially engineered periodic structures allow control over every detail, even the unit cell. This intriguing field continues to develop new breakthroughs as creativity and innovation forge crystals with unique and novel properties.

This thesis delves into the properties of two-dimensional photonic crystals, one of the simplest classes of structures available within this topic. Even though it is such a simple structure, the methods of analyzing and interpreting the properties are still being developed. The methods of modeling and simulating the properties of periodic structures were introduced and developed for the behavior of electrons in atomic crystals, where the Schrödinger's Equation reigns supreme[6,7]:

$$\nabla^2\Psi + \frac{2m}{\hbar^2}\left(E - V(\vec{r})\right)\Psi = 0 \qquad \textbf{Equation 1}$$

where Ψ is the electron wave function, m the mass, ħ the Planck's constant divided by 2π, E the energy, and V(r) the electric potential as a function of position r. Maxwell's Equations serve as the counterpart in describing photons, or electromagnetic waves. The Maxwell's Equations can be rearranged to parallel the exact same format as the Schrödinger's Equations[8]:

$$\nabla^2 E + k_0{}^2 E = 0$$

$$\nabla^2 B + k_0{}^2 B = 0 \qquad \textbf{Equation 2}$$

$$\text{where} \quad k_0^2 = \varepsilon(\vec{r})\left(\frac{2\pi}{\lambda}\right)^2$$

where E is now the electric field, B the magnetic field, and k_0 the wave vector in free space, ε(r) the dielectric constant as a function of position r, and λ the wavelength of light. This parallelism led naturally to the band structure formalism to describe the properties of photonic crystals. The initial development of photonic crystals mirrored the phenomena already characterized for atomic crystals, such as the band gap and defect modes from doping[9-11]. Once the band gap effect was established, development in the field was driven towards the approaches taken by the microwave and radio frequency (RF) fields where photonic band gap materials were substituted for the perfect electrical conductor in frequency ranges, such as the visible and infrared (IR), where metallic conductors exhibited significant loss. Size issues challenged the community until fabrication techniques matured in the mid 1990's allowing fabrication of structures in the submicron range. This approach gave birth to line defect waveguides[12-19] and high Q-factor cavities[19-21] which burgeoned beyond the limitations of its longer frequency range

counterparts to demonstrate devices such as add/drop filters[22,23] for dense wavelength division multiplexing (DWDM) applications.

Recently, the study of bulk propagation effects, such as superprisms[24-29] (large refraction angles with small deviation in input angle), self-collimation[29-36] (reduction of the spreading of a beam as it propagates), and negative index of refraction[37-39], has attracted large attention. These phenomena display parallels to the electronic band structure, but take advantage of the unique properties of photons. The electronic band structure is governed by the solution of the periodic form of Schrödinger's Equation[7], coupled with the knowledge of the properties of electrons, such as Pauli Exclusion Principle and Hund's Rule. When characterizing the electronic properties of a crystal, the emphasis is on the density of states and the Fermi-Dirac distribution. By filling the band structure from the lowest energy and considering the behavior of the highest energy electrons, the properties of insulators, conductors, and semiconductors can be obtained[6,7,40]. In addition, due to the tractability of the electron by electric and magnetic fields and the polycrystalline nature of most materials, the direction, or wave vector, of the electrons in a crystal is often overlooked. On an atomic level, the electron will travel only in the propagation direction allowed by the crystal, but by changing its direction, it will macroscopically follow the direction imposed by the potential difference set by a voltage gradient. Photons are fundamentally different from electrons in that they do not follow the Pauli Exclusion Principle. As bosons, photons obey the Bose-Einstein distribution which allows an infinite number of photons to occupy the same state[6,40]. The density of states is no longer a focus in the analysis. Instead, the wave vector and the directionality of the band structure become the primary focus of the interpretation. The

wave vector of a photon is difficult to modify without material boundaries, thus discrete propagation directions and phenomena which take advantage of controlling the wave vector of a photon, such as refraction, become possible. Photonic crystals utilize the periodic arrangement of dielectric materials to control the wave vector of photons. The self-collimation effect investigated in this thesis is a phenomenon which utilizes this distinct property of a photon to control the propagation of a beam of light inside the photonic crystal.

Various methods exist for the fabrication of periodic structures. For large structures, with feature sizes on the order of cm or greater, bulk machining techniques are adequate. The first demonstration of a photonic band gap was in the Yablonovite[41-43] structure, a 3-cylinder diamond cubic-like lattice structure, in the microwave wavelength, which allowed construction utilizing mechanical drilling of a dielectric slab. This structure, schematically shown in Figure 1, was fabricated and successfully demonstrated a photonic band gap for the 10~13GHz wavelengths[42]. Even though the photonic band

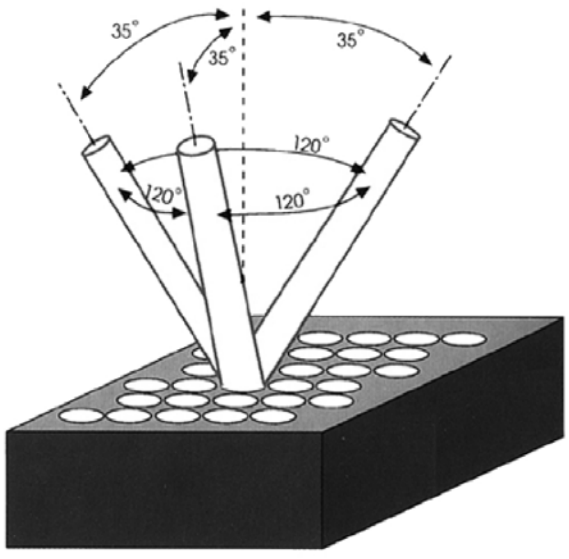

Figure 1. Schematics of the drilling directions to form Yablonovite[41-43].

gap was demonstrated at microwave wavelengths, interest in band gap structures failed to develop due to the availability of metals to act as perfect reflectors. However, the race to fabricate photonic crystal structures that display a complete band gap in the visible and near infrared wavelengths was started and arguably still continues today[44-49]. Three classes of fabrication methods emerged for creating photonic crystals. Lithographic techniques developed in the microelectronic industry provide an ideal method for the fabrication of two-dimensional photonic crystals. Three-dimensional log-pile structures have been fabricated utilizing lithography by stacking alternate layers through wafer bonding[49,50] and through sequential layer growth and planarization using chemical mechanical polishing[47,48]. An example of a two-dimensional line defect waveguide[51] and a log-pile structure[48] are shown in Figure 2. Self-assembly of monodispersed colloidal particles proved to be a breakthrough in providing an affordable method for fabricating the opal and inverse opal structures which, with an appropriate index of refraction, exhibit complete photonic band gaps. Holography techniques utilizing the interference of multiple beams to create periodic structures give the ability to fabricate defect free

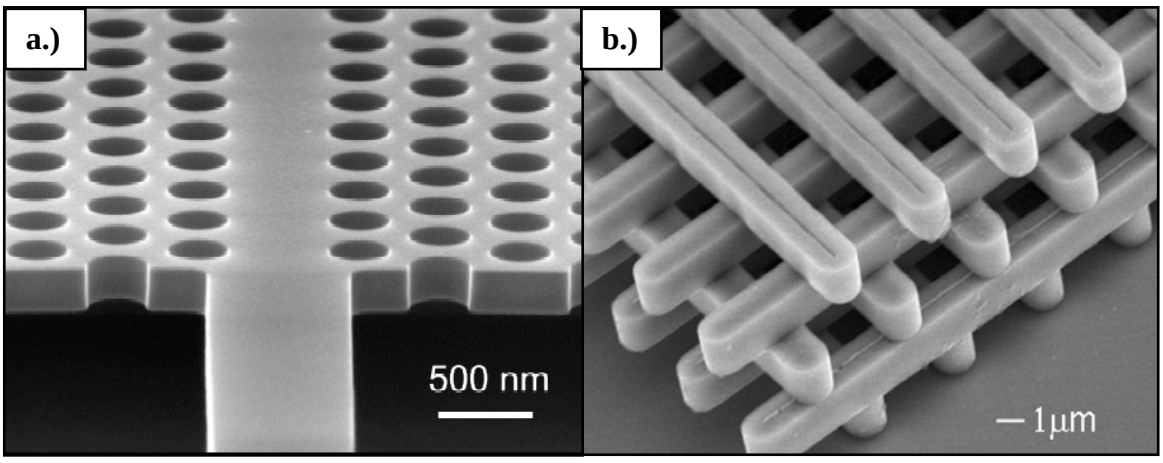

Figure 2. a.) 2D[51] and b.) 3D[48] photonic crystals fabricated using lithography and microelectronics technology

large area photonic crystals with any degree of periodicity by combining different numbers of beams. In this thesis, fabrication of two-dimensional photonic crystals utilizing electron beam lithography coupled with thin film deposition and plasma etching was investigated.

With the successful demonstration of the photonic band gap, focus turned to the engineering of devices utilizing the photonic band structure. Numerous theoretical studies were conducted on two-dimensional structures as the computational capability could accommodate the size of the simulation. Functionalities in band gap guided line defect waveguides produced many of the initial simulated functionalities[12-15], as shown in Figure 3. The silicon-on-insulator (SoI) structure consisting of a high index (n = 3.45)

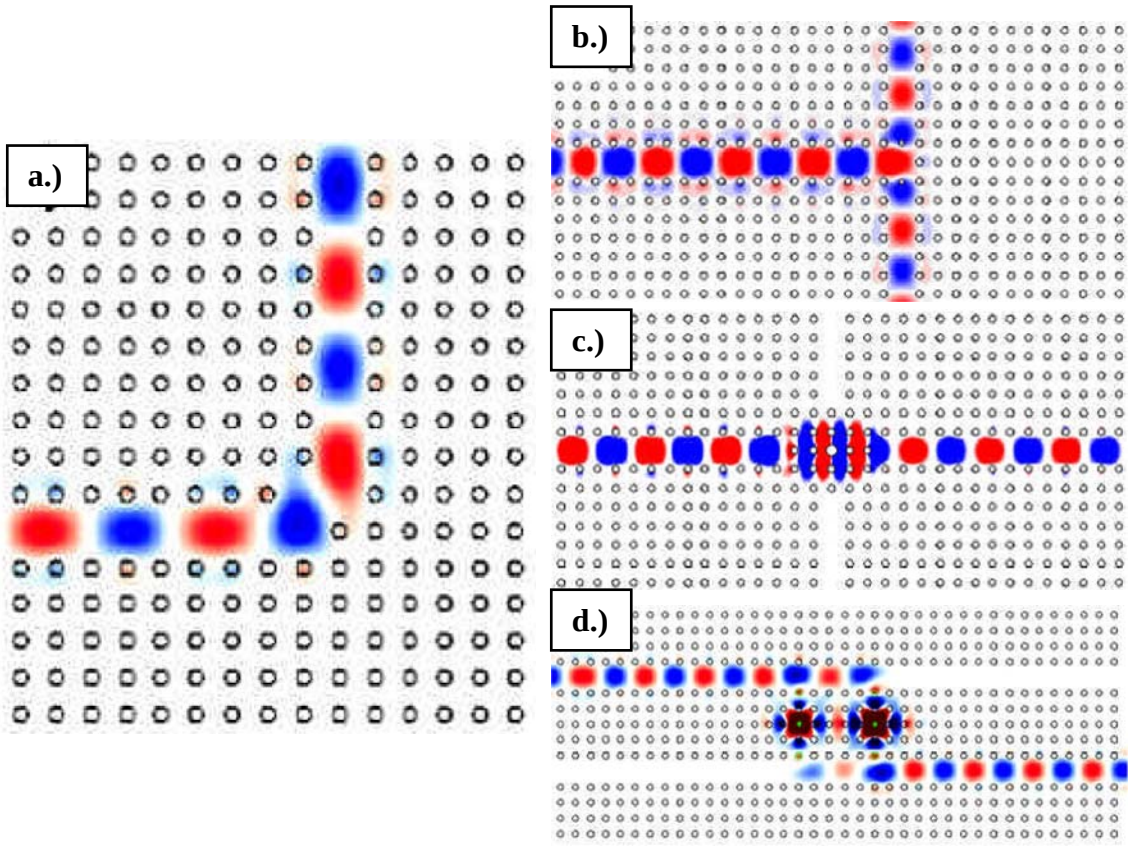

Figure 3. Simulation of line defect waveguides showing a.) sharp bend[12], b.) beam splitting[15], c.) leakage free intersections[14], and d.) coupling between branches[13]

silicon layer on top of silicon oxide layer (n = 1.45) provided the index confinement in the off-plane direction allowing for a structure closely resembling an ideal two-dimensional structure. Photonic crystals fabricated on SoI have successfully demonstrated the theoretical calculations of defect waveguides[51] with sharp bends and resonant cavity devices. A schematic of a drop filter composed of a line defect waveguide and resonant cavities, along with an SEM image and the measured frequency response are shown in Figure 4[23].

Negative index phenomena, such as imaging, focusing, and negative refraction have also been simulated[37-39] and experimentally observed[27], as shown in Figure 5 and Figure 6. The concept of bulk propagation through the photonic crystal having self-collimation and lens-like effects was first proposed by Kosaka[30] qualitatively utilizing the curvature of the equifrequency contour. Figure 7 reveals further simulation results and theoretical developments for the propagation of self-collimated beams demonstrating the ability to make sharp turns and split beams as was demonstrated for the line defect waveguide[33,34]. These effects were demonstrated by Prather[34,35], as seen in Figure 8,

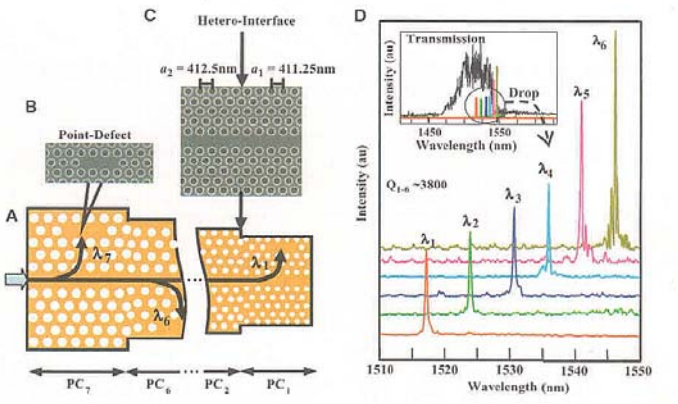

Figure 4. a.) Schematic of a drop filter composed of photonic crystals with slightly varying sizes utilized to filter out selected wavelength channels from the line defect waveguide b.) SEM picture of the cavity c.) SEM picture of waveguide region d.) Drop channel intensity[23]

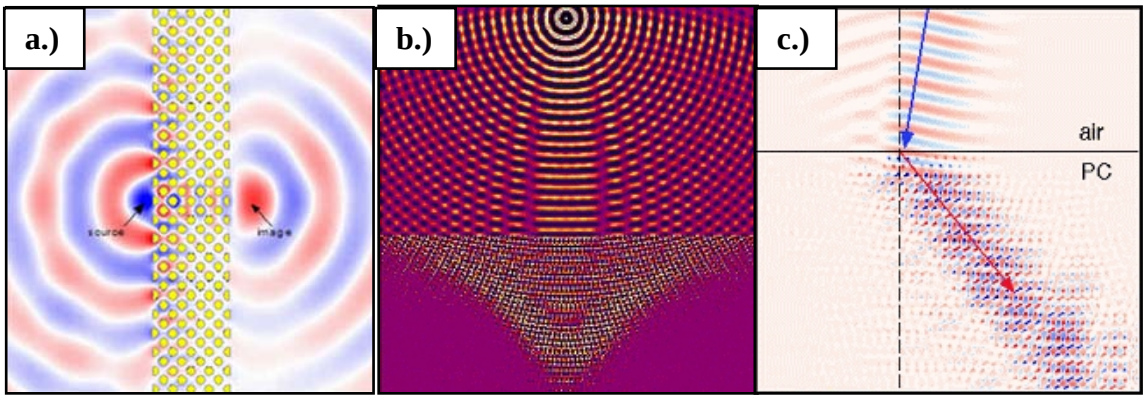

Figure 5. Simulations of negative index phenomena such as focusing and imaging in a.)[39] and b.) and negative refraction in c.)[38]

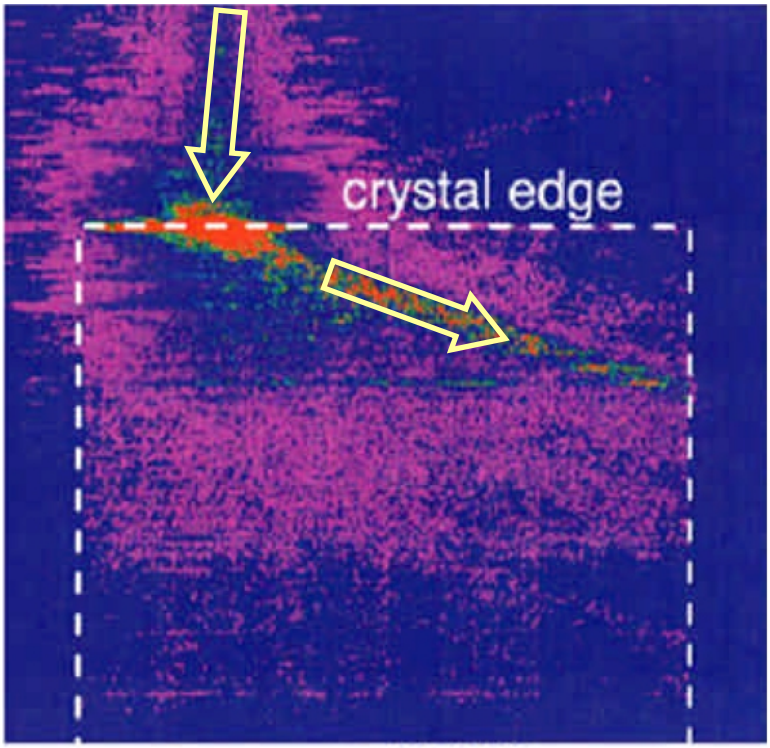

Figure 6. Experimental observation of negative refraction[27]

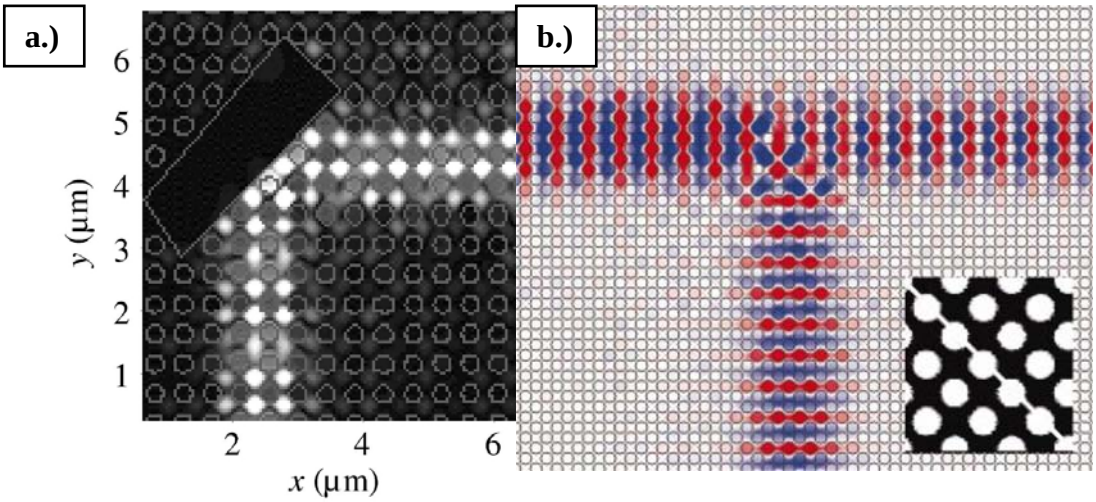

Figure 7. Simulation results showing a.) beam bending[34] and b.) beam splitting with self-collimated beams[33]

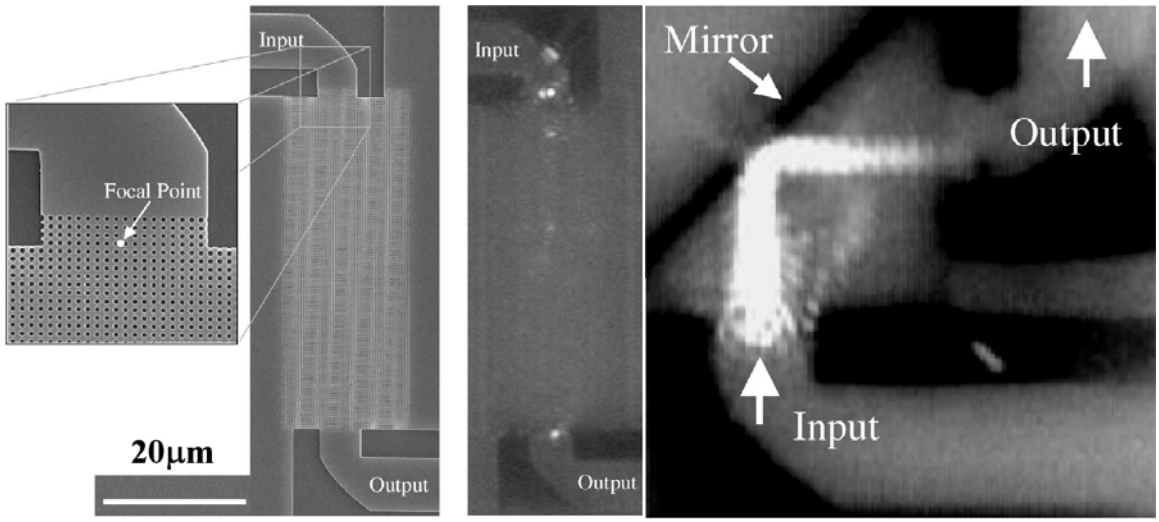

Figure 8. Experimental demonstration of self-collimated beams[34]

utilizing structures fabricated on a SoI with electron beam lithography. Two-dimensional photonic crystal devices have proven to be a fruitful area of research fulfilling the promises and expectations of the modeling and simulation results.

This study focuses on further understanding light propagation through a two dimensional photonic crystal. The thesis is divided into three main chapters focusing on modeling and simulation, fabrication, and property measurement of two-dimensional photonic crystals. Chapter 2 details the simulation methodology utilized for calculating the photonic band structure and modeling the devices. An effective index model for the propagation of Gaussian beams in a photonic crystal was developed, followed by simulations of applications utilizing self-collimated beams. Chapter 3 provides an extensive overview of the fabrication process with an emphasis on the development of a unique plasma etch that produced highly anisotropic and very smooth sidewalls necessary for photonic crystal devices. An overview of the measurement techniques and the results for the fabricated devices are given in Chapter 4. Each chapter ends with a discussion to highlight the key points presented. Finally, Chapter 5 concludes the thesis with an overview of the accomplishments, their significance, and outlook for the work presented.

CHAPTER 2

MODELING AND SIMULATION OF PHOTONIC CRYSTAL PROPERTIES

Introduction

Simulation has been a cornerstone of the photonic crystal community ever since its inception when the existence of the photonic band gap was postulated through the results of theoretical simulations[2,3]. Indeed, the photonic crystal community has reversed the centuries old method of modeling and simulation being created to explain an observed phenomenon. Photonic crystal research has benefited from the advances in the microelectronic industry, not just in fabrication techniques, but in the computing power that it has provided to make accurate simulations. Photonic crystal research is an area which exemplifies the revolution in the scientific community, where the models and the simulation methods have reached an accuracy which gives confidence that the phenomena observed in the simulation can be experimentally verified. This chapter introduces two methods for analyzing the properties of photonic crystals, the band diagram and the allowed wave vector surface. After introducing these methods, detailed overviews of the plane wave expansion and finite difference time domain methods, the two most common simulation methods for the analysis of photonic crystal, are given. The majority of the simulations performed for this thesis was developed and ran in the Matlab environment and a section is devoted within the description of each method to address issues encountered in the code development. The next section describes the development of an effective index of refraction model to describe propagation of a

Gaussian beam through a photonic crystal. A survey to determine the self-collimation frequencies in a square lattice photonic crystal was conducted followed by an analysis of the robustness of the self-collimation phenomenon to manufacturing errors. Finally, simulation results for several applications of self-collimated beams in photonic crystals are presented.

Analysis Methods

Simulations of photonic crystal properties begin with the calculation of the band structure. The band structure is calculated by utilizing the Bloch boundary condition, which is the periodic boundary condition with a specified wave vector to add a phase change at the boundary. Simulations can calculate or identify the frequencies of the mode which is stable with the imposed Bloch condition. By calculating these modes for the wave vectors in the first Brillouin zone, the band structure of the photonic crystal can be found. The band structure for the wave vectors outside of the first Brillouin zone are then found by folding the band diagram along the directions of periodicity[6,52]. The wave vector space, analogous to reciprocal lattice space, is a mapping of the direction and period of a wave into a point. The vector defined by the origin and a point in the wave vector space corresponds to a wave which has the wave fronts propagating along the wave vector direction and the period proportional to the inverse of the vector length. When compared to the reciprocal lattice, the crystal plane mapped in reciprocal lattice corresponds to the equiphase plane of a plane wave depicted by the same wave vector.

Several graphical representations similar to solid state physics have become common in displaying the band properties of the photonic crystals. The band structure for the transverse magnetic (TM) slab mode of a square lattice photonic crystal made of

dielectric (n = 3.3) pillars with a radius of 20% of the lattice constant, shown in Figure 9, will be used as an example for this section. It is worth noting that the TM-slab mode corresponds to the TE photonic crystal mode as the slab mode calculation is based on the cross section while the top-down view is the reference plane for the photonic crystal calculation. For this thesis, the slab mode conventions are utilized when referring to the modes. The allowed wave vector surface, depicted in Figure 10, displays a three dimensional plot of the solutions solved for each wave vector. Only the points in the

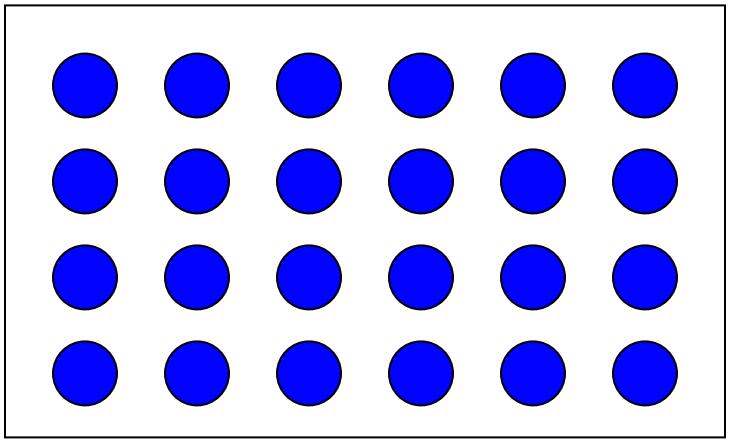

Figure 9. Schematic of a square lattice photonic crystal made of high dielectric constant pillars

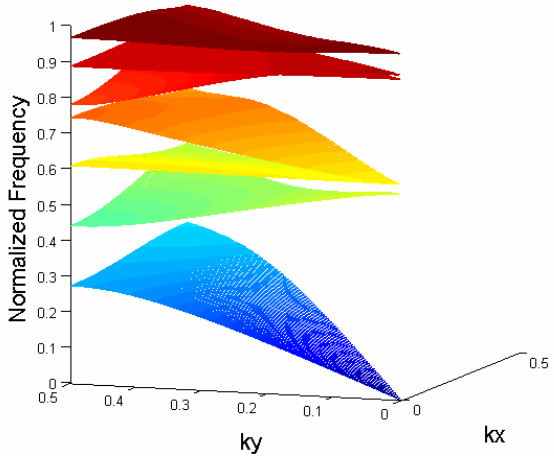

Figure 10. The allowed wave vector surface for the TM mode of a square lattice photonic crystal

irreducible Brillouin zone, the triangle which can be repeated to reproduce the entire band diagram, are plotted. Even though this representation is compact and shows a complete representation of the band structure, it is visually too complex and no valuable information can be garnered from it. A representation including only one band can be utilized to show the curvature of the surface but will not be used in this thesis[34].

The band diagram is the most common representation of the band structure of photonic crystals. This representation plots the boundary of the irreducible Brillouin zone, the smallest area of the wave vector space that, through symmetry operations, can form the whole wave vector space. Figure 11 shows an example of the band diagram. The x-axis is divided into regions representing the line segments connecting the Γ–X–M–Γ points in wave vector space. The band diagram allows identification of the location and width of the band gap and the movement of bands with respect to changing conditions. The band diagram is often expressed in normalized frequency and wave

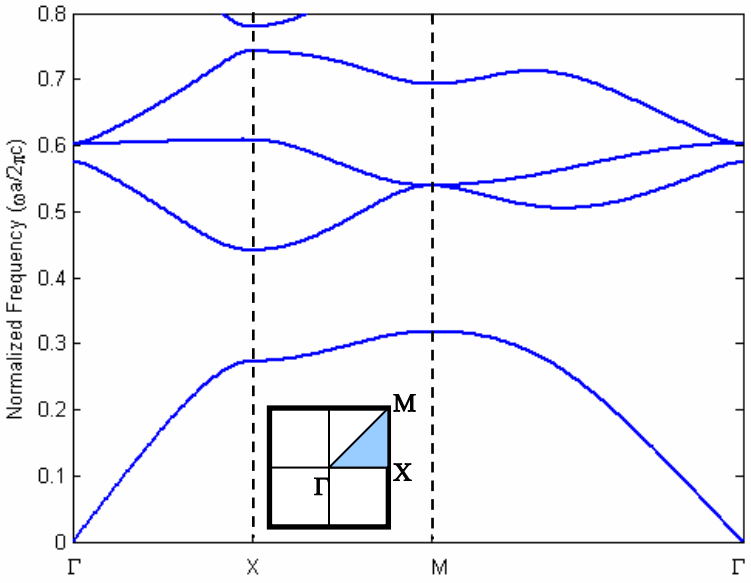

Figure 11. The band diagram for the TM mode of a square lattice photonic crystal

vector due to the scalability of Maxwell's Equations given that the structure is not small enough to require consideration of quantum effects. In the normalized frequency notation, the frequency is scaled so that a plane wave in free space at a normalized frequency of 1 has a period equal to the lattice constant. This corresponds to:

$$\omega_n = \frac{\omega a}{2\pi c} \qquad \textbf{Equation 3}$$

where ω_n is the normalized frequency, ω is the angular frequency, a is the lattice constant, and c is the speed of light.

The representation of the band structure most useful for propagation through a photonic crystal is the allowed wave vector contour, also called the equifrequency contour. This representation is obtained by taking one band in the band surface and taking slices with equal frequencies. Each curve represents the allowed wave vector surface for that frequency and can be utilized in the same manner as in refractive optics to obtain the propagation direction and coupling at an interface. The allowed wave vector contours along with a schematic describing the methodology of utilizing these contours for determining the refraction angle is given in Figure 12. The allowed wave vector for an isotropic material is a circle, as seen on the left side of the interface. To graphically determine the refraction angle, the wave vector of the incoming wave is graphed from the periphery of the circle to the origin. The transverse component of the wave vector is conserved, and a line is drawn perpendicular to the interface that intersects the allowed wave vector curve of the second material. The wave will couple into the second material with a wave vector equal to the vector from the origin to the intersection point[53]. This principle applies even for the allowed wave vector curve of a photonic crystal, which can

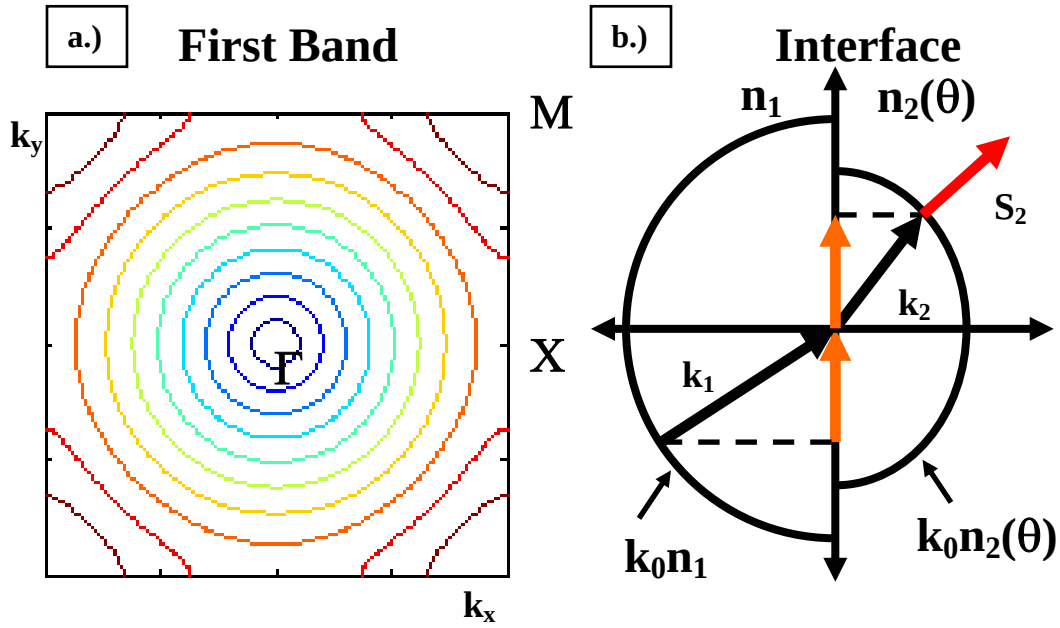

Figure 12. a.) Allowed wave vector contours for the first band of a square lattice photonic crystal b.) Methodology for using the allowed vector contour to calculate the refraction angle at an interface

take on shapes that are not circular or elliptical as in isotropic materials. The allowed wave vector surface of the first band reveals some noteworthy properties of the photonic crystal. Near the center of the first band, the frequency is the lowest, corresponding to waves with a lattice constant which is much larger than the periodicity of the lattice. In this regime, the wave sees an average dielectric constant and the allowed wave vector is circular as in an isotropic material. As the wave vector reaches a value which is near the edge of the Brillouin zone, the shape gradually changes from a circle to a shape resembling the lattice, or a square. Near the top of the first band, near the M point, the allowed wave vector once again shifts towards a circle, but now with the center located on the M point rather than on the Γ point. This trend where the allowed wave vector curve near a symmetrical point in the wave vector space approximates a circle is the source of the negative index and the self-collimation effects.

Simulation Techniques

Since the exact solution to Maxwell's Equation for photonic crystals cannot be obtained, a numerical method must be employed to find approximate solutions describing the system. Due to the rapidly improving performance of personal computers and workstations, these numerical calculations can be performed in a reasonable time frame for research purposes. All programs in this proposal use the Matlab programming language running on high end personal computers with CPU powers ranging from 2.8GHz to 3.4GHz Pentium IV processors and 3GB of memory.

Two different approaches to simulate photonic crystals have been pursued in this thesis. The first method, the plane wave expansion (PWE) method, is a straight forward numerical approximation of the solutions to the wave equation using Fourier expansion of the dielectric constant and the electric/magnetic field as a function of position. The second method utilized is Finite difference time domain (FDTD) simulation. In this method, an electromagnetic (EM) wave traveling through a grid representing the photonic crystal is monitored to discern the interaction of the EM wave with the photonic crystal. The FDTD simulation is a very flexible technique allowing for the simulation of infinitely periodic structures as well as discrete devices containing defects and waveguide structures.

Plane Wave Expansion Method

The PWE method is a numerical method for solving the decoupled Maxwell's Equations. For this method, the form of the decoupled equations are[54]:

$$\frac{1}{\varepsilon(\vec{r})}\nabla\times\left\{\nabla\times\vec{E}(\vec{r})\right\}=\frac{\omega^2}{c^2}\vec{E}(\vec{r})$$

$$\nabla \times \left\{ \frac{1}{\varepsilon(\vec{r})} \nabla \times \vec{H}(\vec{r}) \right\} = \frac{\omega^2}{c^2} \vec{H}(\vec{r}) \qquad \textbf{Equation 4}$$

where E is the electric field and H the magnetic field. Then the dielectric function is approximated by a two-dimensional Fourier series expansion of the form[54]:

$$\frac{1}{\varepsilon(\vec{r})} = \sum_{\vec{G}} \kappa(\vec{G}) \exp(i\vec{G} \cdot \vec{r}) \qquad \textbf{Equation 5}$$

where κ(G) are the two-dimensional Fourier coefficients of the dielectric function in space. Furthermore, through the Bloch's Theorem, the solution to the differential equation can also be expressed as a Fourier series expansion[54]:

$$\vec{E}_{\vec{k}n}(\vec{r}) = \sum_{\vec{G}} \vec{E}_{\vec{k}n}(\vec{G}) \exp\left\{ i(\vec{k} + \vec{G}) \cdot \vec{r} \right\}$$

$$\vec{H}_{\vec{k}n}(\vec{r}) = \sum_{\vec{G}} \vec{H}_{\vec{k}n}(\vec{G}) \exp\left\{ i(\vec{k} + \vec{G}) \cdot \vec{r} \right\} \qquad \textbf{Equation 6}$$

where k is now the wave vector. When these equations are substituted back into Maxwell's Equations, a set of linear equations are formed, which can be solved using linear algebra techniques[54]:

$$-\sum_{\vec{G}'} \sum_{\vec{G}} \kappa(\vec{G} - \vec{G}')(\vec{k} + \vec{G}') \times \left\{ (\vec{k} + \vec{G}') \times \vec{E}_{\vec{k}n}(\vec{G}') \right\} = \sum_{\vec{G}} \frac{\omega_{\vec{k}n}^2}{c^2} \vec{E}_{\vec{k}n}(\vec{G})$$

$$-\sum_{\vec{G}'} \sum_{\vec{G}} \kappa(\vec{G} - \vec{G}')(\vec{k} + \vec{G}) \times \left\{ (\vec{k} + \vec{G}') \times \vec{H}_{\vec{k}n}(\vec{G}') \right\} = \sum_{\vec{G}} \frac{\omega_{\vec{k}n}^2}{c^2} \vec{H}_{\vec{k}n}(\vec{G}) \qquad \textbf{Equation 7}$$

The equations on the left hand side can be written as square matrices if G and G' are of the same size while the right hand side is a constant times a vector of E or H. Furthermore, the same vector of E_{kn} as on the right side can also be factored out of the left hand square matrix to form the common eigenvalue problem of the form:

$$Ax = \lambda x \qquad \textbf{Equation 8}$$

where A is the square matrices formed by κ, k, G, and G'; λ is ω_{kn}^2/c^2; and x is a vector of E_{kn} or H_{kn}. Therefore, the solutions λ and x can be numerically solved using linear algebra functions available in commercial software (such as the eig/eigs function in Matlab).

In the PWE method, input values corresponding to the physical geometry of the photonic crystals, number of expansions to take in the Fourier expansion, and the k vector to be evaluated results in the eigenvalue solution λ and the eigenvector solution x. For each calculation, there are numerous nontrivial solutions λ with their corresponding eigenvectors with each nontrivial solution corresponding to a different band in the band diagram. The band diagram is the plot of the ω (calculated from λ) against the input k vector. The accuracy of the PWE method is determined through the number of Fourier expansions of the dielectric function and the electric/magnetic field. Most simulations are conducted with between 1000 and 8000 plane waves in the expansion[55,56]. Due to computational limitations, a larger expansion is impractical. This limit puts a severe restriction on the accuracy of this method since the number of plane waves is given by the formula:

$$\begin{aligned} \#\_of\_plane\_waves\_3D &= (2n-1)^3 \\ \#\_of\_plane\_waves\_2D &= (2n-1)^2 \end{aligned} \qquad \textbf{Equation 9}$$

Where n is the number of independent Fourier coefficients along each principal axis (κ(G) = κ^*(-G) so they are not independent). It is clearly seen that for a three-dimensional case, the dielectric function and the solution can only be expanded in at most 10 Fourier coefficients per side. For the two-dimensional case, a more reasonable expansion in 30-

45 Fourier coefficients can be performed. Care must be taken in calculating the Fourier coefficients. To decrease the Fourier coefficients to the requisite number, the value of the dielectric constant can be averaged over the fine grid to fit it to a coarse grid. This method is required for simulations which directly utilizes the dielectric function in the calculations. However, for the PWE method, only the Fourier coefficients are used. A more accurate depiction of the structure can be obtained by first taking the fast Fourier transform of a very fine grid, and then decreasing the number of Fourier coefficients by utilizing the values symmetrically around the origin. The difference can be seen in Figure 13. Utilizing the fine grid decreases the sharp corners which occur when the dielectric function is averaged first. Utilizing sufficient conditions, the PWE method can be used to calculate the band structure of the photonic crystal quickly and accurately. All of the band structures in this thesis are calculated using the PWE method unless otherwise stated.

The Matlab implementation of the PWE method is very straight forward, as the environment was created to handle matrix operations. The m-file functions written to

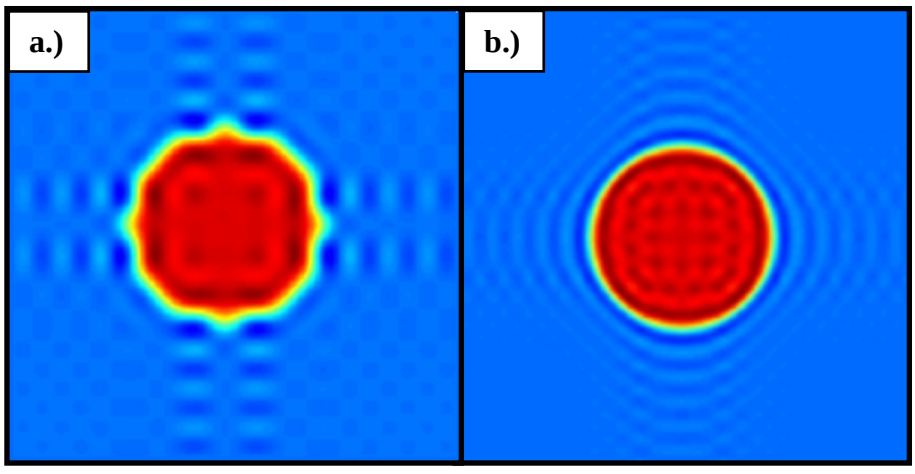

Figure 13. Dielectric function calculated for 529 Fourier coefficients (23x23) with two different methods. a.) Averaging the dielectric function to a coarse grid b.) Utilizing the center section of the Fourier transform of a fine grid

calculate the band diagram for the TM mode of a two-dimensional photonic crystal is given in APPENDIX A. The program was divided into two functions to make the code simple and efficient to use. The initTM2.m function takes the inputs of a matrix containing the inverse of the dielectric constant, the G vectors of the unit cell (x and y directions for square lattice), and the number of Fourier coefficients to expand along each direction. The initTM2.m function initializes all of the variables necessary so that only the wave vector and the number of bands to solve for needs to be input for the solveTM2.m function. This format makes programming to solve for different dielectric structures and different configurations of the band structure, such as the band diagram and the allowed wave vector contours, straight forward by defining the appropriate loops in a script. The Matlab function for solving the eigenvalues of a matrix (eigs), is a precompiled code written in Fortran, thus the speed of the code was comparable to codes written in C or Fortran. Code written in Fortran was still faster, but the added flexibility and the ease of integrating high level graphical and signal processing functions within the program made the developed code much more powerful in application. The corresponding TE mode program requires only slight modifications and is not included in the Appendices.

Finite Difference Time Domain Simulation

The PWE method is useful for perfectly periodic materials where a small number of Fourier coefficients may be used to accurately depict both the dielectric modulation and the solution. However, many geometries of interest are not perfectly periodic and are too complex to accurately depict using a small number of Fourier coefficients. For these cases, the finite difference time domain (FDTD) simulation method can be used. FDTD

has the advantage of using a grid to define the material properties so sharp discontinuities can be accurately modeled compared to using a Fourier series. However, due to the use of square or cubic grids, smooth curves need to be approximated using blocks causing a "staircase" effect[57]. The evolution of an EM wave is followed through discretized time steps in this finite grid.

The FDTD method can be derived from the Maxwell's Equations by discretizing the curl equations in the form (for simplicity, the assumptions of linear, isotropic, nondispersive, no-loss material is made)[57]:

$$\frac{\partial \vec{H}}{\partial t} = -\frac{1}{\mu}\nabla \times \vec{E}$$

$$\frac{\partial \vec{E}}{\partial t} = \frac{1}{\varepsilon}\nabla \times \vec{H} \qquad \textbf{Equation 10}$$

Expanding the curl operators yields six coupled scalar equations[57]:

$$\frac{\partial H_x}{\partial t} = \frac{1}{\mu}\left[\frac{\partial E_y}{\partial z} - \frac{\partial E_z}{\partial y}\right]$$

$$\frac{\partial H_y}{\partial t} = \frac{1}{\mu}\left[\frac{\partial E_z}{\partial x} - \frac{\partial E_x}{\partial z}\right]$$

$$\frac{\partial H_z}{\partial t} = \frac{1}{\mu}\left[\frac{\partial E_x}{\partial y} - \frac{\partial E_y}{\partial x}\right]$$

$$\frac{\partial E_x}{\partial t} = \frac{1}{\varepsilon}\left[\frac{\partial H_z}{\partial y} - \frac{\partial H_y}{\partial z}\right]$$

$$\frac{\partial E_y}{\partial t} = \frac{1}{\varepsilon}\left[\frac{\partial H_x}{\partial z} - \frac{\partial H_z}{\partial x}\right]$$

$$\frac{\partial E_z}{\partial t} = \frac{1}{\varepsilon}\left[\frac{\partial H_y}{\partial x} - \frac{\partial H_x}{\partial y}\right] \qquad \textbf{Equation 11}$$

These equations are discretized to form the update equations to step through each time step and are the basis of the FDTD method for EM radiation. For the case where one dimension extends to infinity with no variation, these equations can be simplified since all of the partial derivatives with respect to z vanish[57]:

$$\frac{\partial H_x}{\partial t} = \frac{1}{\mu}\left[-\frac{\partial E_z}{\partial y}\right]$$

$$\frac{\partial H_y}{\partial t} = \frac{1}{\mu}\left[\frac{\partial E_z}{\partial x}\right]$$

$$\frac{\partial E_z}{\partial t} = \frac{1}{\varepsilon}\left[\frac{\partial H_y}{\partial x} - \frac{\partial H_x}{\partial y}\right]$$

$$\frac{\partial E_x}{\partial t} = \frac{1}{\varepsilon}\left[\frac{\partial H_z}{\partial y}\right]$$

$$\frac{\partial E_y}{\partial t} = \frac{1}{\varepsilon}\left[-\frac{\partial H_z}{\partial x}\right]$$

$$\frac{\partial H_z}{\partial t} = \frac{1}{\mu}\left[\frac{\partial E_x}{\partial y} - \frac{\partial E_y}{\partial x}\right] \qquad \textbf{Equation 12}$$

Notice that the first three equations depend on only H_x, H_y, and E_z while the last three are also dependent only on each other. These two cases are the TE and the TM modes respectively. Therefore, when simulating a two-dimensional structure, a smaller simulation using only half of the variables can be conducted for the TE and TM cases separately. A leapfrog scheme where the E and H components are displaced half a cell width apart and also half a time step apart is used to maximize the efficiency of the algorithm[57].

The FDTD method can be used for many different types of simulations. It can simulate both the PBG structure and the dispersion characteristics in an infinite, as well as a finite, structure. In addition, the FDTD method has been used to simulate complex cases such as propagation along an off-axis direction in a two-dimensional structure[58].

Band Diagram Calculation

The FDTD technique can be used to calculate the band diagram for perfectly periodic structures in two- and three-dimensions as well as structures with periodicity in two dimensions and anisotropy in the third dimension, such as waveguides. To understand how to simulate the band structure using the FDTD method, the physical significance of each point in the band diagram needs to be examined. As described in the characterization section, each point on the band diagram represents an EM field pattern, which corresponds to a stationary field comparable to a standing wave pattern in a vibrating string. Therefore, to simulate the band diagram, a long simulation of the periodic structure is performed to isolate the stationary signal from the background noise. All field intensities deviating from the stationary field pattern will travel through the grid and vanish when the time average is taken over a sufficiently long simulation. When taking the boundary conditions, recall that the solution to the Maxwell's Equations can be expanded in a Fourier series as in the PWE case:

$$\vec{E}_{\vec{k}n}(\vec{r}) = \sum_{\vec{G}} \vec{E}_{\vec{k}n}(\vec{G}) \exp\left\{i(\vec{k}+\vec{G})\cdot\vec{r}\right\}$$

$$\vec{H}_{\vec{k}n}(\vec{r}) = \sum_{\vec{G}} \vec{H}_{\vec{k}n}(\vec{G}) \exp\left\{i(\vec{k}+\vec{G})\cdot\vec{r}\right\} \qquad \textbf{Equation 13}$$

Substituting r+L for r in these expressions where L is the principle lattice vector for the unit cell and solving in terms of $E_{kn}(r)$ and $H_{kn}(r)$[56]:

$$\vec{E}_{\vec{k}n}(\vec{r}+\vec{L}) = \sum_{\vec{G}} \vec{E}_{\vec{k}n}(\vec{G}) \exp\left\{i(\vec{k}+\vec{G})\cdot(\vec{r}+\vec{L})\right\} = \vec{E}_{\vec{k}n}(\vec{r}) \exp\left\{i\vec{k}\cdot\vec{L}\right\}$$

$$\vec{H}_{\vec{k}n}(\vec{r}+\vec{L}) = \sum_{\vec{G}} \vec{H}_{\vec{k}n}(\vec{G}) \exp\left\{i(\vec{k}+\vec{G})\cdot(\vec{r}+\vec{L})\right\} = \vec{H}_{\vec{k}n}(\vec{r}) \exp\left\{i\vec{k}\cdot\vec{L}\right\}$$

$$\text{where} \quad \exp(i\vec{G}\cdot\vec{L}) = 1 \qquad \textbf{Equation 14}$$

Therefore, the boundary conditions are the periodic boundary condition with an appropriate phase shift applied proportional to the k vector. Many initial field patterns were tested including the delta function, random number generator, and a superposition of plane waves as described in the paper by Chan et. al. [56]. For simulations of the primitive unit cell, all initial conditions worked well. However, for non-primitive unit cells, the superposition of plane waves was necessary to meet the boundary conditions. The Fourier transform of the resulting data was analyzed for peaks corresponding to each data point on the band diagram. Sample band diagram calculated using a 50x50 grid for the same dielectric profile used in the PWE section was shown in Figure 14. The results show that long time steps are necessary to accurately simulate the band diagram.

Even though perfectly periodic materials shed light on the possibilities of photonic crystals, real applications often fall far short of the perfectly periodic conditions used for the simulation. One main deviation is the waveguide structure where the third dimension is confined through total internal reflection rather than extending to infinity, as the two-dimensional case assumes. In a waveguide structure, the electromagnetic energy

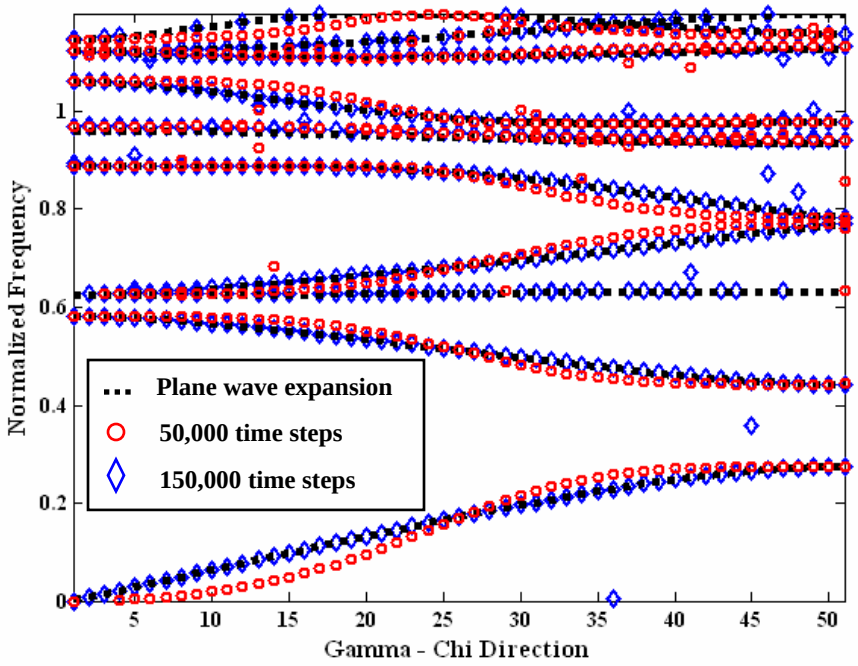

Figure 14. Band diagram calculated using the FDTD method (dots) compared with those using the PWE method for the Γ–X direction

travels in both the waveguide and in the surrounding cladding area due to the evanescent field extending from the boundary of the waveguide[53]. Also, this confinement in the third direction can cause different modes to form in the third dimension complicating the analysis. The FDTD method can simulate the waveguide structure for comparison with the two-dimensional case simulated using the PWE method or the FDTD method. Results have shown that by utilizing the effective index calculated for the slab mode of an index confined waveguide layer, an accurate simulation of the band structure can be obtained by two-dimensional calculations for the three-dimensional slab structure[59].

Device Simulation

In addition to producing the band structure, the FDTD technique can simulate the behavior of finite structures and interfaces between photonic crystals and other materials.

In this type of simulation, an EM wave travels from air or another outside medium into the photonic crystal. The electric and magnetic fields can be recorded to monitor the evolution of the fields with any arbitrary structure. In this manner, a theoretical experiment can be performed to predict the behavior of actual photonic crystal devices.

Simulation of a device utilizing FDTD has the same basic steps as an actual experiment. First, a sample is created by defining the dielectric function for the simulation space. Then a light source is simulated as either a monochromatic sine wave or a Gaussian or modulated Gaussian at the inputs of the device. The response of the device is measured by recording the EM fields at the output location. The advantages of the FDTD method over an actual experiment are not only in the ease of creating and measuring a device, but in the degree of control it has on the data to be collected. By utilizing a Gaussian or a modulated Gaussian source in time, a range of frequencies can be measured in a single simulation. Also, field values can be measured in locations which can not be probed in an actual experiment along with the measurement not interfering with the propagating waves. The main limitation of this method is the computational size. Due to the shear size of the data which needs to be stored for such a simulation, computational space sizes are limited to around 50 million points. This is less than 400 grid points along each axis for a three-dimensional simulation, which limits the ability of 3-D FDTD to simulate realistic devices. However, for two-dimensional problems, 7000 grid points along each axis is possible allowing for the simulation of structures closely resembling an actual device. The finite simulation size requires a boundary condition which absorbs all of the radiation reaching the edge of the simulation space. This is accomplished through the Berenger's perfectly matched layer (PML). The

principle behind the PML lies in placing a lossy material at the edge of the simulation space with no reflections back into the grid. By satisfying the following conditions, a reflectionless interface for normal incidence can be achieved[57]:

$$\varepsilon_1 = \varepsilon_2$$

$$\mu_1 = \mu_2$$

$$\sigma^* = \sigma \mu_1 / \varepsilon_1 \qquad \textbf{Equation 15}$$

where ε and μ are the dielectric constant and magnetic permeability of the two materials, and σ^* and σ are the magnetic and electric conductivity of the PML material. To increase the performance of the PML for non-normal incidence, the two conductivities are gradually increased following a third or fourth order polynomial to slowly absorb the impinging radiation[57].

Numerous types of simulations can be performed utilizing the two-dimensional FDTD method. Transmission and reflection measurements and refraction angle measurements are commonly simulated. Self-collimation and negative index can also be demonstrated utilizing this method. All of the simulation figures shown in the introduction chapter were calculated utilizing the two-dimensional FDTD technique. In this thesis, measurement of the properties of the self-collimated beams as it propagates inside of a photonic crystal and simulations of the applications for self-collimated beams are conducted using this method.

Matlab Implementation

FDTD program is composed of a large number of additions, subtractions, multiplications, and divisions as a series of these operations must be performed at each

grid point. This brute force approach to calculation is not well suited for a high level programming environment such as Matlab, and resulted in a simulation speed which was 3 orders of magnitude slower for the Matlab code compared to a code written in C or Fortran. This difference arises from the high level variable type and variable consistency tests that Matlab performs at each iteration. To overcome this issue, the bulk of the calculations involving the floating point operations, were written in the C programming language and linked to Matlab through compiling the C program as a mex-function inside of the Matlab environment. Through this operation, the speed of the simulation was increased by a factor of 100. Another increase in speed, by a factor of 10, was obtained by changing the compiler from the standard "lcc" compiler into the Microsoft Visual Studio C++ compiler. The program was ran on a Windows XP Professional computer, thus the C compiler by Microsoft was found to perform the best. When utilizing the C mex-file for the FDTD code, the simulation ran with a speed that was comparable to, and even faster than, some FDTD codes available for download.

The two main components of the code with PML boundary conditions are given in APPENDIX B. The m-file script is similar to the initiation function for the PWE method. It requires a matrix with the inverse of the dielectric constant and the size of each grid point. Based on these two values, the script declares all of the other variables, including the PML parameters. The mex-file includes the bulk of the calculations and performs one time step. After each time step, the updated fields are returned to the Matlab environment where the fields can be plotted in real time or a value can be monitored and plotted onto the screen. Since the compiled mex-file utilizes the same location in memory as the Matlab code, the overhead of returning the simulation back

into the Matlab environment is small. However, by having access to the simulation data in real time, the powerful post processing capabilities of the Matlab environment can be utilized to perform complex analysis and functions on the data without the need to write extensive code to add into the program or to store an extremely large amount of data. A precompiled add-in for the Matlab environment with help files and example programs was created for the two dimensional TE mode FDTD with periodic, Bloch, and absorbing boundary conditions. This has been made available upon request as stated in the Appendix.

Photonic Crystal Effective Index Model

Propagation through a photonic crystal is a complex phenomenon requiring a renewed look at the current models. The index of refraction is the property used to describe propagation of light inside of a material. Since atoms and molecules are much smaller than the wavelength of light, the light only sees an average dielectric constant. The frequency response for ordinary dielectrics are dependent on resonances of the various charged entities within the material for which models have been developed to characterize its frequency response such as the Debye model[60]. Photonic crystals obey a different model for their frequency dependent properties. The lattice constant of the photonic crystal is on the same order of magnitude as the wavelength of light it is designed to operate in. Therefore, the light waves interact strongly with the geometry of the structure resulting in features such as the band gap, self-collimation, and negative index of refraction. In this section, the characteristics of the photonic crystal slab are introduced, followed by the development of an effective index model which describes the

propagation behavior of a Gaussian beam along the Γ-M direction of a square lattice photonic crystal.

Before embarking on the task of developing an effective index model for propagation through a photonic crystal, an overview of the two-dimensional photonic crystal slab is given to understand the system being simulated, fabricated, and measured. The two-dimensional photonic crystal slab is a class of photonic crystals where the periodic structure is fabricated on a thin film of high index material sandwiched between two layers of low index material. In the case of the silicon-on-insulator substrate, the high index layer is silicon (n = 3.45), the low index layer on the bottom is silicon oxide (n = 1.45), and the top layer is either air (n = 1) or another coat of oxide. The TE and TM slab modes for this structure can be calculated for a symmetrical case, and simulated for the nonsymmetrical cases[61]. These modes have an effective index which describes their propagation wave vectors. Two-dimensional band structure calculations utilizing this effective index have yielded good agreements with full three-dimensional calculations[59]. Another concern for the photonic crystal slab is the loss of the mode to the air layer and substrate layer. The coupling of the mode to an isotropic media on the top and bottom surface of the photonic crystal can be treated utilizing the allowed wave vector curve in a similar way to the refraction angle analysis. If the mode inside of the photonic crystal has a smaller wave vector than the wave vector in the free space or substrate material, the mode can couple into a radiation mode[62]. This condition is identical to the case for total internal reflection. A graphical representation for this condition is the light line drawn on the band diagram, as shown in Figure 15. The light line, or light cone in two dimensions, is the line drawn in the normalized band diagram where the magnitude of the normalized

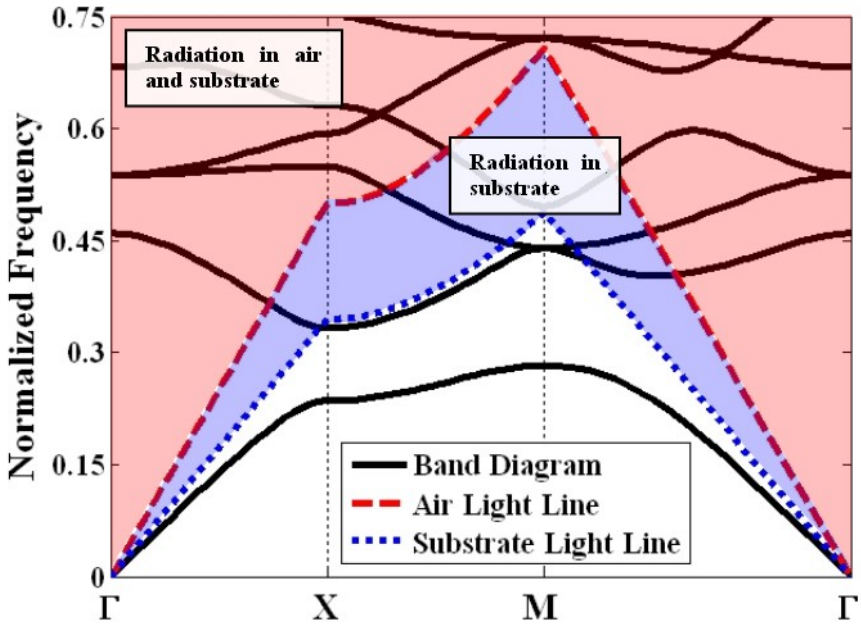

Figure 15. Band diagram showing the light line for the air and substrate radiation modes

frequency is the wave vector divided by the index of refraction of the media. All modes above the light line have the possibility of coupling into a radiation mode. From the band diagram shown, it is apparent that only the first band is entirely within the light line, while parts of the second to fourth bands remain below the light line depending on the index of the substrate. Staying under the light line is critical for a successful photonic crystal device, thus this thesis focuses on the top of the first band where it is guaranteed that the mode is always below the light line.

Figure 12 shows the shape of the allowed wave vector curves in the first band of a square lattice photonic crystal. At low frequencies, near the Γ-point or center of the Brillouin zone, the allowed wave vector curves are circular. This corresponds to the physical interpretation applied earlier that the wavelength is much greater than the periodicity resulting in an average dielectric constant felt by the wave regardless of the

direction of the wave propagation. As the wave vector approaches the edge of the Brillouin zone, the shape changes. The Γ-M direction exhibits an anomaly. As the contours are followed from the Γ point to the M point, the curvature changes from convex to concave with respect to the Γ point. At the point where the concavity changes, the curvature of the wave vector curve is zero and a beam of light will travel without spreading[30]. A model for the property of the portion of the curve beyond the self-collimation point was proposed as a material exhibiting a negative dielectric constant[39]:

$$\varepsilon = \begin{vmatrix} \varepsilon_1 & 0 \\ 0 & -\varepsilon_2 \end{vmatrix} \qquad \textbf{Equation 16}$$

This results in an allowed wave vector curve corresponding to a hyperbola. Developing this approach further, this thesis investigates the use of elliptical and hyperbolic fitting of the wave vector curve. Schematics of the model fitting utilizing the wave vector contour for a square lattice photonic crystal simulated for a silicon pillar / silicon oxide matrix slab waveguide is given in Figure 16. Models were investigated in this thesis to fit the wave vector contour with a circle, ellipse, and a hyperbola by adjusting the index of

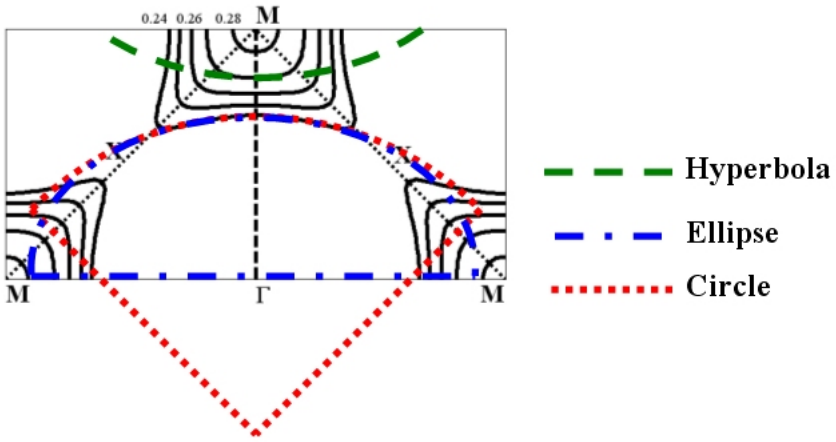

Figure 16. Models for fitting the allowed wave vector curve for the Γ-M direction

refraction. The circular fit assumes an isotropic effective index while the elliptical and hyperbolic cases are for an anisotropic index of refraction arising from different ε and μ in different crystallographic directions. Previous models fit the wave vector curve qualitatively utilizing only an effective index of refraction based on ε as the actual structure only involves a modulation of the dielectric constant[28-39]. A more general model allowing both ε and μ to affect the index was investigated.

Since only the product εμ is proportional to the index, either property can be fit for calculating the effective index of refraction. However, when considering the two-dimensional case, the set of ε and μ values which affect each polarization are fixed, thus for the TE and TM modes, the values of ε and μ used to fit the index profile are restricted. In the TM mode propagating in the z-direction and x-direction perpendicular to the plane of the slab, only the H_z, H_y, and E_x components exist, thus only the z component of the dielectric constant appears, and the shape of the wave vector contour cannot be modified from a circle without introducing anisotropy in the μ_x and μ_y values. For the TE mode, the opposite applies as an anisotropic dielectric constant is sufficient to modify the shape of the wave vector curve. Both the TM and TE mode band structure show the same concavity reversal which gives a significant conclusion that a periodic structure with modulation only in ε can result in an effective anisotropy in μ. This effect is attributed to the multiple reflections off of the curved surfaces of the periodic structure which allows a modulation in the dielectric constant to affect the evolution of the magnetic field. The models for the ε and μ are as follows:

$$\varepsilon = \begin{bmatrix} \varepsilon_x & 0 & 0 \\ 0 & \varepsilon_y & 0 \\ 0 & 0 & \varepsilon_z \end{bmatrix}, \text{ and } \mu = \begin{bmatrix} \mu_x & 0 & 0 \\ 0 & \mu_y & 0 \\ 0 & 0 & \mu_z \end{bmatrix} \qquad \textbf{Equation 17}$$

Curve fitting of the wave vector curves were utilized to calculate the following effective index values:

$$n_{circle} = \sqrt{\varepsilon\mu}$$

$$n_{propagation\_ellipse/hyperbola} = n_{phase} = \left|\frac{\omega}{k}\right| = \sqrt{\varepsilon_x \mu_y}_{TM\_Mode} = \sqrt{\varepsilon_y \mu_x}_{TE\_Mode}$$

$$n_{transverse\_ellipse/hyperbola} = n_{trans} = \sqrt{\varepsilon_x \mu_z}_{TM\_Mode} = \sqrt{\varepsilon_z \mu_x}_{TE\_Mode} \qquad \textbf{Equation 18}$$

where n_{circle} is positive for convex and negative for concave curvature; n_{phase} is the same for both elliptical and hyperbolic fits; and n_{trans} is real for elliptical and imaginary for hyperbolic fit. Z-direction propagation was assumed for these calculations. Utilizing these models for the index of refraction, the parabolic wave equation was solved for propagation of a Gaussian beam. The circular fit model simply replaces the index of refraction with that calculated from the curvature. The beam size, longitudinal phase, and radial phase parameters for the Gaussian beam utilizing the circular fit model are:

$$w_{circle}^2(z) = w_0^2\left(1 + \left(\frac{z\lambda_0}{\pi n_{circle} w_0^2}\right)^2\right)$$

$$\Phi_{longitudinal\_circle}(z) = -\frac{\tan^{-1}\left(\frac{z\lambda_0}{\pi n_{circle} w_0^2}\right)}{2} + \frac{2\pi n_{circle}}{\lambda_0} z$$

$$\Phi_{radial\_circle} = \frac{\pi n_{circle} y^2}{z\left(1+\left(\frac{\pi n_{circle} w_0^2}{z\lambda_0}\right)^2\right)} \qquad \textbf{Equation 19}$$

where the w_0 is half of the beam size at the waste; and λ_0 is the wavelength in free space. For the elliptical and hyperbolic case, the conventional approach to solving this problem includes a coordinate transformation to restate the problem into an isotropic index in an anisotropic coordinate system[64,65], but for the case considered here where only the Γ-M direction is of interest, the problem can be solved without a coordinate transformation and intuitive results can be obtained. First, all of the ε and μ are normalized to the z-axis values as propagation in the z-direction is assumed:

$$\varepsilon = \begin{bmatrix} \varepsilon_x & 0 & 0 \\ 0 & \varepsilon_y & 0 \\ 0 & 0 & \varepsilon_z \end{bmatrix} = \varepsilon_z \begin{bmatrix} \varepsilon_{x/z} & 0 & 0 \\ 0 & \varepsilon_{y/z} & 0 \\ 0 & 0 & 1 \end{bmatrix}$$

$$\mu = \begin{bmatrix} \mu_x & 0 & 0 \\ 0 & \mu_y & 0 \\ 0 & 0 & \mu_z \end{bmatrix} = \mu_z \begin{bmatrix} \mu_{x/z} & 0 & 0 \\ 0 & \mu_{y/z} & 0 \\ 0 & 0 & 1 \end{bmatrix} \qquad \textbf{Equation 20}$$

Then, the normalized values can be used to obtain a value for the divergences of the fields, which are not zero anymore due to the anisotropic media:

$$\nabla \bullet E = \left(1-\varepsilon_{x/z}\right)\frac{\partial E_x}{\partial x} + \left(1-\varepsilon_{y/z}\right)\frac{\partial E_y}{\partial y}$$

$$\nabla \bullet H = \left(1-\mu_{x/z}\right)\frac{\partial H_x}{\partial x} + \left(1-\mu_{y/z}\right)\frac{\partial H_y}{\partial y} \qquad \textbf{Equation 21}$$

Substituting these values into the wave equation form of the Maxwell's Equation and making the two-dimensional approximation in the x-direction, the following two equations can be obtained for the TE and TM, modes respectively:

$$\frac{\partial^2 E_x}{\partial y^2} + \mu_{z/y}\left(\frac{\partial^2 E_x}{\partial z^2} + k^2 E_x\right) = 0$$

$$\frac{\partial^2 H_x}{\partial y^2} + \varepsilon_{z/y}\left(\frac{\partial^2 H_x}{\partial z^2} + k^2 H_x\right) = 0 \qquad \textbf{Equation 22}$$

Only one extra factor, the $\mu_{z/y}$ and $\varepsilon_{z/y}$ is necessary to account for the anisotropy in the material. Solving for the Gaussian beam parameters results in[63]:

$$w^2_{ellipse/hyperbola}(z) = w_0^2\left(1 + \left(\frac{z\lambda_0}{\pi n_{factor}\, n_{phase} w_0^2}\right)^2\right)$$

$$\Phi_{longitudinal\_ellipse/hyperbola}(z) = -\frac{\tan^{-1}\left(\frac{z\lambda_0}{\pi\, n_{factor} n_{phase} w_0^2}\right)}{2} + \frac{2\pi\, n_{phase}}{\lambda_0} z$$

$$\Phi_{radial\_ellipse/hyperbola} = \frac{\pi n_{factor} n_{phase} y^2}{z\left(1 + \left(\frac{\pi n_{factor} n_{phase} w_0^2}{z\lambda_0}\right)^2\right)}$$

$$\text{where, } n_{factor} = \left(\frac{n_{trans}}{n_{phase}}\right)^2 = \mu_{z/y\_TM\_Mode} = \varepsilon_{z/y\_TE\_Mode} \qquad \textbf{Equation 23}$$

The form of the solution parallels the solution for the isotropic case with the appropriate index factor placed in the appropriate locations. Even though the solution is rather trivial, the interpretation provides extensive insight into the propagation properties of the Gaussian beam in such an anisotropic media.

The case for the circular fit is discussed first for reference. Since the index was increased for this case compared to the n_{phase} value which can be determined from the ω and k values directly, the circular model predicts that the beam can travel an increased length by a factor of n_{circle}/n_{phase} while maintaining the same beam spread since substitution of z by zn_{circle}/n_{phase} returns the equation back to the case for an isotropic material where the index of refraction is the same as the phase velocity index of refraction. The main discrepancy of this model is in the longitudinal component of the beam, which oscillates at unrealistically short wavelengths as n_{circle} increases near the self-collimation point. The concavity reversal can be handled by a negative index of refraction which is interpreted physically as reverse propagation of the phase components of the beam with direction. The amplitude and beam size are not affected as the index is squared. The radial phase trend works well with this convention, but the longitudinal phase incurs another nonphysical attribute for this case as the wave vector is clearly pointing in the positive z-direction.

The elliptical model resolves the discrepancies in the longitudinal phase. All of the index factors are positive and the n_{factor} increases as the curvature decreases in the model. The effect of the n_{factor} is to effectively increase the length of propagation, z, so that the beam can propagate n_{factor} times longer with the same beam size and radial phase difference compared to an isotropic material with an index of n_{phase}. For this model to be consistent with the circular model, n_{factor} must be equal to n_{circle}/n_{phase}, which can be proved geometrically. The $\tan^{-1}$ factor in the phase also follows this trend, but this factor is small compared to the dependence of the phase with z due to propagation. The elliptical case preserves the wavelength of the phase fronts with the wave vector

regardless of the curvature, thus resolving the nonphysical modification of the wave fronts in the circular model. To account for the change in curvature, n_{trans} is allowed to become imaginary, resulting in a hyperbolic fit of the wave vector curve. The same interpretation results in describing the beam size and radial phase as traveling in a negative direction as n_{factor} becomes negative for this case. However, the phase fronts still maintain their positive direction since the n_{factor} does not enter the second component of the longitudinal phase. The key component of the modeling is to discern the source of the forces confining and ultimately reversing the normal flow of the beam spread and radial phase in the photonic crystal. Through the model, it is apparent that for waves traveling in the Γ-M direction of a square lattice photonic crystal, ε_z and μ_z increase, reach an asymptote, and then become negative to account for the change in concavity. An interesting result of the theory which is outside of the scope of this thesis pertains to metallic structures. Since metals are modeled by a negative dielectric constant, the model predicts that by introducing conductivity in one-dimension, by having conductive wires with radii much smaller than the wavelength of light strung in the direction of propagation, propagation phenomena following the hyperbolic model fit can be observed. The properties of such a media have been investigated and confirmed to show negative dielectric constant[37,67]. The approach is a simplified approach compared to that theorized by Vesalagos[66] and obtained through the use of split-ring resonators which produce both a negative effective dielectric constant and magnetic permeability in the radio frequency regime[67-69].

To verify the accuracy of the model, the beam width, longitudinal phase, and radial phase obtained from fitting the allowed wave vector surface calculated through the

PWE method were correlated to the parameters calculated from a simulated Gaussian beam in a FDTD simulation. The photonic crystal investigated was a square lattice photonic crystal with a high index pillars with ε = 12 and r = 0.2a in a matrix with ε = 2. The choice of the structure is discussed in more detail in the device and application section. The allowed wave vector curves shown in Figure 16 were calculated for this structure. Figure 17 plots the effective index values calculated. The beam width after propagation through 5000 grid points, corresponding to a distance of 250*sqrt(2)*a, shows excellent agreement with the calculated values for both models, as expected since they both fit the geometrical curvature. The value obtained from the FDTD simulation oscillates around the model fit, as shown in Figure 18 and 19. The longitudinal and radial phases also followed the trend expected from the model, with the circular fit model resulting in a completely nonphysical interpretation of the longitudinal phase while the elliptical and hyperbolic fit successfully modeled all aspects of the beam. The oscillations in the data are attributed to interference from other wave vector components

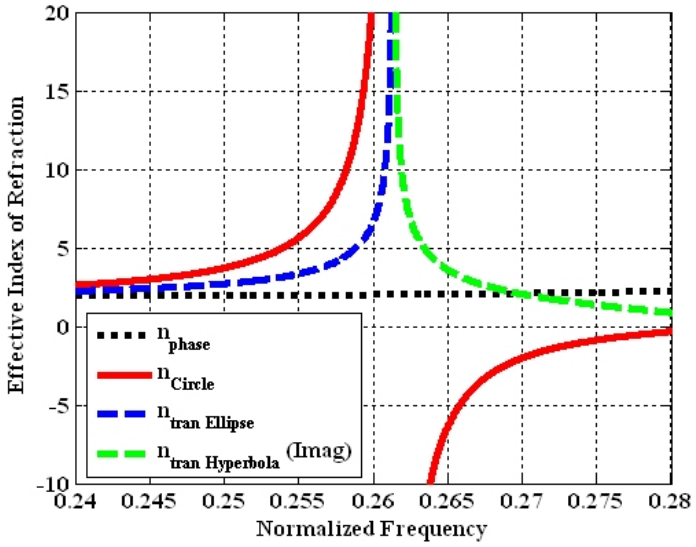

Figure 17. Effective index values calculated for the square lattice photonic crystal

due to the excitation of Bloch modes outside of the first Brillouin zone and also from insufficient time in the simulation to capture some of the slow group velocity modes. The simulation time could not be increased to avoid detecting reflected signal from the back plane of the photonic crystal.

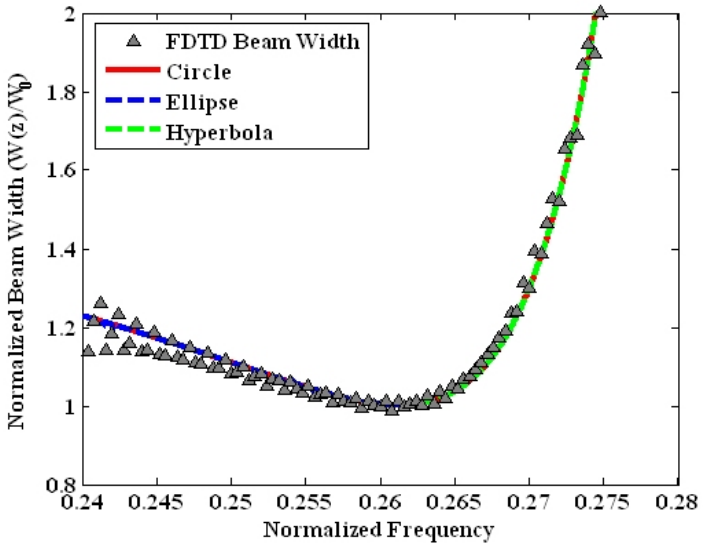

Figure 18. Beam width correlation between the model and FDTD simulation

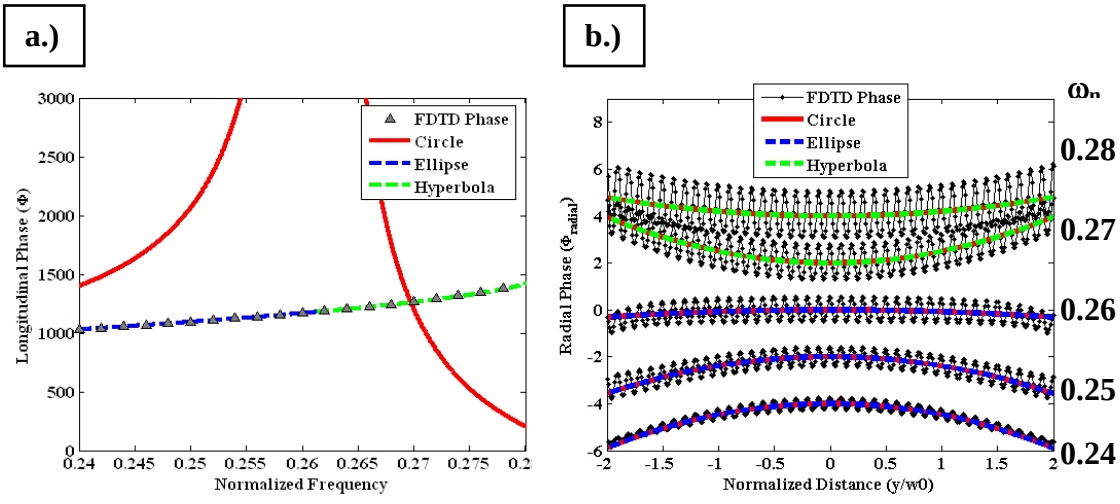

Figure 19. Phase correlation between the model and the FDTD simulation

Self-Collimation in the Square Lattice Photonic Crystal

Before proceeding to practical concerns for the applicability of self-collimated beams to integrated optical devices, a survey of the range of square lattice photonic crystals exhibiting self-collimations was conducted. A range of simulations were conducted for square lattice structures with circular holes and pillars. The size of the circle was varied from 0.1a to 0.4a and the index of refraction for the high index material was varied from 1.25 to 4. The low index material was given an index of 1 corresponding to free space.

The results for the case of pillars are plotted on the three-dimensional surface contours in Figure 20. The main feature for the normalized frequency of the self-collimation point, the point where the curvature reverses, is that the TE mode has a definite cut-off where self-collimation starts, while the cut-off for the TM mode either does not exist or is small enough to be inconsequential in realistic structures. The self-collimation point remains nearly parallel between the two modes and decreases in frequency with increasing index contrast and radius of the pillars. Up to a radius of 0.4a,

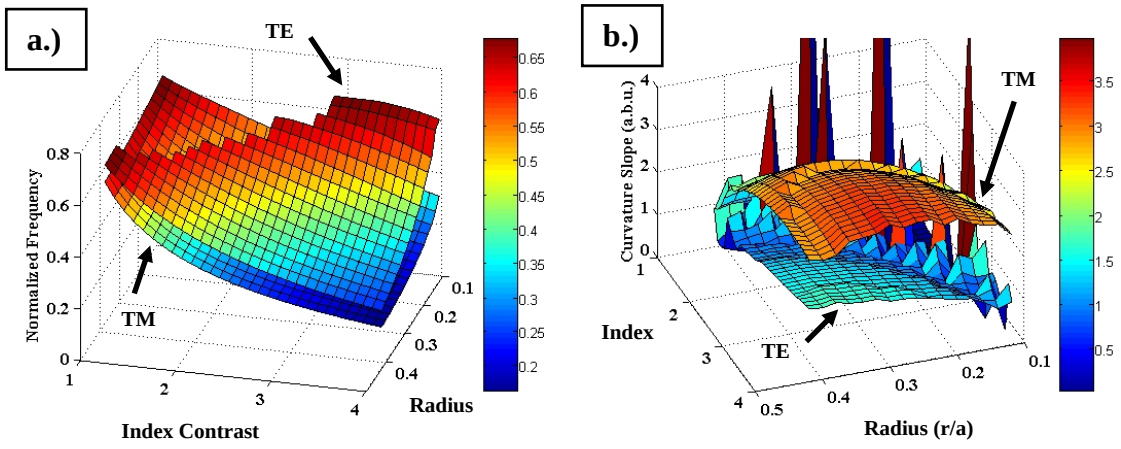

Figure 20. The normalized frequency of the self-collimation point and the slope of the curvature for a square lattice photonic crystal made of high index pillars

which is close to the limits of reliable fabrication, this trend is conserved. The second graph shows the magnitude of the change in curvature with respect to the frequency scaled to arbitrary units. This value is proportional to the width of the self-collimation. For the case of pillars, the TM mode shows strong self-collimation effects. The TE mode can show self-collimation, but the range of frequencies exhibiting the self collimation is much smaller than the TM mode. However, since the TE mode always lies above the TM mode, this structure can be optimized so both the TE and TM modes show self-collimation by adjusting the slab thickness. The TE mode always has the higher effective slab mode index; thus for very thin slabs, the TM mode will have a higher self-collimation frequency due to a lower effective index. As the slab thickness is increased, the effective indices for the two modes approach the bulk index of refraction where the TM mode has a lower self-collimation frequency. At an optimal slab thickness, self-collimation occurs at the same frequency for the two modes. Also, the pillar structure has a very strong band gap effect in the TM mode allowing for a wide range of phenomena to be investigated utilizing this structure[52]. Therefore, this structure was investigated in further simulations to demonstrate the functionality of combining the self-collimation and the band gap effects.

The results for the hole structure, shown in Figure 21, reveal a very different behavior for this structure. The self-collimation point is relatively independent of the polarization of light and the hole radius, and dependent almost entirely by the refractive index of the slab. This insensitivity to the radius is due to the balancing of two competing effects. Increasing the hole diameter decreases the average index of the slab, thus increases the frequency of the self-collimation point. However, an increase in the

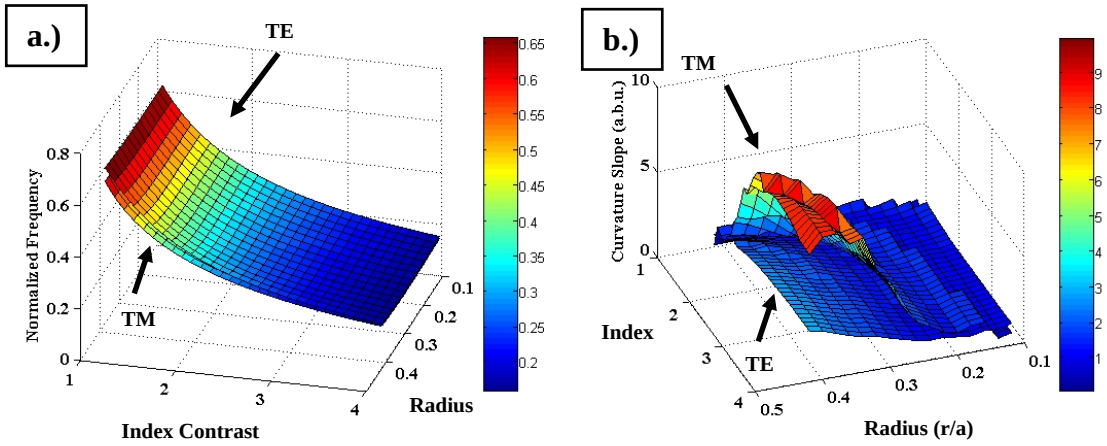

Figure 21. The normalized frequency of the self-collimation point and the slope of the curvature for a square lattice photonic crystal made of low index holes

radius also increases the contrast of the modulation, which pushes down the self-collimation point. For the pillar structure, these two effects affect the self-collimation in the same direction causing the bands to be dependent on both the index and the pillar diameter. The slope of the curvature reveals that the TM mode for the hole structure exhibits a much larger self-collimation width than the TE mode and both of the modes in the pillar structure. Due to its insensitivity on the hole radius and the larger bandwidth exhibiting self-collimation, the structure with holes is a better candidate for demonstrating the self-collimation effect and is the structure fabricated and tested.

Robustness of the Self-Collimation Effect

Figure 22 shows the photonic crystal slab structure that was investigated throughout the rest of the simulation section. This structure consists of cylindrical pillars arranged in a square lattice. Even though this structure is less robust to error than the hole structure, it exhibits a large band gap which is desirable in applications. Structures using silicon ($\varepsilon = 11$) and silica ($\varepsilon = 2$) were chosen to ensure compatibility with

conventional semiconductor processes where the dielectric constant of silicon was set lower than its value of 12.1 at 1.55 μm to account for the out of plane confinement. A rigorous solution for the effective index is not determined since the thickness of the slab is considered a variable to match the application. Since the effective index method results in lower indices for the high index material, a value for the index slightly lower than the bulk was utilized.

The PWE method was utilized to calculate the TM band structure. 625 terms of the expansion were used to provide sufficient accuracy for design purposes. The geometry in Figure 22 was simulated using silicon pillars in silica and silica pillars in silicon. The band structures and allowed wave vector curves for the pillar radii varying from 0 to 0.5a were calculated. The structure with silicon pillars of radius 0.2a in a silica matrix was found to exhibit strong self-collimation in the Γ-M direction on the top edge of the first band for the TE polarization. The band diagram and allowed wave vector curves for this structure are shown in Figure 23. Between normalized frequencies of 0.28 and 0.33, a band gap exists where any incident beam will be totally reflected. The section of the band diagram below the band gap and between the X and M frequencies

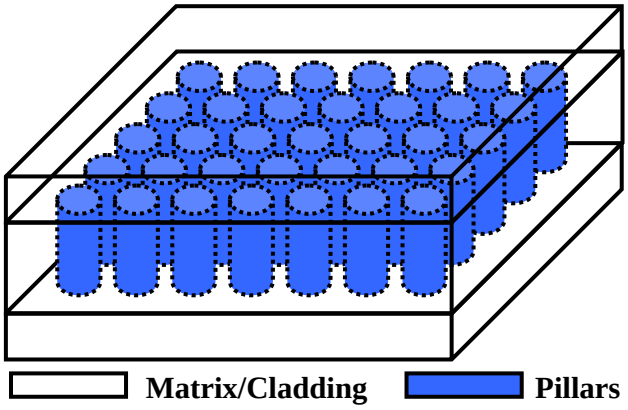

Figure 22. Schematic of the photonic crystal slab investigated[36]

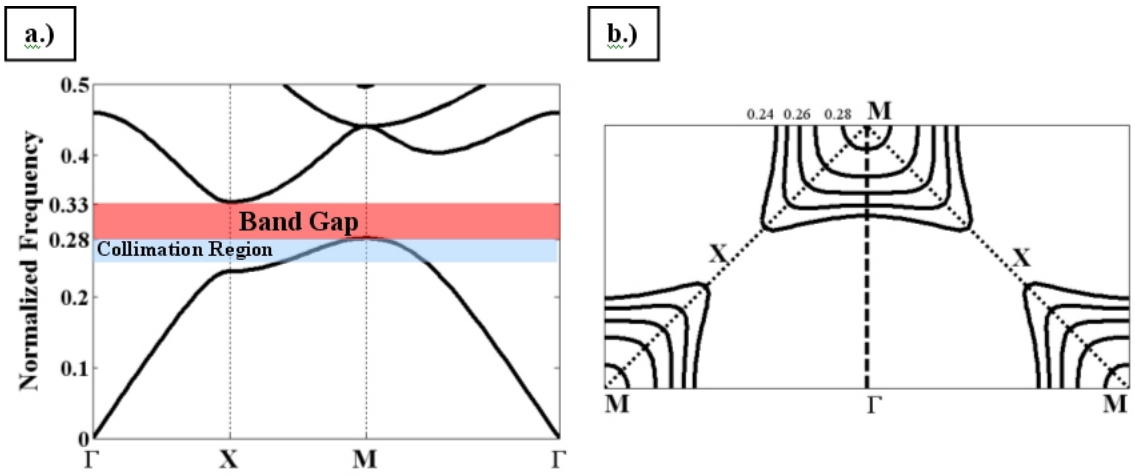

Figure 23. The band diagram and the allowed wave vector curves for the photonic crystal slab[36]

(ω_n = 0.24~0.28) exhibits self-collimation. The allowed wave vector curves shown change from convex to concave along the Γ-M line (dashed bold line) as the frequency is increased from ω_n = 0.24 to ω_n = 0.28. The allowed wave vector curve for ω_n = 0.26 is completely flat and normal to the Γ-M line. Therefore, a Gaussian beam incident on the photonic crystal along the diagonal of the unit cell with a normalized frequency of 0.26 is expected to exhibit the highest degree of self- collimation. The most common wavelengths for optical signals are 850 nm, 1.3 μm, and 1.55 μm. However, since silicon absorbs light below 1.06 μm, only the 1.3 μm and 1.55 μm cases were considered. The lattice constant, a, to achieve self-collimation for the design wavelength was then determined by equating the design wavelength to a normalized frequency of 0.26. The formula for the normalized frequency was rearranged to give $a = \omega_n\lambda$, where λ is the wavelength of the incident radiation. The lattice constants were 0.338 μm and 0.403 μm for 1.3 μm and 1.55 μm wavelengths, respectively. The silicon pillars (r = 0.2a) have diameters of 135.2 nm and 161.2 nm respectively, which are within the processing capability of state of the art lithography. The values for 1.55 μm incident wavelength are

used throughout the rest of this section, but all conclusions can be directly applied to a system with 1.3 μm wavelength by scaling the structure accordingly.

The Gaussian beam full width at half max (FWHM) utilized throughout this section was 300 grid points wide or about 8.5 μm for the 1.55 μm incident wavelength. This width corresponds to mode field radii of available single mode available and is a realistic beam width for analysis. To verify the self-collimation predicted by the PWE simulation, an FDTD simulation grid was created using 20 grid points for each side of the non-primitive unit cell containing two pillars diagonally placed for propagation in the Γ-M direction. The Courant stability limit was utilized for the time step. Figure 24 depicts the plot of the time-averaged electric field intensity pattern of a Gaussian beam propagating in an isotropic slab of silica compared to inside of a photonic crystal for normalized frequency of 0.26. After propagation through 120 μm, or 4250 grid points, no observable spreading occurred in the photonic crystal compared to significant spreading in the silica slab.

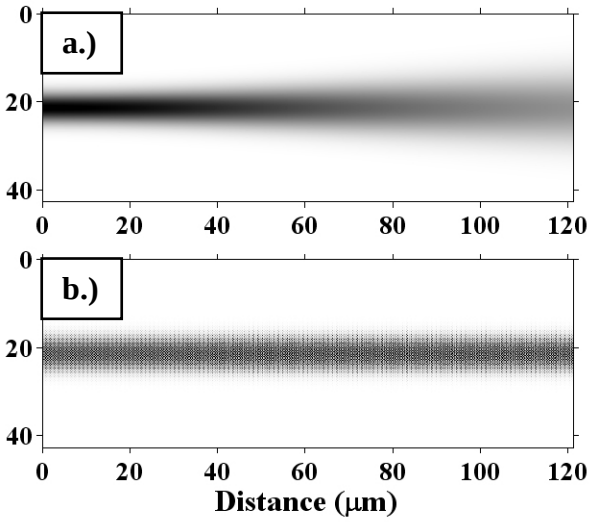

Figure 24. Propagation of a Gaussian beam in a.) silica and b.) photonic crystal slab[36]

Many proposed integrated optics devices rely on resonance for achieving their functionality. This factor contributes to very stringent fabrication tolerances that make applications of these devices difficult beyond the simulation realm. Photonic crystals also suffer from this difficulty in applications utilizing defect resonant modes, where a small deviation in size or spacing can dramatically change the performance of the device. However, self-collimation occurs in a photonic crystal over a range of frequencies, so small errors can be accommodated. A FDTD grid measuring 3000x7000 grid points was filled with the photonic crystal except for a 70 grid wide region of isotropic silica denoting the input plane. The beam width was recorded after propagation through 6000 grid points, or 171 μm, from the incident plane and compared to the incident beam width for a photonic crystal filled grid and with several isotropic media. The beam width expansion after traveling 171 μm as a function of wavelength is plotted in Figure 25. The range of wavelengths where the beam spread is under 20% ranges from 1.525~1.575 μm. Self-collimated beams exhibit a dramatic decrease in the beam expansion over a wide frequency range compared to the case of pure air, silica, and silicon. The degree of beam

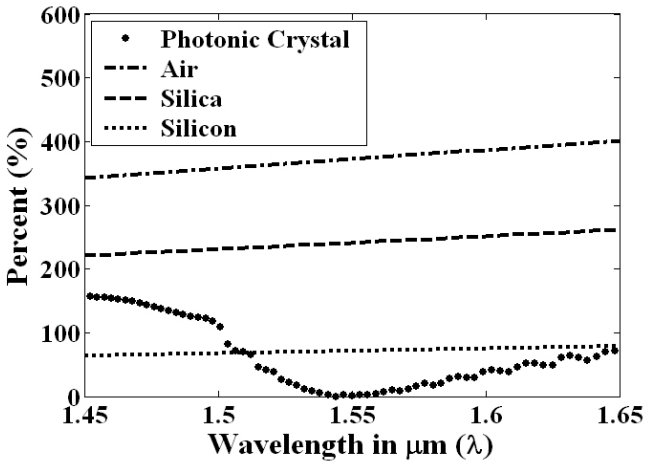

Figure 25. Beam spreading in a photonic crystal compared to isotropic media[36]

spreading in isotropic media was calculated using the Gaussian beam spread equation:

$$w^2(z) = w_0^2\left[1+\left(\frac{\lambda_0 z}{\pi n w_0^2}\right)^2\right] \qquad \textbf{Equation 24}$$

where $2w_0$ is the FWHM at the beam waist; $2w(z)$ is the FWHM after traveling a distance z; and n is the index of refraction of the isotropic media.

Two types of errors are investigated in this study: systematic error and random error. Systematic error was modeled as a uniform increase/decrease of the pillar size which can result in fabrication from over or under development or exposure of the photoresist as well as subsequent etch or deposition processes. All other factors remained constant compared to the previous simulation. Systematic errors of ±5% and ±2.5% were simulated and the results plotted in Figure 26. For 2.5% error in either direction, the additional beam spread at 1.55 μm was only 10%. The general shape of the beam expansion curve remained constant while larger pillar diameters shift the minimum beam expansion towards longer wavelengths due to an increase in the average refractive index that lowers the band structure. The data for the ±5% error show that the beam expansion

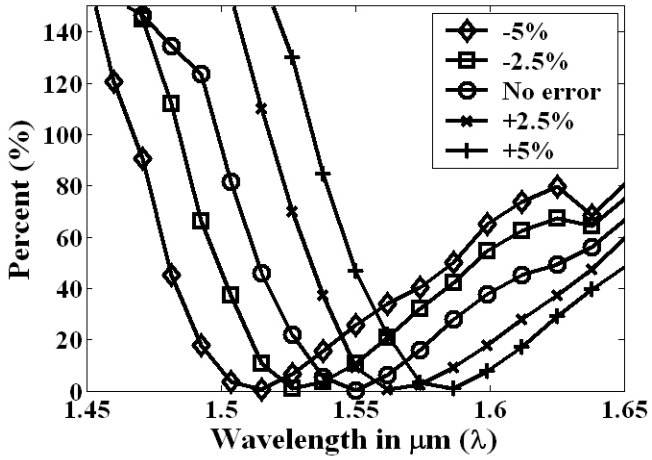

Figure 26. Beam spreading as a function of the wavelength for systematic errors[36]

is more sensitive to positive error in radius than a negative error. This is due to the higher slope of the beam expansion curve towards the shorter wavelength. In addition, an increase in the radius increases the mean dielectric constant by a larger factor than a decrease in the radius decreases its value. With a -5% error, the beam width increases by less than 30%. Even with a 5% error in the pillar sizes, the overall shape of the curve is intact so a tunable laser can be used to compensate for the error. Such robustness is rare in resonant optical devices where a large Q factor is necessary to achieve good device performance resulting in a very narrow band of operational frequencies[14].

In addition to systematic errors, random errors were simulated. Random errors can occur at any step of the fabrication process where deviations or fluctuations within a process step can introduce error among the features. Random and normal distributions of the diameter about the mean value at ±2.5% and ±1.25% were simulated. For the random distribution, the pillar diameters were uniformly distributed between the two extremes values in the range. In the normal distribution, the pillar sizes follow a normal "bell curve" distribution with a standard deviation of 2.5% and 1.25%, respectively. For each distribution, a set of five simulations were conducted and averaged. The results for the two distributions of pillar sizes are graphed in Figure 27. The ±1.25% case retains good collimation with a slight shift towards longer wavelengths, but the ±2.5% case results in large scattering resulting in the beam losing its confinement. The shift of the minimum beam expansion wavelength was attributed to the higher average index resulting from the area of the dielectric showing an asymmetric relation to the radius. The results for the normal error distribution show that with only 1.25% error, the beam loses its self-collimating characteristic. The normal distribution has a finite probability of pillars that

are significantly larger or smaller than the average size. When a pillar has high deviation from its surroundings, it acts as an effective scattering center rather than a slight perturbation. The analysis of error tolerance reveals that systematic error results in a shifting of the self-collimation wavelength and that small random errors among the pillar sizes are acceptable, but even a small number of pillars with large deviations from the mean size can destroy the performance. A ±2 nm variation in pillar diameters can be accommodated while retaining good self-collimation[36].

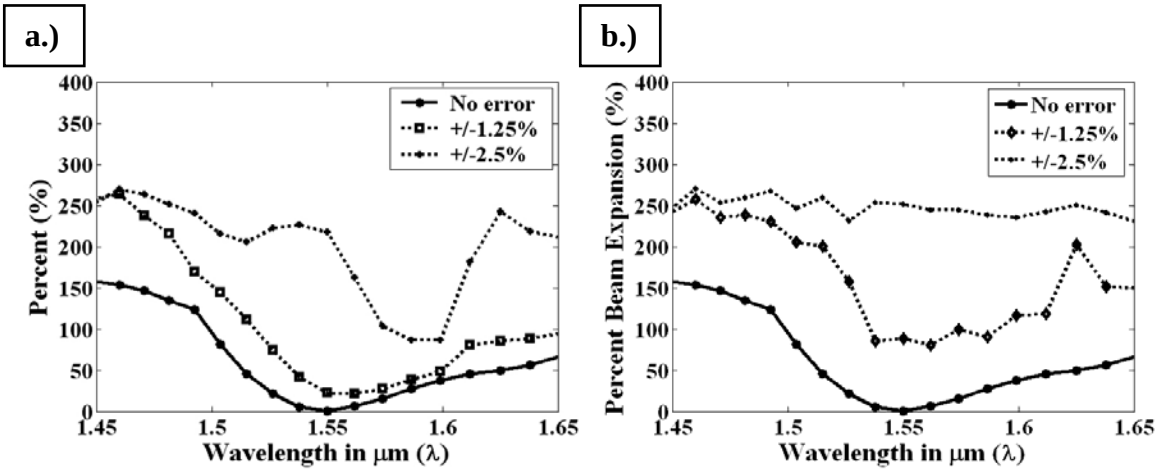

Figure 27. Beam spreading as a function of error magnitude for a.) random distribution and b.) normal distribution of pillar sizes[36]

Application of Self-Collimated Beams

The ability to propagate a beam freely in a material without the need for waveguides makes feasible applications unimaginable with conventional optical materials. The applications discussed in this thesis are optical interconnects and Fabry-Perot interferometer for beams with width of the same order of magnitude as the wavelength of light.

Optical Interconnects

Two of the major challenges for integrating optical devices onto a chip are the difficulty of routing an optical signal and the high sensitivity to misalignment when coupling into a waveguide. In addition, crosstalk between waveguides in proximity, losses from sharp turns, and cross-coupling when signals intersect make optical routing difficult. A system of self-collimated beams in a photonic crystal forms the ideal platform for optical signal routing which addresses these issues. Optical signals are more difficult to route compared to electrical signals due to restrictions on the radius of curvature of turns in a waveguide. Optical integrated devices are much larger than their electrical counterparts due to the inability to route signals in a compact manner. Semiconductor waveguides using high-index materials offer better performance, but suffer from difficulties in coupling, such as misalignment and coupling loss from silica and polymer low-index waveguides. Self-collimated beam in a photonic crystal provides a novel media that is ideal for routing optical signals compatible with free space and low-index waveguides.

One advantage of photonic crystals originates from its symmetric, periodic structure. Rotations of 90° in square symmetry are invariant, resulting in self-collimated beams traveling in orthogonal directions. This inherent orthogonality creates a convenient Cartesian coordinate system to facilitate device design. In addition, the inherent grid system insures that devices and features are perfectly aligned with the propagation direction.

Sharp 90° turns with no loss are one of the main advantages touted for photonic crystal line defect waveguides[12,19]. Self-collimated beams can also be bent towards a

symmetrically equivalent direction through total internal reflection by an interface with a lower index media[31,33,34]. A perfect mirror is also formed by a photonic crystal with a band gap in the frequency range of interest. For the case of the silicon-silica structure investigated, an increase in the radius of the silicon pillars to 0.3a is sufficient to shift the band gap down to coincide with the self-collimating frequencies of the original structure as shown in Figure 28. The band gap extends between normalized frequencies of 0.24 and 0.28 corresponding to the region of self-collimation in the original structure. By increasing the radius of a diagonal or triangular area intersecting the path of the self-collimated beam, perfect reflection into a perpendicular direction can be accomplished. Figure 29 shows the structure and the calculated intensity profile of a 1.55 μm beam making a 90° bend. The intensity difference between the input and output beams is due to interference between the incident and reflected beams. The transmission coefficient and the beam width expansion after traveling 85.6 μm and one 90° turn are shown in Figure 30. The beam maintains its collimation and intensity even after reflection from

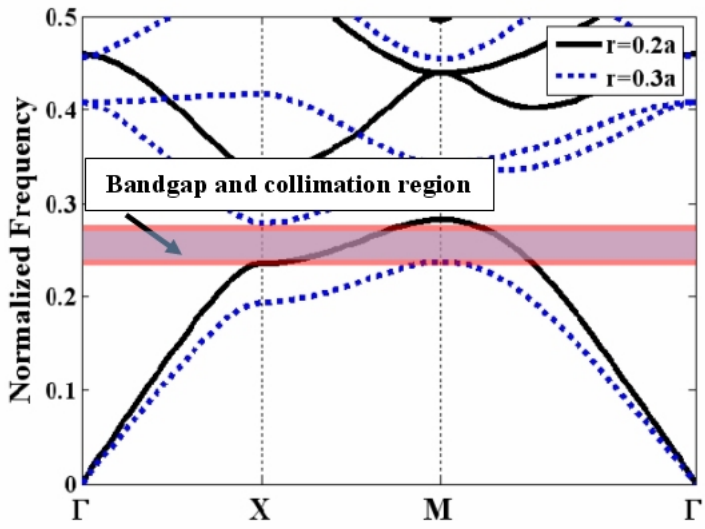

Figure 28. Band diagram showing the band gap for r = 0.2 and r = 0.3 in the silicon/silica structure[36]

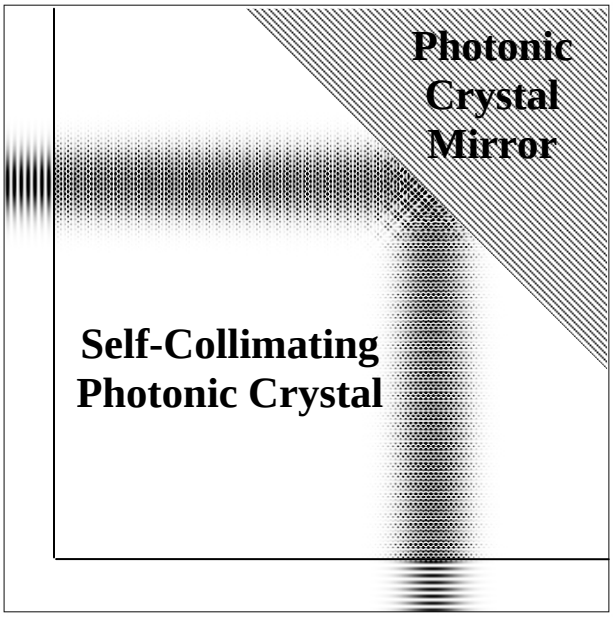

Figure 29. A plot of the intensity of a 90° reflection of a self-collimated beam by a band gap photonic crystal simulated by FDTD[36]

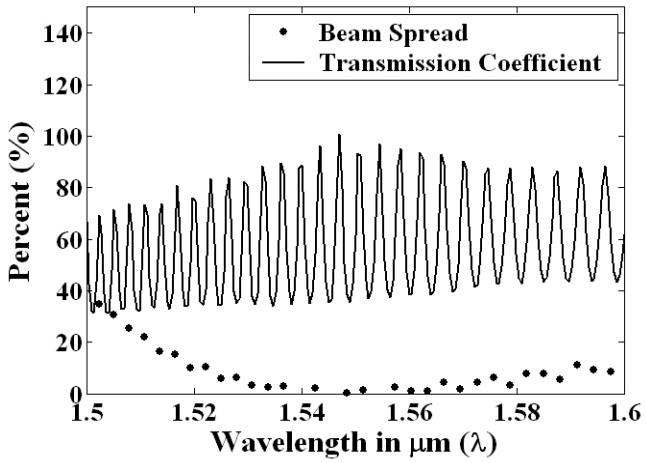

Figure 30. Beam spread and transmission coefficient for a Gaussian beam traveling through 85.6 μm and one 90° turn[36]

the photonic crystal mirror and shows an oscillation in the transmission coefficient due to Fabry-Perot type interference.

In addition to sharp turns, the self-collimated beam system has the unique advantage among waveguiding structures of allowing beams to cross each other with no coupling, akin to free space optics. Figure 31 illustrates two self-collimated beams traveling through a square photonic crystal. This unique combination of guiding and propagation behavior allows compact routing of signals on one optical signal plane rather than having to use complex three dimensional structures to avoid signal crossings.

To demonstrate the potential of this system for routing optical signals, a permutation of three parallel beams switching the output location of the first and third beam was conducted using the FDTD method with the results shown in Figure 32. Beam widths of 9.97 μm, 8.55 μm, and 7.12 μm along with wavelengths of 1555 nm, 1550 nm,

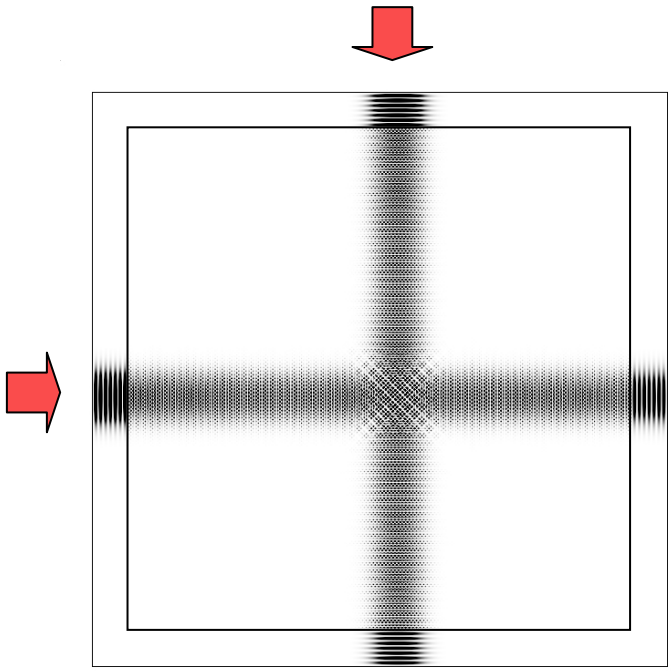

Figure 31. Non-interacting crossing of self-collimated beams[36]

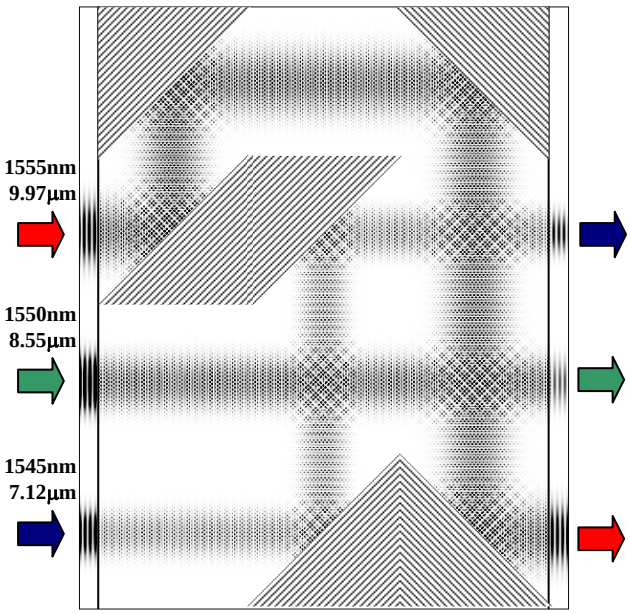

Figure 32. Routing three parallel beams with different wavelengths and widths within a single signal layer using the photonic crystal virtual waveguide[36]

and 1545 nm, respectively, were used. This device requires an area spanning only 91.2 μm×68.4 μm and a single layer as opposed to other waveguiding methods which could take mm^2 or even cm^2 worth of area and two layers to accomplish the same task[36].

Fabry-Perot Interferometer

Resonant optical cavities are utilized extensively for laser cavities and interferometers. These high Q-factor cavities provide the frequency selectivity necessary for dense wavelength division multiplexing (DWDM) applications. Recently, guided-wave interferometers, such as the ring resonator[70], have garnered high attention due to their attractiveness for miniaturization and integration. By utilizing the self-collimation properties of photonic crystals[30-36], beam spread is significantly reduced allowing for the extension of conventional optical devices, such as the Fabry-Perot Interferometer (FPI), to beam size ranges in the micron regime.

The Fabry-Perot Interferometer operates through constructive and destructive interference of the multiple reflections from the end mirrors. For normal incidence on a symmetric FPI, the transmission is given by the equation:

$$T = (1-R)^2 \Big/ \left\{ (1+R)^2 + 4R\sin^2\left(\frac{2\pi n_p d}{\lambda}\right)\right\} \qquad \textbf{Equation 25}$$

where T is the fraction of the power transmitted, R is the power reflectivity of the end mirrors, n_p is the phase velocity index of refraction, d is the physical length of the cavity, and λ is the wavelength of light. The resonant modes are given by the equation, $\nu_q = qc/2n_pd$, where ν is the resonant frequency of the q^{th} mode in Hz, q is the integer mode number and c is the speed of light. The free spectral range (FSR) follows the equation $\nu_q - \nu_{q-1} = c/2n_gd$, where n_g is the group velocity index of refraction. A lossless FPI displays 100% transmission for the resonant mode with the Airy function transmission peak. The reflectivity of the mirrors determines the sharpness of the peak and the degree of extinction of the wavelengths between the modes.

Two-dimensional finite difference time domain was used to characterize photonic crystal based FPIs. A cavity with length of 23.1 μm was constructed using the r = 0.2a photonic crystal. Two photonic crystal FPIs, one with end mirrors and one without end mirrors were simulated. Two rows of staggered pillars with r = 0.3a which has a reflectivity between 80-85% in the wavelength range from 1.5 μm to 1.6 μm was used for the end mirrors. A corresponding FPI with the end mirrors and silica replacing the photonic crystal in the cavity was simulated for comparison. To achieve the same FSR, the cavity length was increased to 61.2 μm. These three interferometers were simulated using incident radiation of a plane wave and an 8.5 μm wide Gaussian beam. The results

for the transmitted power are given in Figure 33. The plane wave incident condition simulates a large beam, such as those >0.5 mm, where the wave front is approximately a plane wave. For this case, the two FPIs with mirrors both have near unity transmittance for resonant modes. The high group velocity index of refraction of the photonic crystal results in a much shorter cavity length to achieve the same FSR. The mismatch in the mode location for the case without the mirror reveals a phase shift upon reflection which is not a multiple of π. In addition, the mode spacing in the photonic crystal is not uniform due to the highly dispersive characteristics near the band edge where self-collimation occurs. The results differ drastically when the beam width is decreased to 8.5 μm. Without the photonic crystal, the FPI loses significant intensity due to significant beam spreading within the resonant cavity. The transmitted intensity at the center of the beam is only 16% whereas the photonic crystal FPI retains over 98% transmitted intensity at 1.55 μm. The gradual reduction of the peak intensity away from 1.55 μm corresponds to the decreasing effectiveness of the self-collimation phenomenon away from the center wavelength. The intensity profiles for the electric field in the two cases

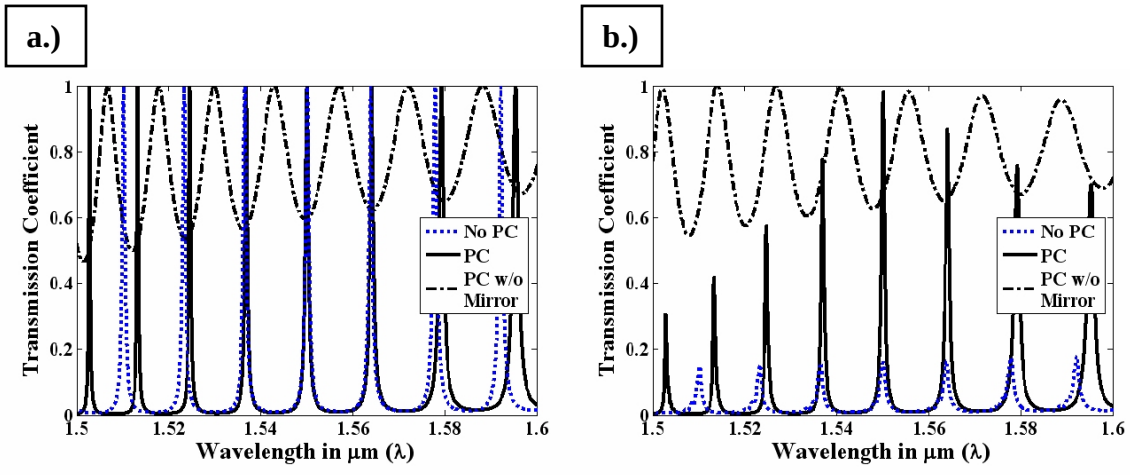

Figure 33. Transmission properties for photonic crystal FPI with a.) plane wave incidence and b.) an 8.5 μm wide Gaussian beam

with the mirror in Figure 34 show the significant beam spread within the structure without the self-collimation.

A photonic crystal based FPI allows the extension of the conventional FPI down to a beam width on the same order of magnitude as the modes inside of a fiber as well as to sizes readily obtained using ball lenses and microlenses. By tailoring the degree of self-collimation and taking advantage of the highly nonlinear dispersive properties of the photonic crystal, a single channel of a DWDM signal can be selected. Significant miniaturization of optical add/drop devices can be achieved by combining with optical circulators. One of the most promising applications is the ability to perform "free-space-like" optics in a planar lightwave circuit utilizing self-collimated beams and devices based on the self-collimation effect, like the photonic crystal FPI[36].

Photonic crystal based Fabry-Perot interferometers have the potential to overcome the significant losses resulting from beam spreading in conventional Fabry-Perot interferometers. The ability to miniaturize conventional optical devices, tailor the

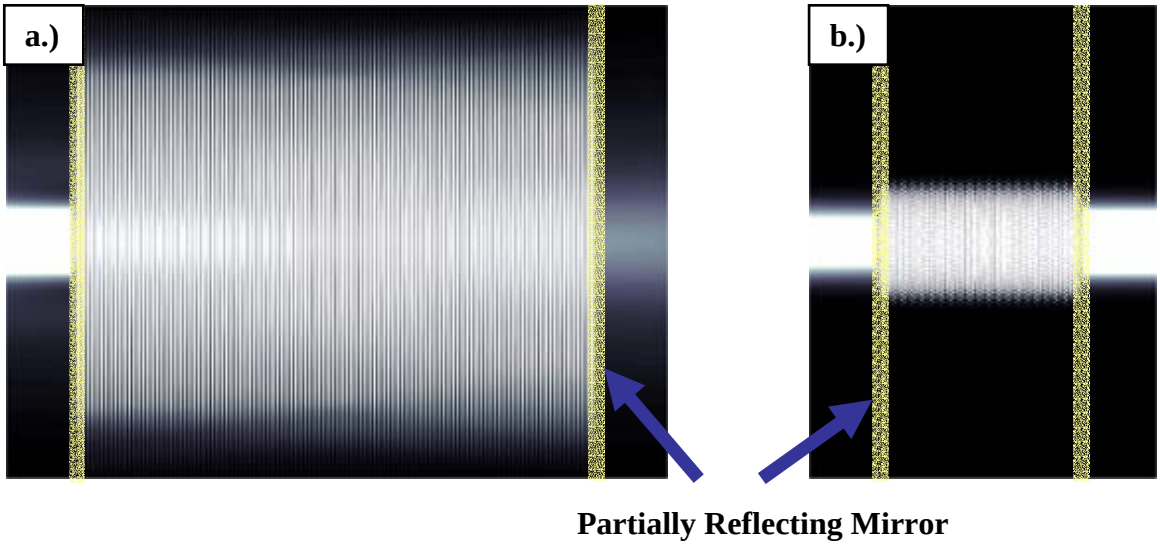

Figure 34. Simulations of the interferometer with photonic crystal mirrors with a.) free space and b.) self-collimating photonic crystal in between the mirrors

dispersive characteristics of the photonic crystal, and integrate within an integrated optical system hold promise for practical applications of miniaturized devices made possible through the self-collimation phenomenon in photonic crystals.

Discussion

This chapter has laid the foundation for understanding the behavior of electromagnetic waves in two-dimensional photonic crystals, with an emphasis on the propagation and application of Gaussian beams in square lattice photonic crystals. An effective media model was developed utilizing anisotropic dielectric constant and magnetic permeability which was shown to successfully model all aspects of a Gaussian beam within the range of interest. Simulations were conducted to discern the range of structures which exhibited self-collimation and their dependence on the index of refraction contrast and the size of the features. The index of refraction and the polarization were shown to have a significant effect on the pillar structures giving this structure the ability to tune its properties across a wide range of frequencies. The hole structures, on the other hand, exhibited only a small dependence on the hold radii for the center wavelength of self-collimation making the structure extremely tolerant to small deviations in fabrication parameters. The tolerance to different errors in fabrication and the routing capabilities of sharp turns and crossing beams were demonstrated for optical interconnect applications. In addition, the ability to miniaturize optical devices without significant beam spreading issues was demonstrated for a Fabry-Perot filter made with self-collimating and band gap photonic crystals.

The development of the model opens the path for exploration and characterization of more phenomena. The model is not restricted to dielectric two dimensional photonic

crystals and can be extended to other effective media, such as periodic and pseudo-periodic structures made of metals. Future work in the simulation and modeling area include the development and verification of compatible effective index models to describe the reflection and transmission properties as well as angle dependent models. Insights gained from the developed models can be used for the exploration of novel applications and new configurations for achieving the desired properties. Simulation provides invaluable feedback in the design of photonic crystal structures to be fabricated, giving the ability to design structures with high tunability and/or high robustness to fabrication errors.

CHAPTER 3

FABRICATION OF 2-D PHOTONIC CRYSTALS

Introduction

Photonic crystals operating in the visible and infrared wavelengths have proved difficult to fabricate until recently with the availability of electron beam lithography (EBL) and other advanced lithography techniques for patterning, such as laser interference lithography[71-73], self-assembled monolayer[74], and x-ray lithography[75]. Through the use of these lithography techniques coupled with fabrication processes from the semiconductor industry, successful fabrication of planar two dimensional photonic crystals have been reported by numerous groups[16,22,34]. In this section, the process development for the fabrication of two dimensional photonic crystals in amorphous silicon on insulator (ASoI) as well as traditional silicon on insulator (SoI) is described. First, the production of an ASoI wafer through growth and deposition of SiO_2 and amorphous Si layers is described, followed by the patterning of photonic crystals utilizing electron beam lithography (EBL). Plasma etching optimization for pattern transfer follows the lithography with a final section on post processing of the patterned device, such as singulation, smoothing, passivation, and production of an air bridge structure. A graphical flow chart of the fabrication process of an ASoI device is outlined in Figure 35. Also, a traveler detailing the process flow, monitoring parameters, and intermediate measurements is given in APPENDIX C.

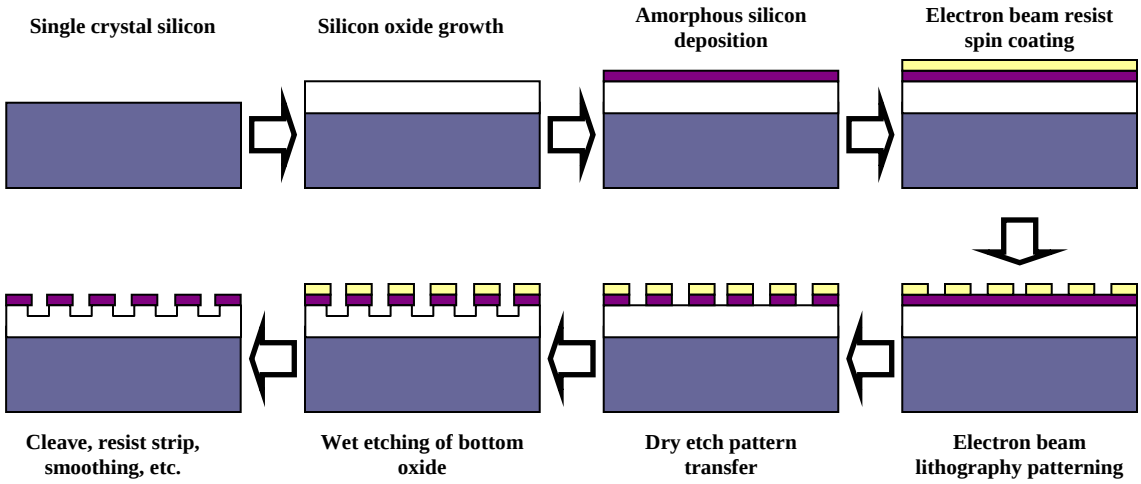

Figure 35. Flow chart of fabrication processes

Substrate: Silicon on Insulator (SoI)

SoI has become the standard material for the fabrication of two dimensional photonic crystals due to the index contrast necessary for confinement in the third dimension. SoI devices offer the confinement necessary for integrated optics in the out of plane dimension by the index contrast between Si and SiO_2 (3.45:1.45), as well as the feasibility for undercutting the bottom oxide layer to form an air bridge structure. Two types of SoI's were utilized in this thesis. The first type was an amorphous silicon layer deposited over the bottom oxide, and the second type was a single crystal silicon layer bonded to the oxide layer. For fabrication of photonic crystal devices, a thick bottom oxide layer of greater than 1 μm is favorable for isolation of the device from leaking into the substrate while a thin top silicon device layer of under 400 nm is required to ensure that the photonic crystal is operating in a single mode region.

Amorphous Silicon on Insulator (ASoI)

Amorphous silicon is an ideal material to use for photonic crystal device fabrication operating at wavelengths in the near infrared. Amorphous silicon has an index of refraction of n = 3.73, which is higher than crystalline silicon with n = 3.45, at a wavelength of 1.55 μm and displays high transparency[76]. In addition, it can be doped and processed to form transistors, and has been widely studied for use in applications such as solar cells and displays[77]. ASoI was fabricated utilizing the thin film deposition equipment available in the cleanroom. A layer of silicon oxide was grown on top of a silicon substrate. Following the formation of the bottom oxide layer, a thin layer of amorphous silicon was grown on top of the oxide.

Two methods of forming the bottom oxide layer in the aSoI were investigated. The first method was to utilize the plasma enhanced chemical vapor deposition (PECVD) method. The equipment used for this process was the Unaxis 78324 PECVD. A schematic of this equipment is given in Figure 36. The equipment consists of parallel plates where the RF plasma at 13.56 MHz is produced. The top plate, called the showerhead, delivers the source gas through small holes distributed around the plate for uniform deposition. The sample is located on the bottom plate and is heated to assist in the chemical reaction and the formation of a dense film. The recipe used for the SiO_2 deposition consisted of 400 sccm SiH_4/He mixture and 900 sccm N_2O with an RF power of 25 W, 900 mTorr process pressure, and a 300°C platen temperature. The deposition rate for this recipe was approximately 60 nm/min and stays relatively constant for depositions as thick as 5 μm.

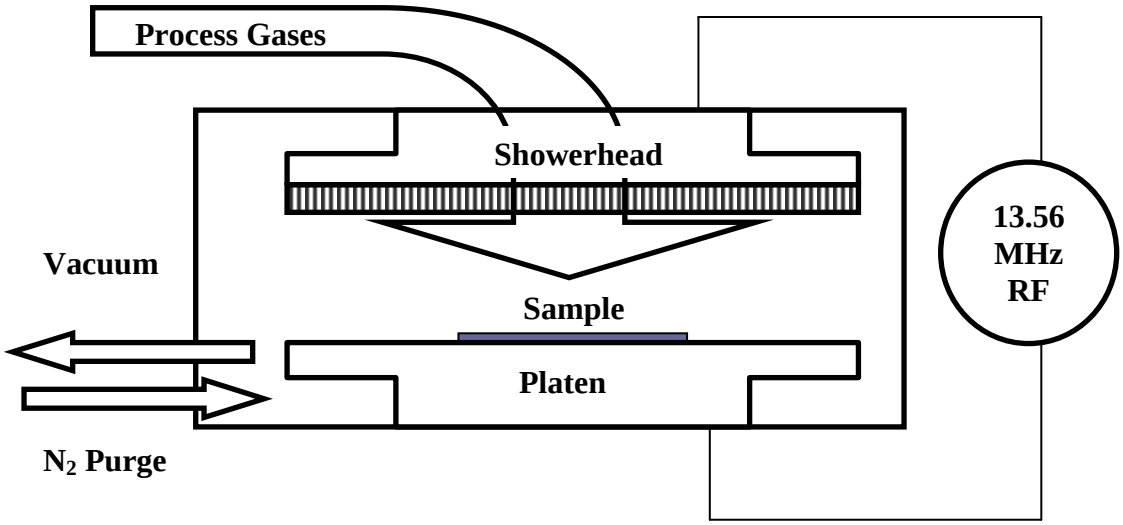

Figure 36. Schematic of a PECVD system.

The second method used for the formation of the bottom oxide layer was by wet oxidation of the silicon substrate in a furnace. The Lindberg tube furnace was used with a bubbler to feed in H_2O vapor along with oxygen for the surface oxidation. The Deal-Grove model for oxidation gives an accurate prediction for the thickness of a grown oxide layer. The oxide growth occurs at the boundary of the already grown oxide and the silicon layer. Therefore, the oxygen must diffuse from the surrounding atmosphere through the oxide to the interface between the oxide and the silicon. The model equates the flux of oxygen to the interface from the atmosphere (J_1), with the diffusion of oxygen through the oxide layer (J_2), and the reaction rate of silicon with the oxygen at the interface (J_3). By adding another equation relating the concentration of oxygen on the surface of the oxide to the partial pressure of oxygen in the gas through Henry's law, the set of equations can be solved. The final solution is given by:

$$t_{ox}^2 + At_{ox} = B(t + \tau)$$

where

$$A = 2D\left(\frac{1}{k_s} + \frac{1}{h_g}\right)$$
$$B = \frac{2DHP_g}{N_1} \qquad \textbf{Equation 26}$$
$$\tau = \frac{t_0^2 + At_0}{B}$$

and D is the diffusion constant of oxygen or water through the oxide, k_s is the chemical rate constant for the reaction to form oxide, h_g is the mass transport coefficient describing the flux of oxygen from the atmosphere, H is the Henry's gas constant, P_g is the partial pressure of the oxygen containing species in the atmosphere, and N_1 is half the number density of oxygen atoms in SiO_2 ($2.2x10^{22}cm^{-3}$)[78]. Experimentally observed A and B constants agree well with theoretical values. Table 1 gives these constants for dry and wet oxidations. The growth rate of the wet oxidation in the Lindberg furnace was observed to be much slower than the calculated growth rates. This is attributed to the partial pressure of H_2O being much lower than the 640 Torr partial pressure used in the calculations as the feed from the H_2O bubbler was kept well below the boiling point of water to avoid overheating and cracking of the glass containers. To achieve an oxide

Table 1. Table of Deal-Grove model constants for oxidation of silicon

	Dry (O_2)		Wet (H_2O 640Torr)	
Temperature (°C)	A (μm)	B (μm^2/hr)	A (μm)	B (μm^2/hr)
1000	0.165	0.0117	0.226	0.287
1100	0.090	0.027	0.11	0.510
1200	0.040	0.045	0.05	0.720

thickness of 1.5 μm a 9 hour wet oxidation was necessary.

The roughness of the two oxide films produced was measured using an atomic force microscope (AFM). Figure 37 shows a 3D picture of the two surfaces. The RMS roughness was 4.044 nm for the oxide deposited by the PECVD, while the roughness for the wet oxidation film was only 0.051 nm, almost two orders of magnitude smoother. The thermal oxidation produces a higher quality oxide compared to PECVD and can be considered nearly atomically smooth as expected from the oxidation of an atomically smooth, single crystal silicon wafer. The smoothness of the oxide layer is a very important factor in reducing the optical loss of the photonic crystal devices fabricated.

The amorphous silicon layer was also deposited by the PECVD using the Unaxis 78324 PECVD system. The recipe for deposition consisted of an 800 sccm SiH_4/He mixture with an RF power of 50 W, 550 mTorr process pressure, 150°C platen temperature, and 30 minutes deposition time. Initially, a high platen temperature of 300°C was used, but films grown at a high temperature exhibited high stress due to the difference in thermal expansion coefficient between silicon (2.6 ppm/°C) and the silicon

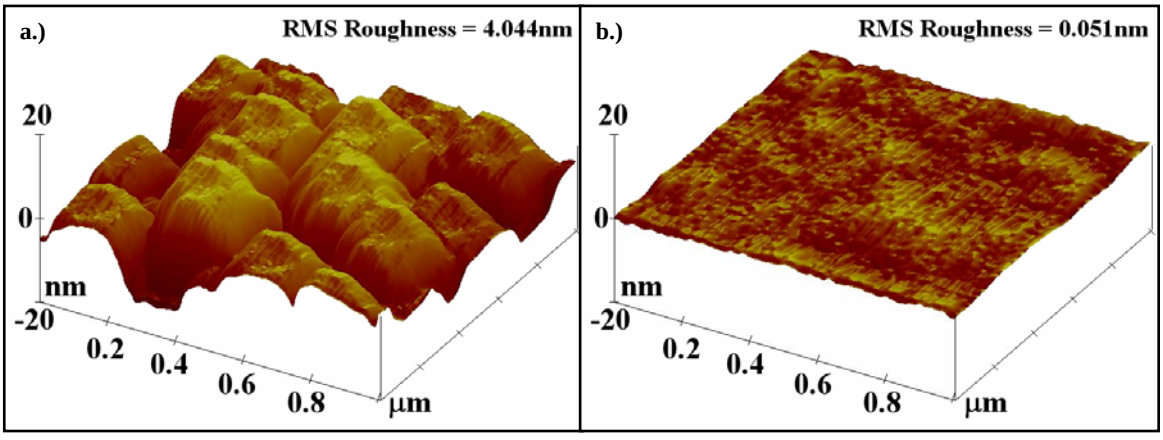

Figure 37. 3D images of AFM scans for silicon oxide. a.) Deposited by PECVD and b.) Grown using wet oxidation

oxide (0.5 ppm/°C) causing them to crack. For these films, the platen had to be cooled slowly to 100°C before removing the sample or else the films started to crack. A 30 minute deposition, resulting in ~200 nm layer of amorphous silicon, was chosen since a larger thickness also induced large stresses inside of the film. Figure 38 shows cracking in the film due to thermal stress on wafers resulting from high deposition temperature, too thick of a deposition, and rapid thermal gradients due to rapid cooling of the sample after deposition. Substrates with cracks and defects also nucleated cracks which with time spread across the whole film. An AFM scan of the amorphous silicon deposition, shown in Figure 39, on the previously measured PECVD oxide and the wet oxidation oxide shows the dramatic difference obtained in the quality of the amorphous silicon layer due to the underlying substrate. The RMS roughness for the film deposited on top of the PECVD oxide was 3.904 nm showing little difference from the oxide. However, the morphology is much finer showing that the amorphous silicon deposition resulted in much smaller aggregate sizes as expected in a low temperature deposition where the adsorbed atoms do not have as much energy to diffuse and anneal to larger pieces. The amorphous silicon deposited on the oxide grown by wet oxidation showed a RMS roughness of only 0.579 nm. The low temperature amorphous silicon layer was tested to see if the film can withstand undercutting of the bottom oxide layer by etching a piece of the wafer in a buffered oxide etch (~85 nm/min etch rate) for 10 minutes. An SEM angled view and cross section shown in Figure 40 reveal that the stress in the film is low enough to form a free standing film.

By utilizing wet oxidation followed by a low temperature PECVD amorphous silicon deposition, a high quality ASoI wafer was fabricated. The fabricated ASoI's

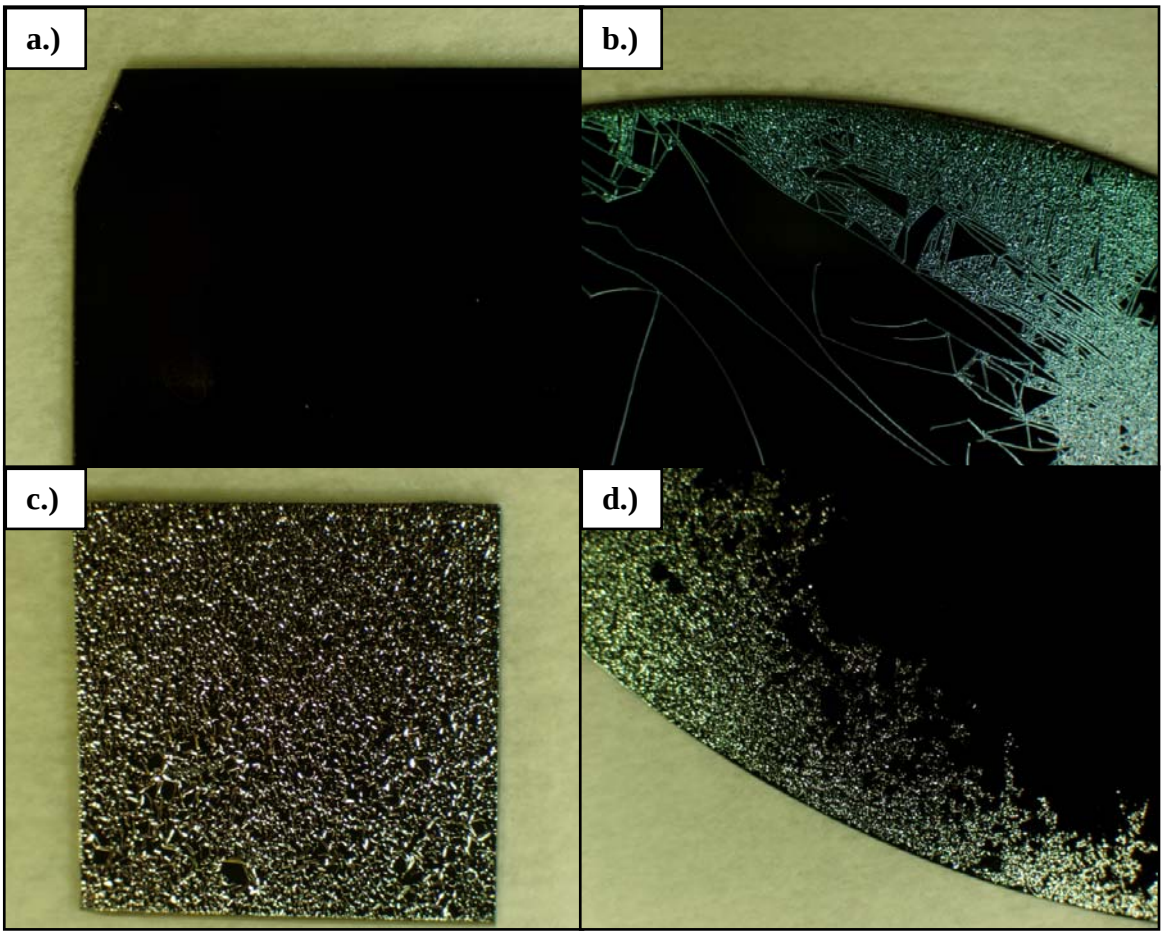

Figure 38. Cracking of amorphous silicon films grown on thermally oxidized wafers. The depositions were performed at: a.) 150°C for 30 min. b.) 300°C for 30 min and left at room temperature for 1 week. c.) 150°C for 45 min. d.) 300°C for 30 min and removed from the platen immediately.

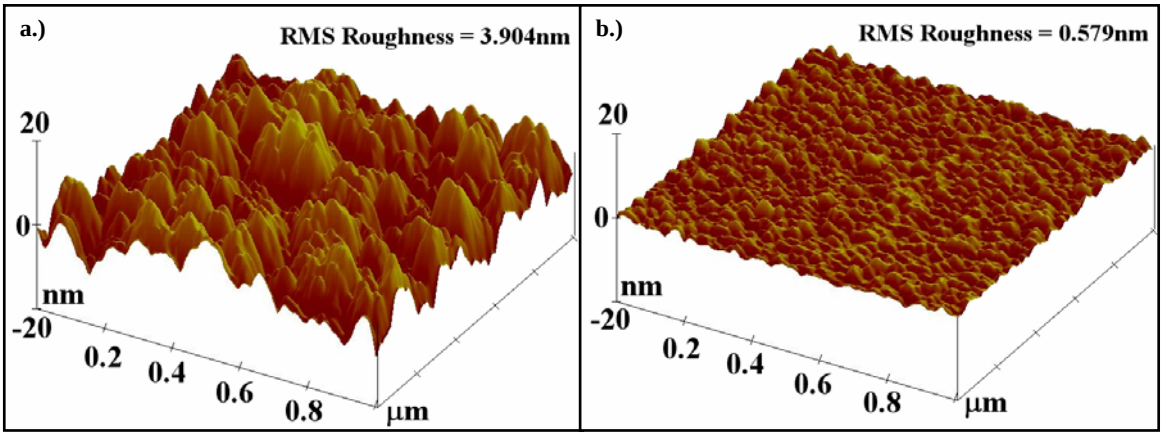

Figure 39. 3D images of AFM scans for amorphous silicon deposited over a.) PECVD oxide and b.) wet oxidation grown oxide.

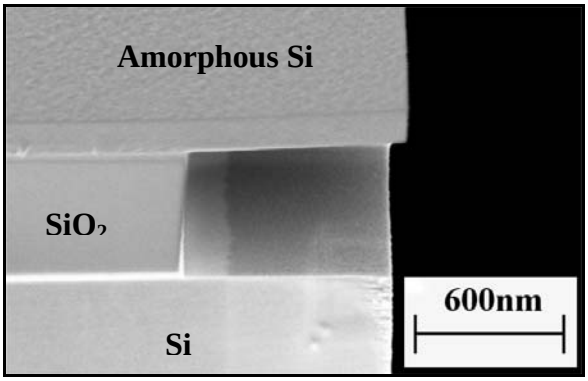

Figure 40. Amorphous silicon deposited at 150°C for 30min and etched in a buffered oxide etch for 10min showing that it can form a free standing film.

ranged from 1~1.5 μm thickness of the bottom oxide with approximately 200 nm of an amorphous silicon device layer on top. The film was thermally and mechanically stable and was possible to undercut without pealing or cracking.

Single Crystal SoI

Single crystal SoI wafers were purchased from industry vendors. The fabrication method for the SoI utilizes wet oxidation to grow the bottom oxide and then various proprietary methods for bonding thin films of silicon onto the oxide. For thick films, epitaxial single crystal silicon is grown on top of the bonded single crystal silicon. Wafer

bonding is performed using rapid thermal processing equipment or plasma assisted bonding methods. The bonded wafer, usually 100's of microns thick, is cut utilizing methods such as the smartcut™ and nanocleave™ methods. Both methods employ ion implantation of dopants, hyrdrogen in the case of the smartcut™ method, into a controlled thickness of the wafer to make the wafer more brittle. Then the wafer is cleaved utilizing either a thermally assisted or a gas pressure controlled cleaving of the top wafer. Due to limitations on the mechanical stability of the wafer and the depth achievable in ion implantation, the bonded layer is usually between 150 nm and 250 nm thick. To achieve thicker layers, an epitaxial growth of silicon is performed utilizing methods such as low pressure CVD. The purchased SoI wafer properties were 3 μm thickness of the bottom oxide with a 250 nm thick single crystal <100> orientation silicon device layer.

Patterning: Electron Beam Lithography (EBL)

Photonic crystals operating in the infrared wavelengths require uniform feature sizes on the order of hundreds of nanometers. To draw reproducible, uniform periodic patterns in this size range, a resolution of less than 10 nm is necessary. Electron beam lithography is ideal for patterning small area devices since an electron beam can be focused to a spot size of under 5 nm diameter and can be scanned using magnetic lenses with precision of a nanometer or less. For this research, the JEOL JBX-9300FS EBL system was utilized. This system features a variable spot size ranging from 4 nm to 200 nm with vector scanning, and a step and repeat stage. The addressing resolution is 1 nm. The principle of operation for the EBL system and its basic parts are described. Then the

results of test runs to optimize the exposure to achieve the desired pattern are described. Finally a short description of the patterns written is given.

Principle of Operation

The EBL system is very similar to a scanning electron microscope (SEM), where an electron beam is focused to a spot onto the substrate and scanned over the desired field of view. The major differences between an SEM and an EBL system is that in an SEM, the emphasis is on capturing signals emitted from the sample, due to the incident electron beam, for imaging and analysis, while an EBL system is focused on controllably applying the desired dose of electrons in a localized pattern on the substrate. Therefore, the SEM includes many configurations of detectors, such as the secondary electron detector, backscattered electron detector, and in-lens secondary electron detector for imaging, electron backscattered diffraction (EBSD) system for crystallographic information, and energy dispersive spectroscopy (EDS) detector for compositional analysis. On the other hand, the EBL system includes a highly accurate positional control stage using laser interferometry to measure the position of the stage and sample, a Faraday cup with a picoampere current detector, high speed blanking system for blocking the electron beam during movement, sophisticated software and routines for automatically correcting for focus, stigmatism, and a computer interface to feed data from a CAD file into the instrument. The JEOL JBX-9300FS also operates all components digitally including the focus, scanning, and stigmatism alignment[79].

Figure 41 shows a schematic of the major components of the EBL system and the sample holder cassette. The electron gun and the condenser lenses comprising the top

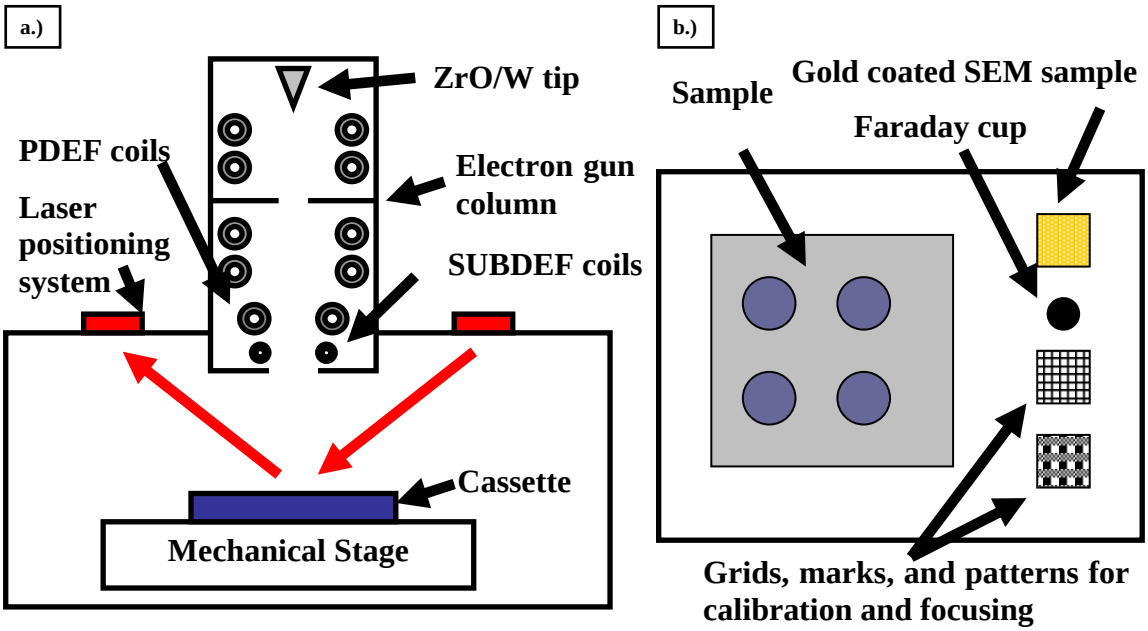

Figure 41. Schematic of the major components of a.) the JEOL JBX-9300FS EBL system and b.) the sample holder cassette.beam

column generate the electron beam and are identical to an SEM and are not described in this thesis. The system features two scanning deflectors, the position deflectors (PDEF) and the subfield deflectors (SUBDEF). The position deflectors provide coarse deflection of the beam over a field of view of up to 500 μm by 500 μm, while the subfield deflectors scan the beam over a maximum of a 4 μm by 4 μm area with an addressing resolution of 1 nm. For any pattern larger than 500 μm by 500 μm, the stage is mechanically moved and then the laser positioning system is utilized to measure the exact position of the stage. A small deviation in the position of the stage from the intended position is compensated by adjusting the PDEF coils. The cassette includes the sample holder with different configurations to hold 3", 4", 6", and 8" wafers, 4" and 5" masks, and a "pieces holder" to hold smaller samples. In addition, a faraday cup for measuring the current is

integrated onto the cassette along with knife edges, grids, and focusing areas for the calibration.

The CAD file for designing the patterns written on the EBL system is created using AutoCAD 2004. The file is converted from a DXF format into a GDSII format, which is converted to a pattern file on the EBL system. Once the pattern file is created, two more files, the jobdeck file (JDF) and the scheduler file (SDF), is needed to define the other parameters necessary for writing the pattern including the system settings, electron beam dosage, calibration sequence, arrangement of the pattern, the layers to be written, and the order of writing the patterns. Examples of JDF and SDF files are given in APPENDIX D and APPENDIX E. Important parameters in these files include the shot pitch and resist base dose, specified in the SDF file under the commands SHOT and RESIST. The shot pitch is defined in nanometers and corresponds to the spacing between two adjacent points drawn. The base dose is in units of $\mu C/cm^2$ and corresponds to the dosage applied to each point on the CAD file. The EBL system has a minimum dwell time that it can keep the beam stationary at a spot, determined by the beam blanking speed as well as the scanning speed of the beam. Therefore, the shot pitch can not be so small that the minimum time spent at a point exceeds the dosage allocation of the area calculated for that point. The other commands include instructions to read in the settings for the system as well as offsets to place each pattern at the correct location on the wafer. The important parameters in the JDF file are the layout of the pattern, the current setting of the system, and the shot modulation to vary the dosage. The layout of the pattern is determined by the ARRAY command in the first part of the file. Various patterns can be arranged utilizing the ARRAY and ASSIGN commands as well as

repeating a desired pattern in a regular Cartesian grid. The second section of the file includes the STDCUR command which signifies the current of the beam. This value is necessary to calculate the shot pitch along with the parameters in the SDF file. The common settings for the system are 10nA, 1nA, and 100pA. A lower current produces a tighter focus resulting in higher resolution, but requires a longer time to write. For the feature sizes necessary for a photonic crystal, the 1nA setting was found to be the best compromise between reasonable speed and acceptable resolution. The MODULAT command in the JDF file sets the values for the shot modulation option. This option allows different layers in the CAD file to have different dosages. Since the minimum shot pitch value is determined by the smallest dosage, the dosage can only be increased from the base value. The values following the MODULAT command assigns each numbered layer with a dose which is a percentage increase from the base dose. Thus, a base dose of $200\mu C/cm^2$ and a shot modulation of 50 would result in a dose of $300\mu C/cm^2$ as that is 50% greater than the base dose. In addition to these setting, a calibration sequence determined by the PATH command in the JDF file is executed during each run. A graphical user interface is utilized to load/unload the sample holder, run calibrations, and start the writing process.

The mechanism for the pattern transfer lies in the interaction of an electron beam with the resist layer as well as with the substrate. The primary resist investigated in this study was the ZEP-520A, a proprietary block copolymer resist supplied by Zeon Chemicals. The electron beam patterns the ZEP resist by chain scission, a process by which the electron beam breaks apart the chains of the polymer allowing it to dissolve away in a developer solution. ZEP is a positive tone resist since the portions written by

the electron beam are dissolved away. This resist was chosen over other positive tone electron beam resists, such as a polymethylmethacrylate (PMMA) resist, due to the ZEP-520A having a higher contrast and higher etch resistance. The contrast for a resist is given by:

$$\gamma = \frac{1}{\log_{10}\left(D_{100} / D_0\right)} \qquad \textbf{Equation 27}$$

where γ is the contrast, D_{100} is the dose necessary to develop 100% of the resist, and D_0 is the maximum dose where no resist is developed[78]. The ZEP resist is a block copolymer consisting of chains with higher resistance to chemical attacks compared to PMMA, which allows it to stay intact longer in a plasma etch allowing for a deeper etch with the same thickness of the resist. A negative tone resist consisting of a film of hydrogen silsesquioxane (HSQ) supplied by Dow Corning was also investigated. The mechanism for patterning the HSQ is the reaction of the resist to form SiO_2-like film by interaction with an energetic electron beam. The unreacted HSQ dissolves in a tetramethyl ammonium hydroxide (TMAH) solution leaving behind the portion reacted by exposure to the electron beam. The positive tone resists are well suited for writing holes while the same pattern written in a negative tone resist results in pillars. However, due to a higher dose required for HSQ and rougher sidewalls resulting from the reaction of HSQ with the electron beam forming a granular solid, the ZEP-520A was the primary resist investigated in this thesis.

Optimization

Several parameters must be optimized to successfully transfer the pattern in the CAD file to the electron beam resist. The parameters to optimize include the thickness of the resist, the exposure dose, design parameters of the pattern, and the writing time.

One of the most important parameters to optimize in the lithography process is the thickness of the resist. In general, the aspect ratio (height/width) which can be obtained in the resist before the resist topples or slumps is a fixed value. Therefore, to achieve smaller features, a thinner resist must be used. However, to transfer the pattern down into the underlying layer, a thicker resist layer is desired since the etching process etches both the resist and the underlying film. For the ZEP resist, a thickness of around 400 nm was found to be adequate for both the writing and etching processes. The resist was coated using a spin coating technique. Figure 42 shows the curve of resist thickness vs. spin speed as provided by the vendor. A spin speed of 3000RPM produces the desired thickness of the resist. However, it was experimentally found that the resist solution has difficulty wetting the surface, which can result in a resist layer that is significantly thinner than those predicted. In addition, when acetone, a common cleaning solvent, contacts the resist solution, a white solid residue formed. The wafer surface must be cleaned and kept free from solvent residue to ensure that the desired thickness and quality of the resist film is obtained. A 180°C post bake for 90s was performed after spin coating the resist to drive off the excess solvent and to cure the resist.

After coating the resist, the exposure dose was optimized to produce uniform and consistent patterns. The exposure by the electron beam is not limited to the area where the beam actually strikes the sample. The electron beam will have a finite probability of

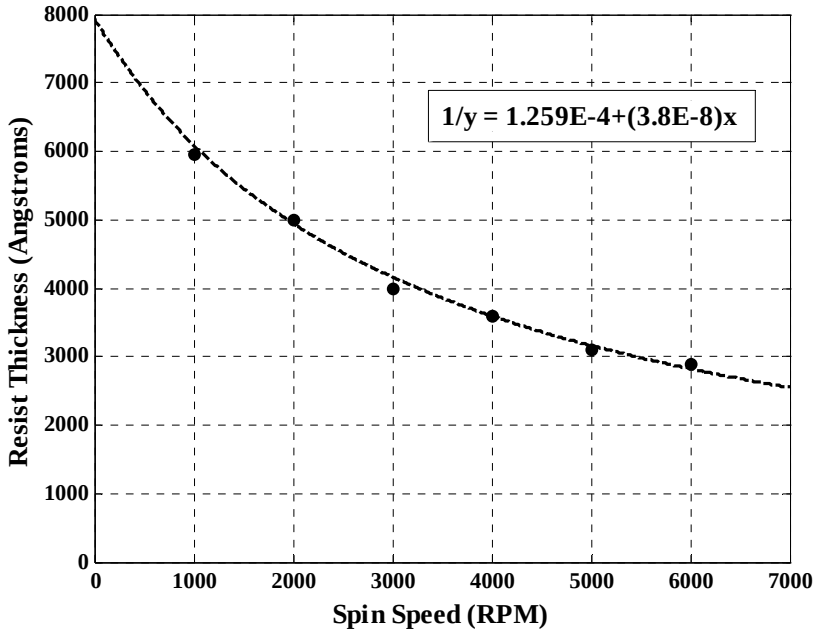

Figure 42. Spin speed vs. thickness of the resulting resist thickness for ZEP-520A electron beam resist

striking a molecule in the resist as it passes through it in the forward direction. After passing through the resist, the electrons can scatter backwards from the sample and again pass through the resist. This forward scattering and back scattering produces a complex dose profile which can be corrected by using proximity effect calculations. The forward scattering probability increases as the thickness of the resist increases, thus the dose required for a thicker resist film is generally smaller than for a thin resist where the majority of the electron beam passes through the sample without ever hitting a resist molecule. The forward scattering tends to increase the spot size of the beam as more scattering events occur, thus forming a slightly reentrant profile in a thick resist. The back scattered dose depends on the energy of the electrons. For the 100kV accelerating voltage utilized in the EBL system, points as far away as 50 μm can affect the features with the effect decreasing in a Gaussian-like manner from the center of the beam. Also,

the photonic crystals fabricated consist of circular patterns. Due to the addressing of the system in Cartesian coordinates, which results in dividing a circle up into triangles, trapezoids, and rectangles when being written, the best results for circles are obtained by writing a smaller circle and giving a high dose so that the features blur to form a smoother, less faceted edge. The effect of these factors are evident in the measured hole sizes in a square lattice photonic crystal, written with a r/a value of 0.2 for diagonal lengths equal to 400 nm, 500 nm, and 600 nm, comparing the size of the circle at the center of the pattern to those at the edge of the pattern where there was a solid block written. The circle sizes are approximately 110 nm, 140 nm, and 170 nm respectively. Figure 43 shows the trend of the circle sizes for this pattern. The base dose for the ZEP-520 A was 200 $\mu C/cm^2$ to expose large areas. The circles are given a larger dose of 600 and 1000 $\mu C/cm^2$. The circles near the edge where there was a large backscattered dose coming from the block outside of the edge shows a much larger circle than in the center. This can be attributed to the fill fraction of holes in the pattern being only 12.6%, so even a dose of 1000 $\mu C/cm^2$ has a smaller average dose per area (126 $\mu C/cm^2$) compared to the base dose of 200 $\mu C/cm^2$ used in the adjacent block. The patterns near the edge are strongly governed by the backscattered dose resulting in all three patterns showing a similar increase in diameter. The smallest circles show the largest percentage increase in circle size with an increase in the backscattered dose from the adjacent block. This can be attributed to the area affected by the strong forward scattering being a larger percentage of the beam diameter for the smallest circle since the forward scattering range is determined by the size and energy of the electron beam spot. For the regions in the center, this relationship did not hold as well with the largest circle showing a larger

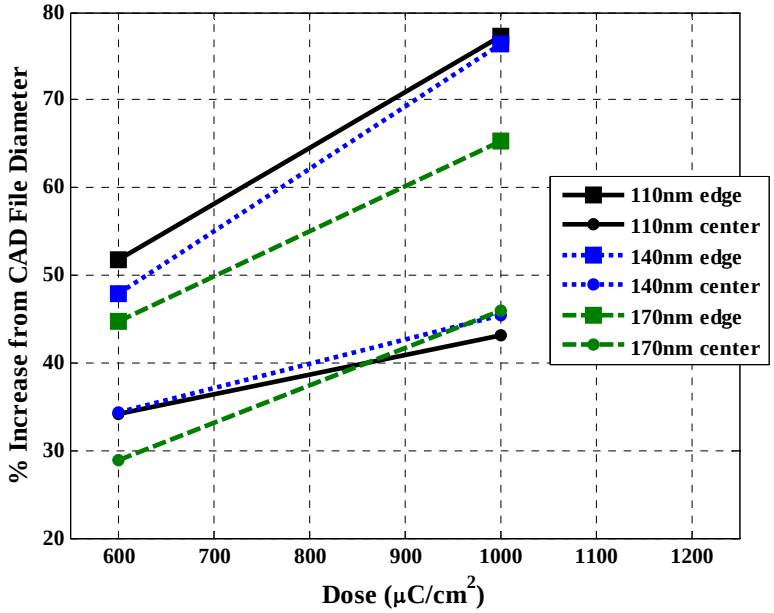

Figure 43. Increase in the diameter of circles written in the EBL system with respect to the dose and the location within the pattern

dependence on the dosage. There is a trend that the larger circles have a larger dependence on the dose, but the relationship is not clear. The slope for the 170 nm circles is similar near the edge and in the center, suggesting that the region is in an area where the increase in the backscattered dose has a linear effect in increasing the size. The two smaller holes show a lower slope in the center indicating that these sizes are still experiencing a complex dependence on the dose. Therefore, the size range of features necessary for the photonic crystal is in a region where the effect of the dose on the final size follows a complex function and is a very difficult parameter to optimize. The approach taken to mitigate this factor is to create multiple samples with a range of doses to ensure that there is a sample with the desired size.

In conjunction with adjusting the dose of the pattern using shot modulation, the design of the pattern must also be optimized. It is necessary to design the outer edges and

the borders of the pattern to adjust for the proximity effect. Another major issue with the design of the pattern is the field size. As mentioned previously, the system writes the pattern with a maximum field size of 500 μm by 500 μm. Larger field sizes will require mechanical movement and realignment of the stage. This procedure is only guaranteed to ±25 nm accuracy, even though accuracy around ±10 nm is commonly achieved. When critical features, such as very narrow lines or waveguides are cut in this way, the error when stitching the fields, called the stitching error, can make a device inoperable. Also, the stitching error is magnified when proper height calibration is not performed on the sample. The HEIMAP calibration routine, which measures the average height of the sample using the laser positioning system and creates a matrix of deviations from the average height, must be run on the sample while ensuring the area covers the region which is to be written. An example of a stitching error, where proper height measurement was not taken into account, is given in Figure 44. In addition to running HEIMAP, the CAD file design was modified and split to multiple CAD files to have control over the position of the field boundaries. In this manner, the location of field boundaries can be controlled to be at locations where a 10-25 nm inaccuracy will not cause the device to become totally inoperable.

The final parameter that needs to be optimized is the writing time. Even though it is important to produce the best quality possible, it is also important to realize that there are multiple steps after the lithography, which necessitates the need to make multiple samples to optimize further steps in the process, along with allowing for the chance of failure in the subsequent steps. The writing time can be divided into several components: the time necessary to expose the areas to be written, the time necessary to move the stage

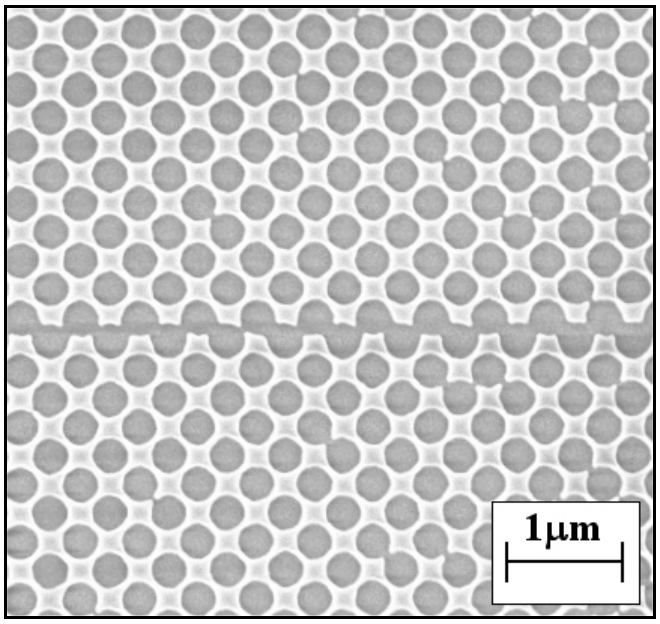

Figure 44. Example of stitching error caused by improper calibration of the height of the sample

between each field, the time necessary to run cyclic calibration, and the time necessary to move between the locations to be written. The theoretical exposure time can be calculated using the equation:

$$t_{exposure} = \frac{Area \times Dose}{Current} \qquad \textbf{Equation 28}$$

The exposure time for a 1 mm^2 square pattern written at 200 $\mu C/cm^2$ dose and 1nA current is 33 minutes and 20 seconds. For photonic crystal devices where the area written is often much less than 1 mm^2, the exposure time is usually less than 30 minutes per device including the long input and output waveguides. However, for measuring the band structure of the photonic crystal using transmission and reflection measurements using conventional spectrometers and halogen lamps, an area ranging from 1 mm^2 to 4 mm^2 must be patterned, resulting in exposure time a theoretical exposure time in hours. By increasing the current, the exposure time can be reduced drastically. However, the

other factors are relatively unaffected by the electron beam current. To determine the magnitude of each component, several test patterns were written. The test patterns included vertical, horizontal, and diagonal lines of width 1 μm and length of 500 μm and squares and circles in a square lattice with a fill fraction of 25% with spacings of 2 μm and 1 μm respectively for the large and small patterns. The calibration time and the stage movement time was estimated using a stop watch while monitoring the progress of the writing and were given values of 125 seconds for each calibration cycle and 2 seconds for each stage movement between fields, and the test patterns were exposed using a 1nA current setting. As shown in Figure 45, the processing time for the lines had almost no overhead from beam movement or stage movement giving a value very close to the theoretical exposure value after subtracting the calibration time. The squares and circles showed a different trend where the time to move the stage and the beam were of significant value where they can not be neglected. For the squares, the size of the squares

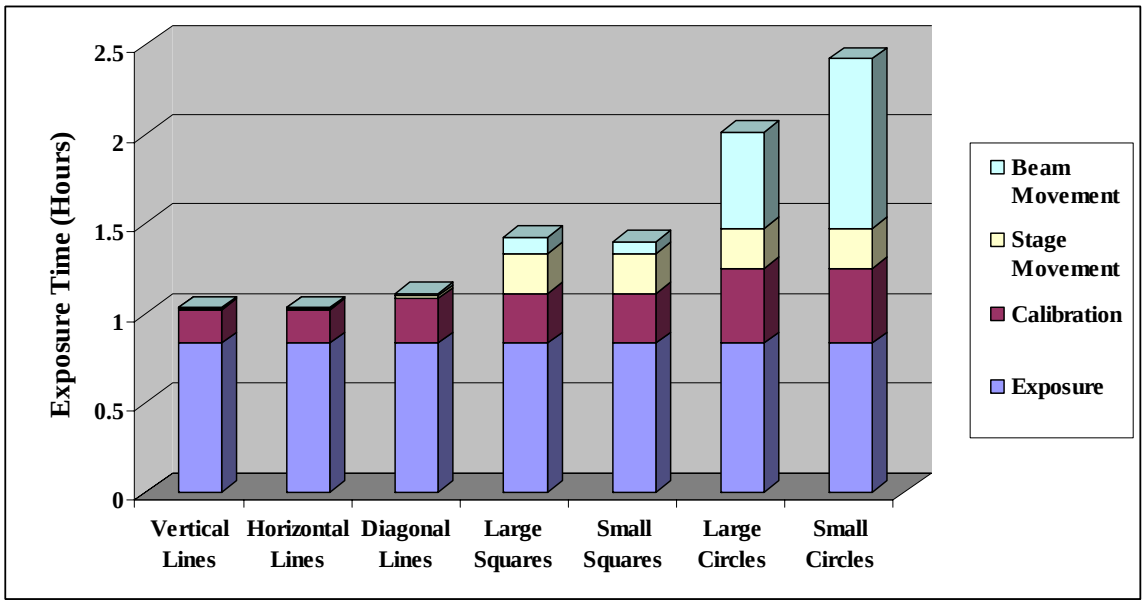

Figure 45. EBL writing time normalized to 1 mm^2 exposure area for various test patterns

had a negligible effect on the writing time. However, for the circles, the smaller circles required a significantly longer beam movement time which even surpassed the theoretical exposure time. The stage movement time was greater for these patterns due to a smaller field being written. Due to the limitation of the CAD file size, both within AutoCAD and the EBL system program, smaller fields must be written and repeated, resulting in a much longer stage movement time. However, this component would also be negligible in actual pattern writing as the field size would be much greater than the value used for the test patterns. With this result, the current optimization can be put into proper perspective. By increasing the current to 10nA, the exposure time can be decreased by a factor of 10. However, due to the photonic crystal dimension being closest to the small circles in the test patterns, the writing time is only expected to decrease by a factor of ~2. On the other hand, by decreasing the current to 100pA, the exposure time would increase by a factor of 10. In this case, the exposure time would dominate the total writing time and the exposure is expected to take ~5 times longer than at 1nA. For a current setting of 1nA, the beam movement and exposure time are within the same order of magnitude and is the best compromise between resolution and writing time for EBL exposure of photonic crystals.

Patterns Generated

Once an optimal condition for the EBL system was determined, three sets of patterns were generated for further processing: a test pattern consisting of a small number of lines and circles to develop the etching process, a large 1 mm by 1 mm square of a square lattice photonic crystal for band structure measurement using reflectivity, and a device for verifying the self collimation effect in the photonic crystal. The test pattern

consisted of sets of 5 lines with lengths of 1 mm and widths ranging from 150 nm to 1 μm and circles of the same size arranged in a line of lengths 1 mm with 5~15 periods in width. These test patterns were created on silicon wafers and oxidized silicon wafers to develop the etching process. The device pattern was written on the ASoI and SoI substrates. Figure 46 shows an optical scope image of the device pattern on an ASoI substrate. The photonic crystal is in the small square brackets in the middle of the image with the single input waveguide on the bottom and multiple output waveguides on top. The device design will be discussed in more detail in the measurement chapter.

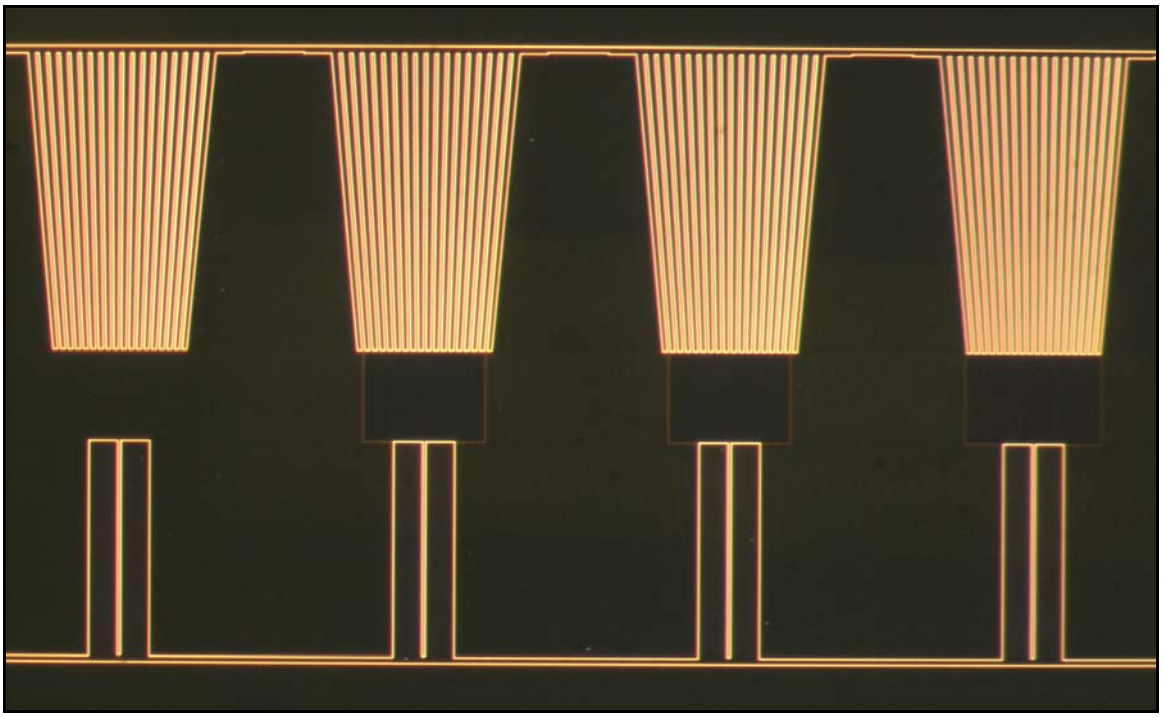

Figure 46. Optical image of the device pattern written ZEP-520A resist on an ASoI

Pattern Transfer: Plasma Etching

Once the pattern was written into the resist using the EBL system, it was then transferred to the underlying silicon layer. Dry etching was chosen as the pattern transfer method due to the availability of knowledge from the semiconductor and MEMS

technologies on etching silicon. The important factors in the pattern transfer is the anisotropy and smoothness of the sidewall as even a small taper or roughness along the sidewall can cause significant loss and mode coupling in the final device. The inductively coupled plasma (ICP) etching technique was selected for the etching method due to the added level of plasma control it has over the reactive ion etching (RIE) as well as the availability of the appropriate process gases on the Plasmatherm ICP in the cleanroom facility used.

Principle of Operation

Plasma etching has numerous advantages over wet etching such as greater control of the length of the etch through the ease of stopping the plasma, less sensitivity to the ambient through control over the environment in a vacuum chamber, and higher anisotropies possible by controlling the plasma characteristics.

The basic configuration of an ICP plasma etching machine is shown in Figure 47. The configuration is similar to the PECVD described previously except that an additional set of RF coils encircling the chamber as well as the top electrode consisting of the whole chamber walls instead of a showerhead. The main differences between the PECVD and the plasma etching are the process gases and the density of the plasma. PECVD utilizes gases like SiH_4 as the objective is to deposit solids, while plasma etching utilizes gases with high halogen component, usually fluorine or chlorine, to form volatile compounds with the material to be etched which can then be pumped away. In PECVD the plasma acts to ionize the source gases to form more reactive species and to give the adsorbed species sufficient energy and surface mobility for deposition. In plasma etching, the

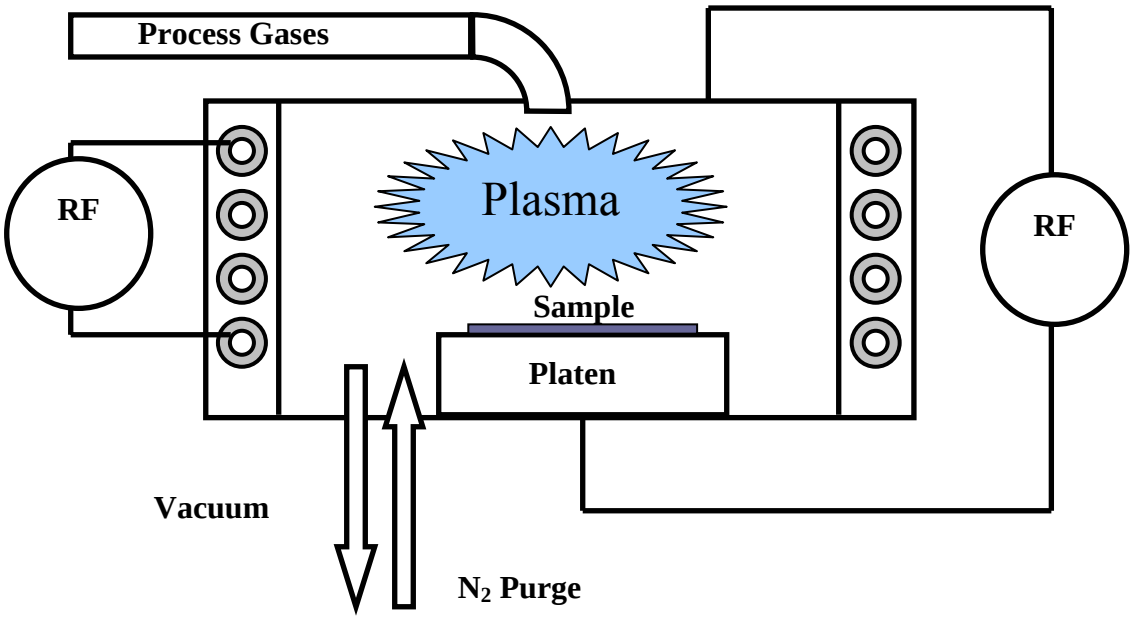

Figure 47. Basic configuration of an ICP plasma etching machine

plasma energy not only breaks up the process gases into reactive species, but also accelerates them to the substrate to give enough ion bombardment energy to break chemical bonds on the surface and to directly sputter the substrate. Therefore, the RF power and the voltage difference between the plasma and the electrodes are much higher in plasma etching. Unlike the more symmetric parallel plate setup used in the PECVD, the plasma etchers utilize the whole chamber wall for the top electrode. This configuration allows for a higher voltage difference between the plasma and the platen following the equation:

$$\frac{V_1}{V_2} \approx \left(\frac{A_2}{A_1}\right)^4 \qquad \textbf{Equation 29}$$

where V_1 is the voltage difference between the plasma and the platen, V_2 is the voltage difference between the plasma and the top electrode, and A_1 and A_2 are the areas of the two electrodes[78]. The DC bias (V_1-V_2) is a parameter which is recorded to ensure consistency of the process. By having a high ratio of areas, the plasma etcher can achieve the high voltage difference necessary to accelerate the ions with sufficient energy onto the substrate. The RIE consists of only one set of RF power, thus both the density of the plasma and the bias across the plasma is controlled by only one parameter. The ICP has an additional coil surrounding the chamber with RF power. This alternating RF signal creates a fluctuating magnetic field which causes the free electrons in the plasma to spiral as they move in the chamber. The spiraling increases the length of path traveled by the electron thus increasing the chance of collision with gaseous species in the chamber resulting in a high density plasma. In this manner, the ICP controls the density of the plasma and the DC bias separately by having two RF power sources available.

A wide range of plasma processes are available which are usually subdivided based on the pressure range in which they operate. The pressure determines the mean free path of the gaseous species, where the mean free path λ is given by:

$$\lambda = \frac{kT}{\sqrt{2}\pi d^2 P} \qquad \textbf{Equation 30}$$

where k is the Boltzmann's constant, T is the temperature, d is the hard sphere model diameter of the gaseous species, and P is the pressure[78]. A high pressure plasma is formed when the mean free path is much smaller than the chamber size. In this regime,

there are multiple collisions within the plasma causing in the plasma to become confined within the areas with the large electric field. The number of reactive species is large and the etching is primarily of a chemical nature. At lower pressures, when the mean free path is within an order of magnitude of the chamber size, the plasma has good contact with the chamber walls and fewer collisions occur within the plasma. This setup is used for the RIE and the ICP as good contact between the chamber walls and the plasma is necessary to increase the effective area of the top electrode. Also, due to a small number of collisions the ion velocity is higher and is nearly vertical towards the sample. Due to this vertical flow of ions, the RIE and ICP can produce highly anisotropic profiles compared to a high pressure plasma where the etch profile is more isotropic.

For fabrication of photonic crystal, the only material that needs to be etched is silicon. The two gaseous species most commonly used to etch silicon and silicon containing compounds are fluorine and chlorine. Both fluorine and chlorine produce volatile compounds with silicon, such as SiF_2, SiF_4, and $SiCl_4$. The most common source for fluorine in an ICP is CF_4. Etching of silicon utilizing CF_4 consists of breaking the C-F bonds in CF_4 and the Si-Si bonds in silicon which require 105kcal/mole and 42.2kcal/mole of energy, respectively. The fluorine can then create Si-F bonds releasing 130kcal/mole of energy[78]. This process will not occur spontaneously as the process requires an additional 17kcal/mole of energy. However, the plasma itself can break the C-F bonds in CF_4 as well as Si-Si bonds on the surface due to ion bombardment. These effects remove virtually the entire energy barrier for the reaction. Even though fluorine based plasmas can etch silicon effectively, they do not produce good sidewall profiles. To achieve good sidewall anisotropy control, a sidewall passivation scheme is utilized.

This type of etch utilizes a component which tends to deposit a polymer on the surface of the sample. A schematic of the process is given in Figure 48. The polymer resists chemical etching and requires ion bombardment to dislodge. Therefore, on the planar regions of the sample, the etch rate is slowed, but etching continues as the polymer is removed by the ion bombardment. The best etches operate where the polymerization on the sidewall balances the slight ion bombardment and there is no buildup of polymers while maintaining a vertical profile. When there is excess polymerization, the profile slopes inward (positive profile) due to buildup of the polymer on the sidewalls. Polymerization in fluorine based etches is accomplished by increasing the carbon to fluorine ratio. When the carbon to fluorine ratio is high, fluorocarbon polymers, like PTFE, are formed which is an ideal polymerization compound as it is resistant to chemical attacks.

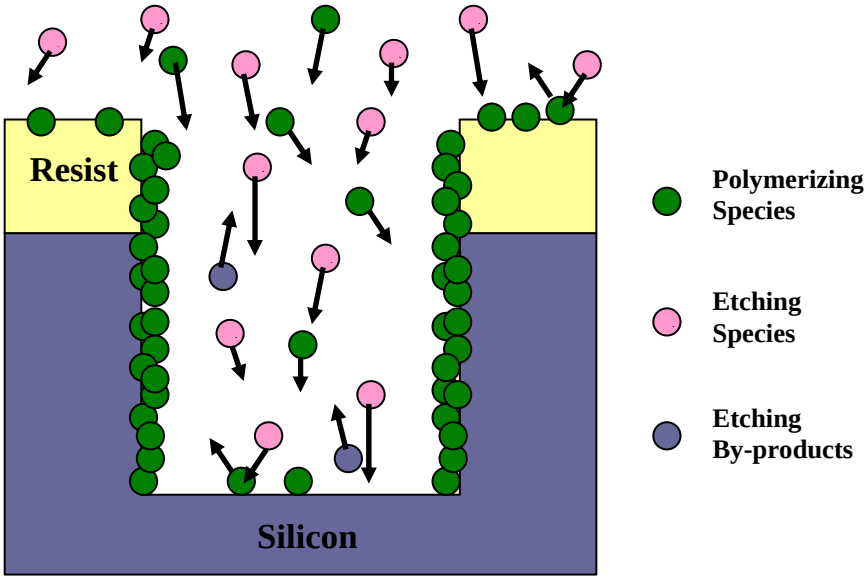

Figure 48. Schematic showing the profile control provided by a sidewall passivation etch where polymerizing species coat the sidewalls

Chlorine containing plasma etches operate in a fundamentally different manner than fluorine based etches. A pure chlorine plasma etches silicon very slowly without the presence of ion bombardment. The mechanism of the etching is believed to be due to formation of a layer of chlorine on the top of silicon by chemisorption. This layer of chlorine impedes the further absorption of chlorine molecules by stearic hindrance resulting in low etch rates in the absence of ion bombardment. In the presence of ion bombardment, the surface is damaged allowing chlorine atoms and ions to enter underneath this layer and dislodge the silicon atoms as volatile silicon chlorides. Since the etching mechanism relies heavily on the existence of ion bombardment, the etch profiles are almost completely anisotropic for undoped or lightly doped silicon. Dopants in silicon allow electrons to migrate to the chlorine layer on the surface causing ionic bonding between the chlorine and silicon, thus freeing the site for further chemisorption without ion bombardment[78]. Since the etching mechanism proceeds without ion bombardment, the profile becomes more isotropic. Another issue with chlorine etching is the formation of microtrenches[80]. Due to scattering and reflection of ions from the sidewalls, the incident ion bombardment reaches a maximum at a point near the edge of the trench. Figure 49 shows a cross section of a chlorine etch showing this microtrenching effect and the chlorine ion trajectories which cause this effect to occur. The microtrench forms near the edge of the trench, and then grows inward as the location of the concentration of reflected ions changes with the depth. To improve the profile, various gases are added in small quantities to the chlorine base etch. The most common of these are fluorine containing gases, such as CF_4 and C_2F_6, and polymerizing and inhibiting gases, such as BCl_3 and HBr[81,82]. Another major issue with chlorine based

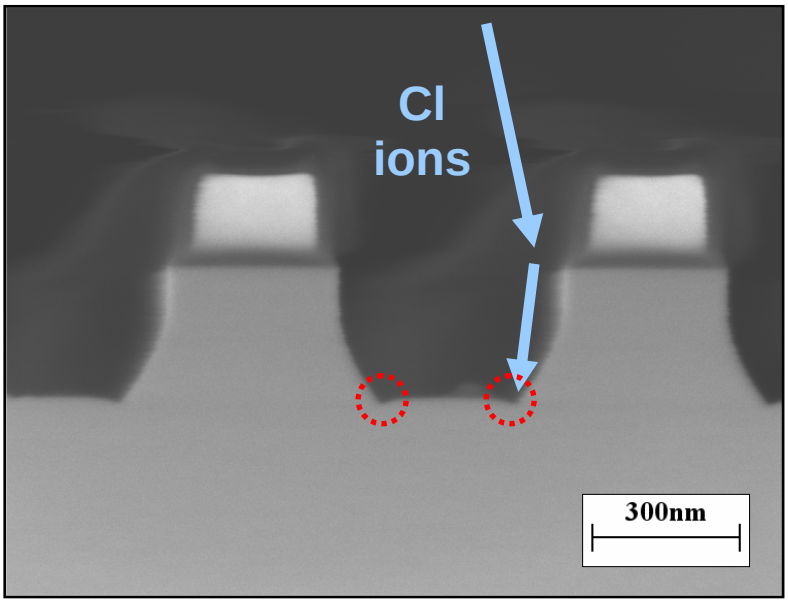

Figure 49. Cross section of a chlorine etch with microtrenching effect

etches is "grass". Due to the high level of anisotropy inherent in the chlorine etch, any small defects, such as incomplete development of the resist, redeposition of small particles of etched resist, deposition of contaminants in the chamber, and formation of small oxide particles from any oxygen containing gaseous species in the recipe, can become a starting point for "grass" to occur. Figure 50 shows an angled and a cross

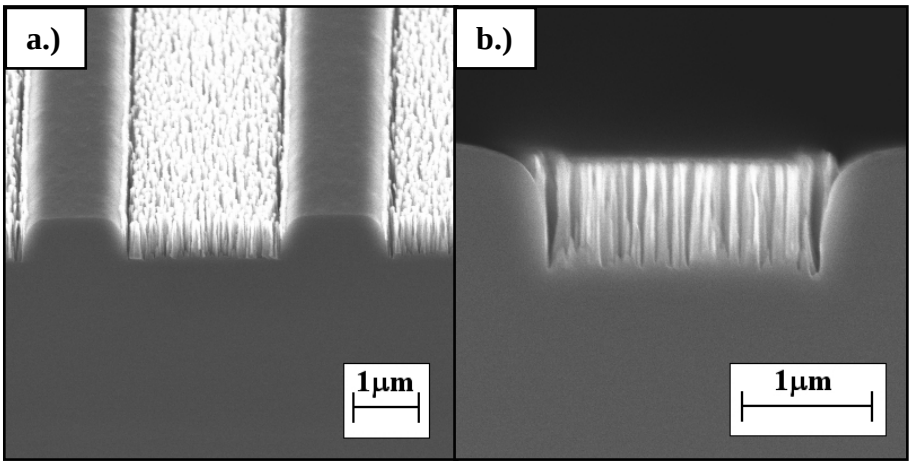

Figure 50. Angled view and a cross section of grass formation in a chlorine/oxygen plasma etch

section view of "grass" formation in a chlorine/oxygen plasma etch. Despite these limitations, a chlorine based etch was investigated in this thesis due to the anisotropy and smooth sidewalls obtainable in a suitably optimized chlorine etch.

Non-Chlorine Based Etch Results

Before describing the results obtained using the ICP and a chlorine based etch process, a brief description of the results obtained using other etching systems is given. The two other processes investigated were the utilization of an SF_6, O_2, and Ar plasma etching in the Plasmatherm RIE and the Bosch process etching in the STS ICP. The SF_6, O_2, and Ar etch in the RIE is a standard high fluorine content silicon etch. The cross section shown in Figure 51 illustrates that this recipe has significant isotropic component as depicted by the rounding and the spreading of the trench from the equal line and spacing pattern in the resist. The Bosch process, performed on the STS ICP equipment, is a two step cyclic etch where a polymerization step and an etch step are performed sequentially. In a manner similar to the polymerization etch, this process relies on the ion bombardment removing the polymer on the bottom faster than on the sidewalls. The etching step consists of a SF_6 and O_2 plasma which removes the polymer on the bottom

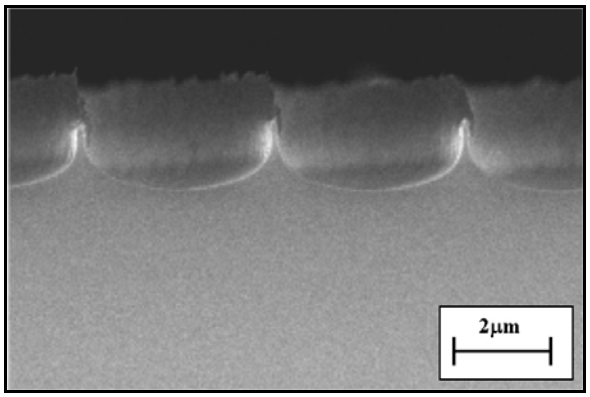

Figure 51. Cross section of 2 μm trenches etched using an SF6, O2, and Ar etch in the RIE

and etches isotropically to form a bowl. The passivation step coats all of the sidewalls with polymer and the process repeats itself. The drawback of the Bosch process is that due to its sequential nature, the sidewall develops periodic ridges as shown in Figure 52. The Bosch process was developed to perform fast deep etch in silicon for micromachining and MEMS applications, thus the sidewalls are not very smooth on the nanometer scale and depth control is hard to achieve in the hundreds of nanometer regime. For these reasons, the Bosch process was eliminated from further consideration. Due to limitations on the available gases on the RIE, further optimizations on the RIE were also foregone for added control and availability of numerous gas sources in the ICP.

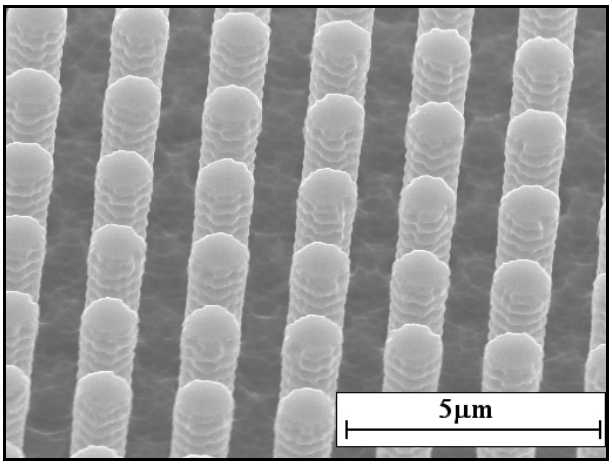

Figure 52. 1 μm sized pillars etched in silicon utilizing the Bosch process

ICP Etch Optimization

The equipment used for the ICP plasma etching is the Plasma-Therm Dual ICP SLR Mn F. ICP. This equipment contains two chambers. The right chamber is dedicated to running the Bosch process for deep silicon etching. The left chamber is equipped with 8 different gases to give a large degree of process control for etching a wide range of materials including silicon, silicon oxide, silicon nitride, gallium nitride, and indium

phosphide. The 8 gases currently configured on the equipment are: Cl_2, BCl_3, H_2, Ar, O_2, CF_4, C_4F_6, and CHF_3. The primary etching gases are chlorine, fluorine, oxygen, and argon, while the other 4 gases are for profile control to achieve anisotropic sidewalls. Etches containing BCl_3, H_2, C_4F_6, and CHF_3 deposit polymers on the chamber walls and require a chamber clean after each process to ensure repeatability of the results. The process development of the ICP processes begins with the characterization of the cleaning process. Then optimization of the various gas mixtures with the base chlorine recipe is investigated. Finally, the combination of Cl_2 with the C_4F_6 was determined to be the most promising and further optimizations were conducted on this mixture.

Cleaning Recipe Characterization

Ensuring that the chamber is clean is one of the most important steps in optimizing a process. In a shared working environment, such as the MiRC cleanroom, it is especially important to be cognizant of the state of the chamber to ensure consistent results. The cleanliness of the chamber is paramount to the ICP since it is used to process many different materials and the gases available for etching include those which polymerize and leave residues on the chamber walls. Of the gases that cause polymerization, C_4F_6 leaves the most residue and is one of the most commonly used gases for etching silicon oxide. The C_4F_6 based oxide etch is used as the standard contamination etch and the response of a high RF and low RF cleaning processes were monitored. For the two cleaning processes, the process pressure was 5mTorr, the gas flow was 40sccm O_2 and 5sccm Ar, and the coil RF (RF_2) was set to 800W. The high and low power cleaning processes have the parallel plate RF (RF_1) of 100W and 15W, respectively. Two parameters were monitored during the cleaning process. The first

parameter was the DC bias. The second parameter was the color of the plasma. The plasma color was observed to transition from a bright white color to a pink color as the cleaning proceeded. This is attributed to carbon and fluorine entering the plasma from the contamination, which turns the plasma white. The DC bias was compared to the value the process exhibited before contaminating the chamber. The DC bias monitoring, plotted in Figure 53, reveals two types of contamination present in the chamber. The initial peak in the curve reveals contamination that raises the DC bias of the cleaning process and is quickly removed. After this contamination is cleaned, there is still a tougher polymer, or redeposited inorganics, left on the chamber walls which takes much longer to remove to recover the clean state DC bias voltage. The initial peak corresponds to the time when the plasma color is white. The minimum point in the DC bias curve

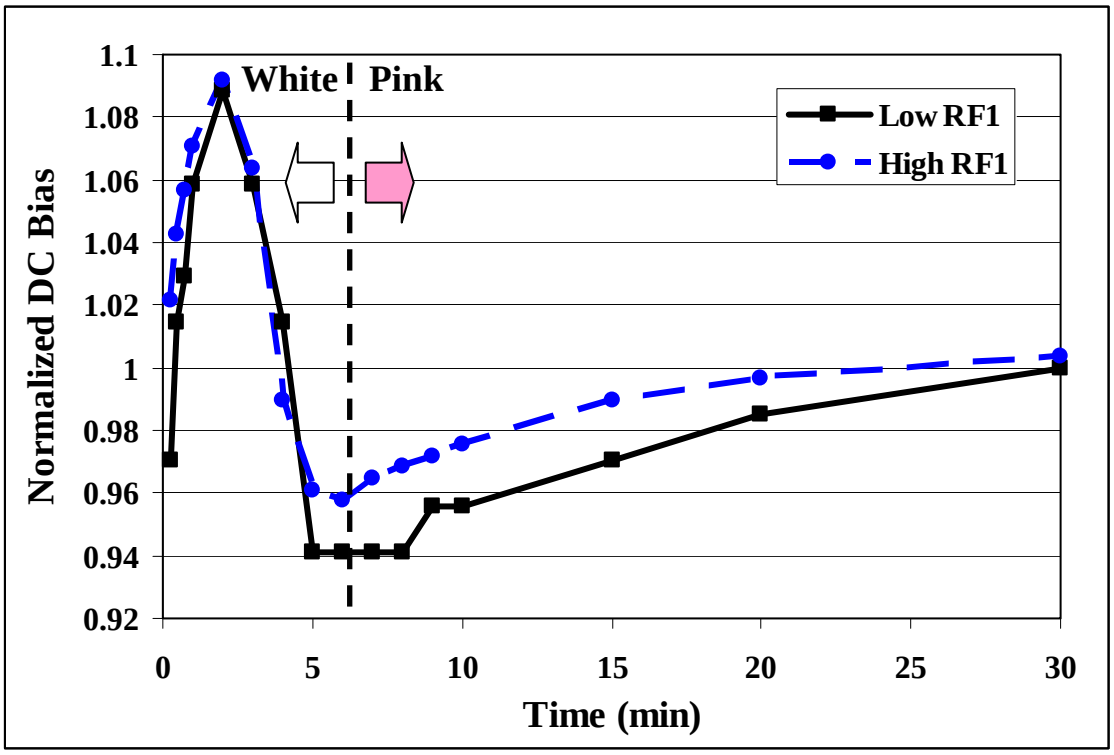

Figure 53. Monitored DC bias for two cleaning processes on the Plasmatherm ICP

represents the point where the plasma turns pink. It is crucial to clean the chamber until this point is reached since any etch performed with such a polymer on the chamber walls will result in excess fluorine and carbon molecules affecting the balance of the gaseous species. The contamination left on the chamber walls beyond this point in the cleaning are not easily removed and acts only to decrease the effective area of the top electrode through an insulating film. The decrease in the effective area of the top electrode decreases the DC bias voltage slightly. However, since the chemistry of the etch is not affected, it is possible to increase the RF_1 power to compensate for the decrease in the voltage to achieve consistent results. Also, the RF_1 power of the cleaning process did not appear to affect the effectiveness significantly as seen by the close matching of the two curves. The high RF_1 clean is slightly faster than the low RF_1 clean for the second stage cleaning, but shows negligible improvement in removing the initial polymerization from the walls.

Chlorine Based Recipe - Gas Mixture Survey

Once the chamber cleaning process was characterized, a survey of the gas mixture was conducted. For the survey, the RF powers were set to 3W for RF_1 and 600W for RF_2. These powers were chosen based on preliminary results which suggest that the ZEP-520A etch rate is strongly related to the DC bias voltage. Since the DC bias voltage is most strongly related to the RF_1 power, the RF_1 power was lowered to as low as the equipment would allow while the RF_2 power was raised to a high value to increase the ion density which increases the etch rate of the silicon. The total flow rate of the gases and the process pressure were kept constant at 20sccm and 5mTorr, respectively. The etching was conducted for 2minutes for each sample. The ignition of the plasma required

a higher RF_1 power, so a 10 second spark step at 10W RF_1 was added before lowering down the power to 3W. Oxygen, argon, and CF_4 have been reported in the literature to give good sidewall profiles free from microtrenching[80-82]. In addition to these gases, a mixture of chlorine with polymerizing gases, such as BCl_3, CHF_3, and C_4F_6 were evaluated. The concentration of the gases was set to 10%, 15%, and 20%. Figure 54 is a cross section of a pure chlorine recipe where microtrenching has occurred to give the sidewalls a sloped profile as well as a knotch on the bottom plane. The trenches were patterned using the EBL system for equal line and spacing with sizes of 1 μm and 300 nm; however, due to overdosing effects, the trenches were larger than the remaining resist.

The addition of oxygen to chlorine plasmas creates silicon oxide on the surface which can not be removed without significant ion bombardment. Therefore, the oxygen acts similarly to a polymerization gas for controlling the sidewall profile. Chlorine does not chemically etch silicon oxide and only sputtering by the ions removes the silicon oxide. However, the recipe is prone to "grass" as uneven oxidation of the surface, or any gas phase reactions creating small particles of silicon oxide landing on the surface, can

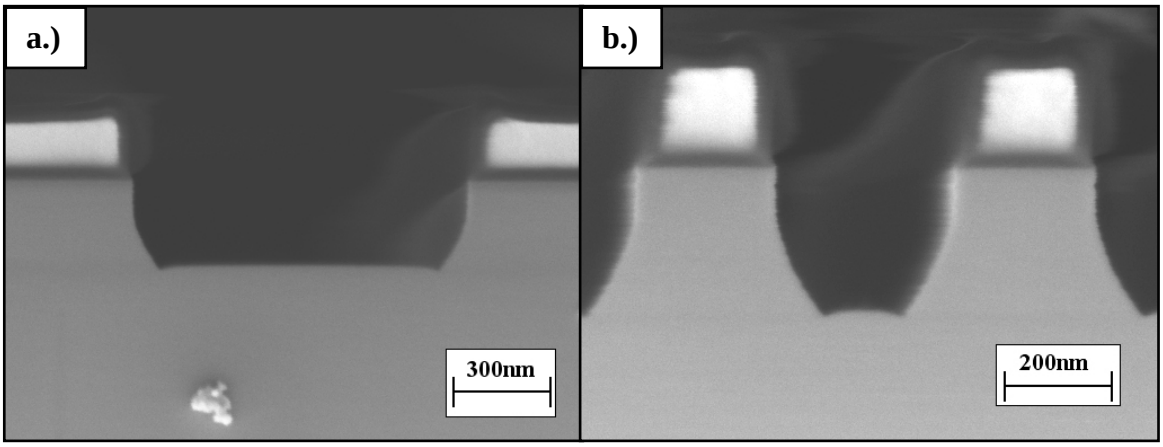

Figure 54. Pure chlorine etch of silicon trenches with a pitch of a.) 2 μm and b.) 600 nm

initiate “grass”. All of the recipes utilizing oxygen showed significant “grassing”. Also, for the conditions tested, all of the recipes utilizing argon showed significant “grassing”. The “grassing” in the recipes with argon can be due to the redeposition of sputtered resist onto the exposed areas of the sample. Due to this problem, additional recipes utilizing chlorine mixed with oxygen and argon were not investigated.

The next set of mixtures investigated was the addition of fluorine. Addition of fluorine adds an isotropic component to the etching which prevents grassing. The combination of chlorine and CF_4 was investigated and the results are shown in Figure 55. The most striking result is the undercutting of the resist caused by the addition of CF_4. The bottom of the undercut is well aligned with the edge of the resist. The angle of the undercut increases with increasing ratio of CF_4. In addition, the selectivity, defined by the ratio of the etch rate of the target material divided by the etch rate of the resist, decreases with increasing CF_4. This is apparent due to the depth of etched silicon remaining relatively constant while the resist thickness decreased with increasing CF_4 concentration. The addition of fluorine eliminated “grassing” and microtrenching, but added an undercut and taper. The undercut and taper follow a consistent trend with the CF_4 concentration and can be useful for making controlled wedges and points for probes or MEMS applications. However, this taper is undesirable in photonic crystal fabrication. To eliminate this effect, CHF_3 was investigated for the gas mixture instead of CF_4. In fluorine based etches, CHF_3 acts as a polymerizing gas. CHF_3 has the potential to act as both a source of fluorine for suppressing the grass and as a polymerizing gas to obtain a better sidewall profile. Figure 56 shows the results for this series of recipes. The CHF_3 does provide fluorine to the plasma as seen in the undercutting profile, but did not have a

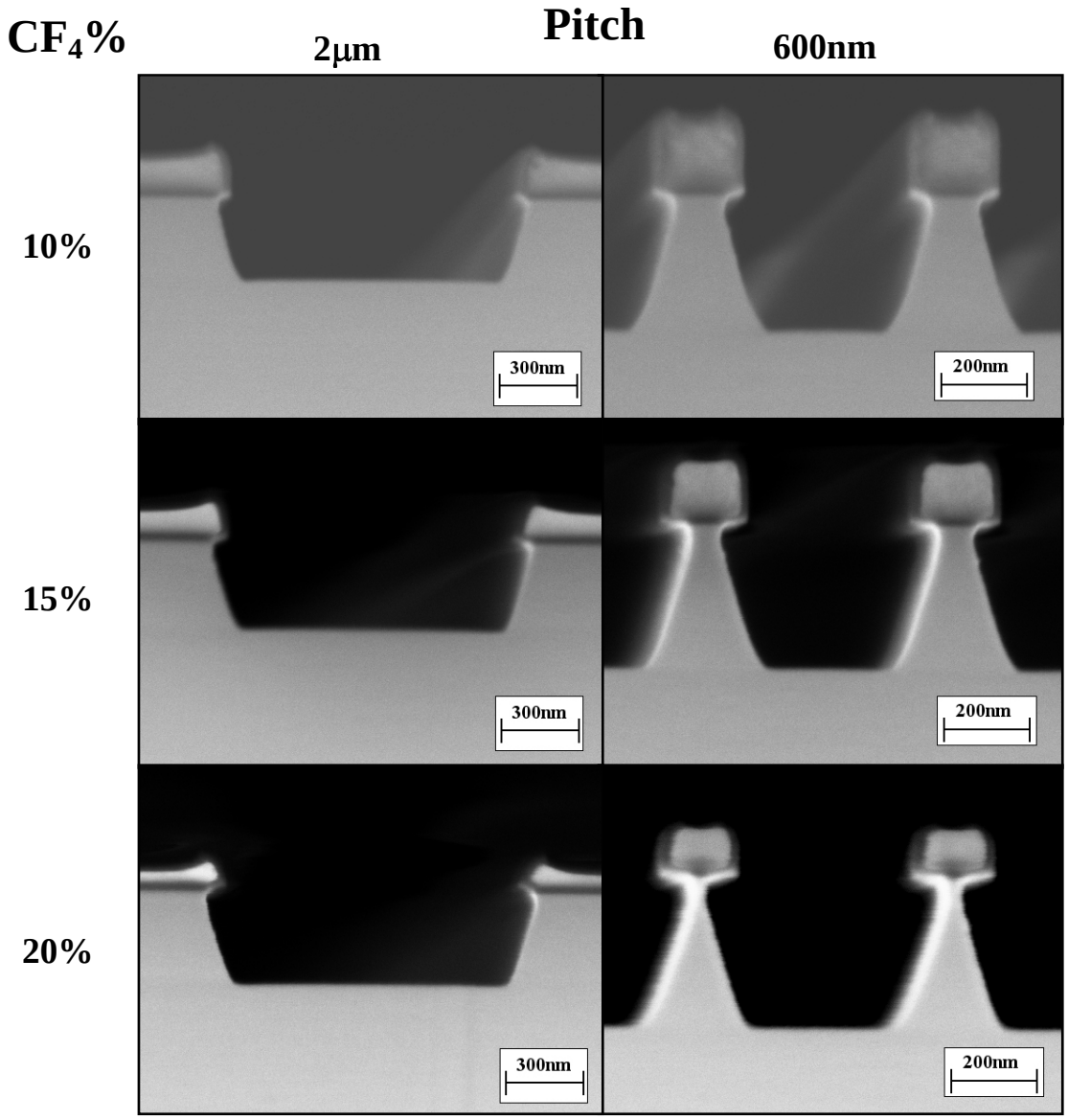

Figure 55. Cross sections of silicon etched utilizing a mixture of Cl_2 and CF_4. The concentration of CF_4 in the recipe and the pitch of the trenches are labeled.

strong polymerizing effect on the sidewalls of the silicon which can be attributed to the hydrogen and carbon forming compounds with chlorine instead of forming a polymer. Unlike CF_4, the CHF_3 did not significantly affect the etch rate of the resist due to the smaller fraction of fluorine formed, and the ability of non-fluorine by-products to attach and polymerize on the resist. Also, unlike the CF_4, the CHF_3 showed the largest undercut for the smallest concentration of CHF_3 due to the excess carbon and hydrogen acting to keep the fluorine concentration relatively constant even with increasing CHF_3 content while providing stronger polymerization. CF_4 and CHF_3 proved to be useful to produce controlled tapers and undercut the resist, but did not provide smooth vertical sidewalls necessary for photonic crystal fabrication.

In addition to the CHF_3, BCl_3 is another polymerizing gas and is one of the standard polymerization gas utilized in a chlorine based etch. The results of the recipes utilizing BCl_3 are given in Figure 57. The BCl_3 recipes did not show any undercutting. The 10% and 15% concentrations seemed to make very little difference with the pure chlorine etch as it still showed the microtrenching and the tapered sidewalls. One difference between the pure chlorine etch was that the tapering starts at the boundary of the resist and the silicon, rather than after a small amount of vertical etching for the pure chlorine case. The highest concentration of BCl_3 at 20% gives better results with respect to the degree of microtrenching and also a more vertical profile. BCl_3 recipes also show a better selectivity compared to the other etches evaluated. However, the profile is still far from the desired vertical profile.

The final gas available on the Plasmatherm ICP was C_4F_6. This gas is a highly polymerizing gas which is utilized in silicon oxide etching to increase selectivity with the

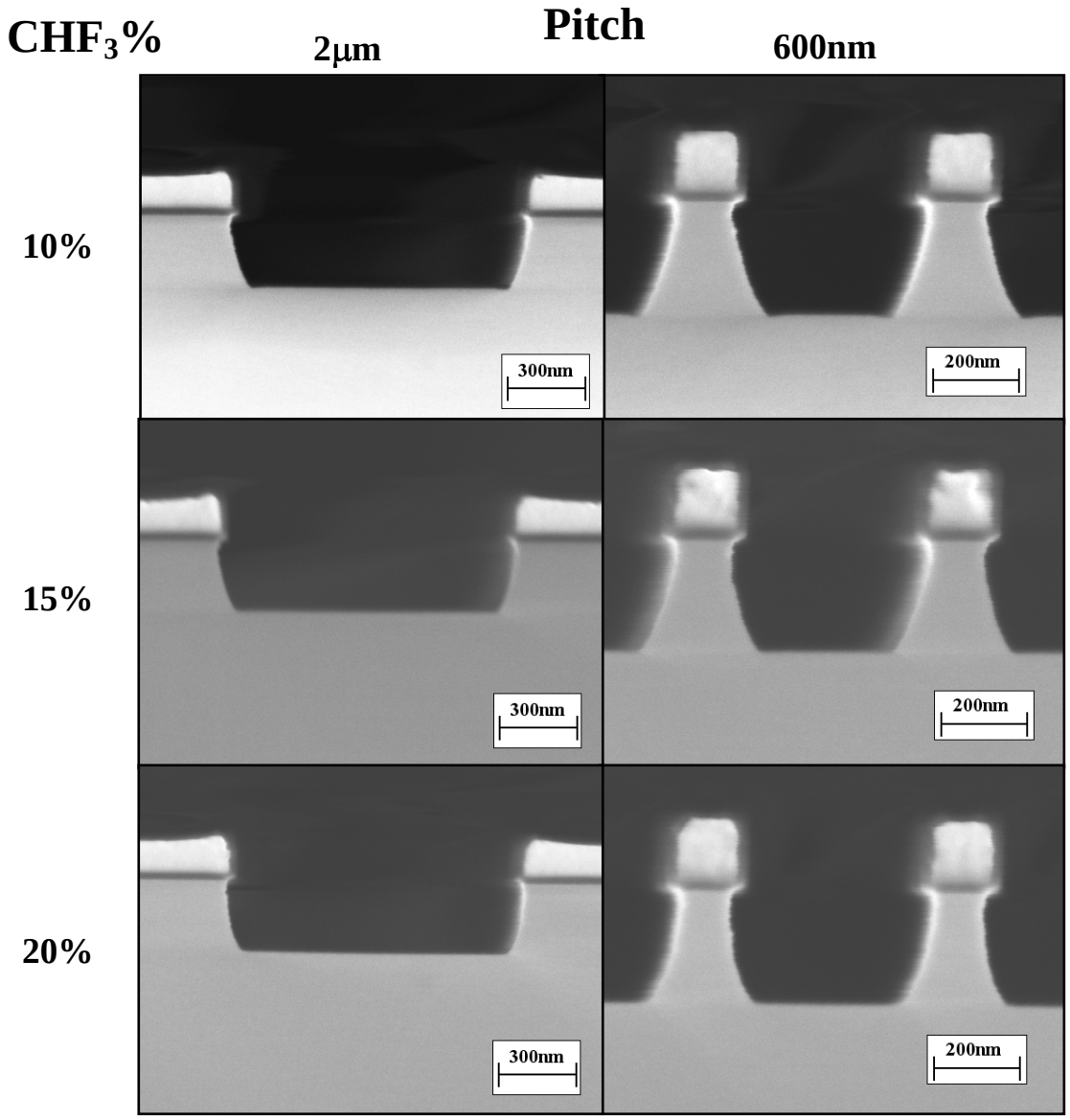

Figure 56. Cross section of silicon etched utilizing a mixture of Cl_2 and CHF_3. The concentration of CHF_3 in the recipe and the pitch of the trenches are labeled.

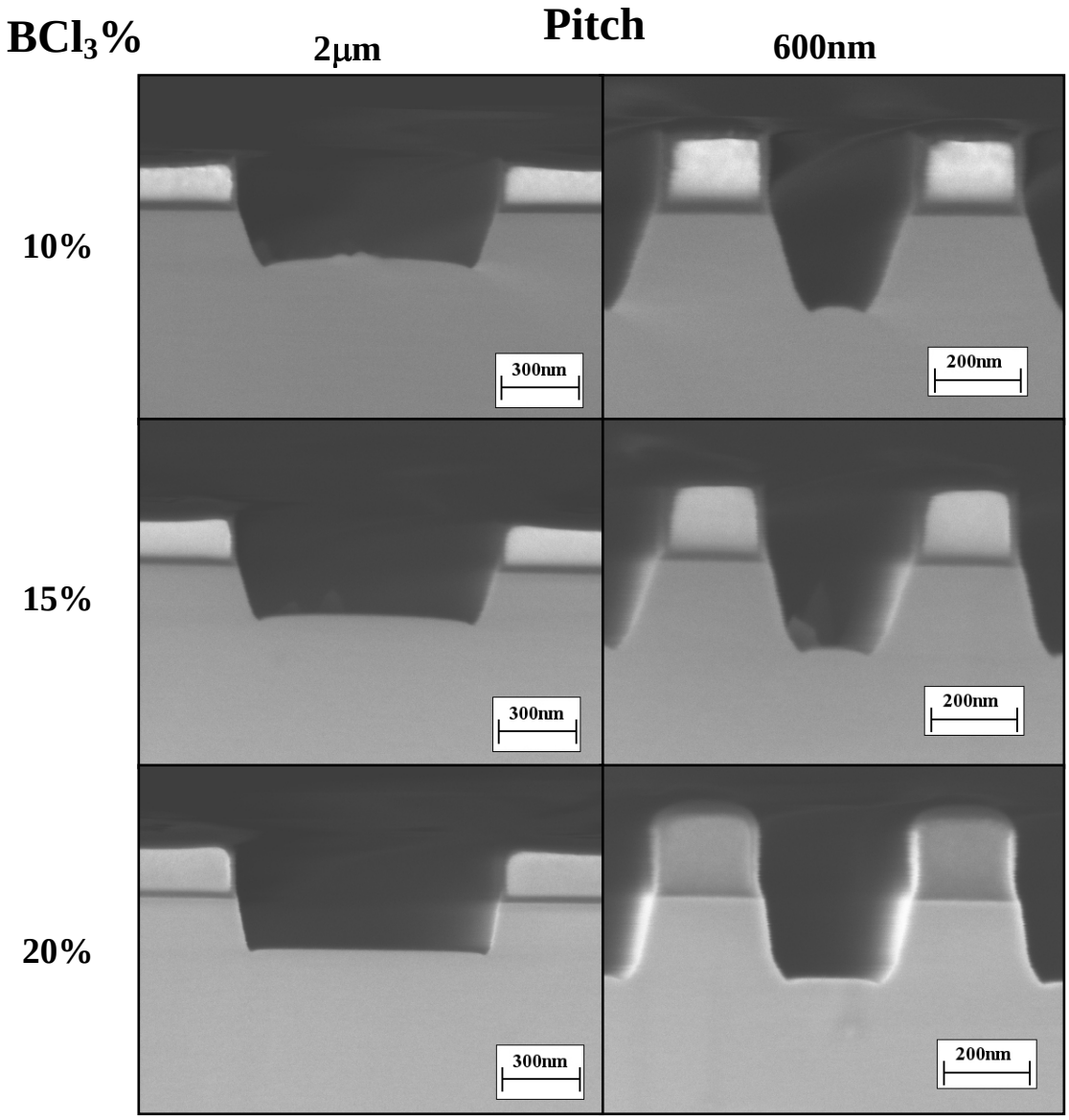

Figure 57. Cross section of silicon etched utilizing a mixture of Cl_2 and BCl_3. The concentration of BCl_3 in the recipe and the pitch of the trenches are labeled

photoresist. The C_4F_6 is also a fluorine containing compound, and thus can be expected to release fluorine as it breaks down in the plasma. The other likely molecules for the C_4F_6 to break down into are C_2F_3 or other combinations of carbon and fluorine containing double bonds between the carbons. These molecules can react with each other to form a fluorocarbon much more readily than the smaller molecules resulting from recipes containing CF_4/H_2 or CHF_3. Therefore, recipes utilizing C_4F_6 are expected to have very strong sidewall polymerization with a small component of fluorine to help prevent "grass." Figure 58 shows that this set of recipes was the best out of the gas mixtures surveyed. The 10% concentration recipe showed only minor improvements from the pure chlorine etch. However, with increasing concentration of C_4F_6, the sidewalls maintained a vertical profile with only slight rounding near the bottom of the trench. The 20% concentration of C_4F_6 in chlorine resulted in the desired vertical profile and good selectivity with the ZEP-520A resist. This base recipe consisting of 16sccm Cl_2, 4sccm C_4F_6, with a processing pressure of 5mTorr and RF powers of 3W RF_1 and 600W RF_2, was chosen for further optimization to achieve smooth vertical sidewalls for photonic crystal fabrication.

Optimization of Chlorine/C_4F_6 Recipe

From the survey of gas mixtures, the 20% mixture of C_4F_6 with chlorine gas was found to give the best profile. Further quantitative optimizations on this base recipe were conducted to improve on the selectivity, etch rate, and anisotropy and to understand the mechanism of the profile control. The RF power, process pressure, and the gas flow rate were modified, and a cross section using the SEM was taken to measure the etch rate of

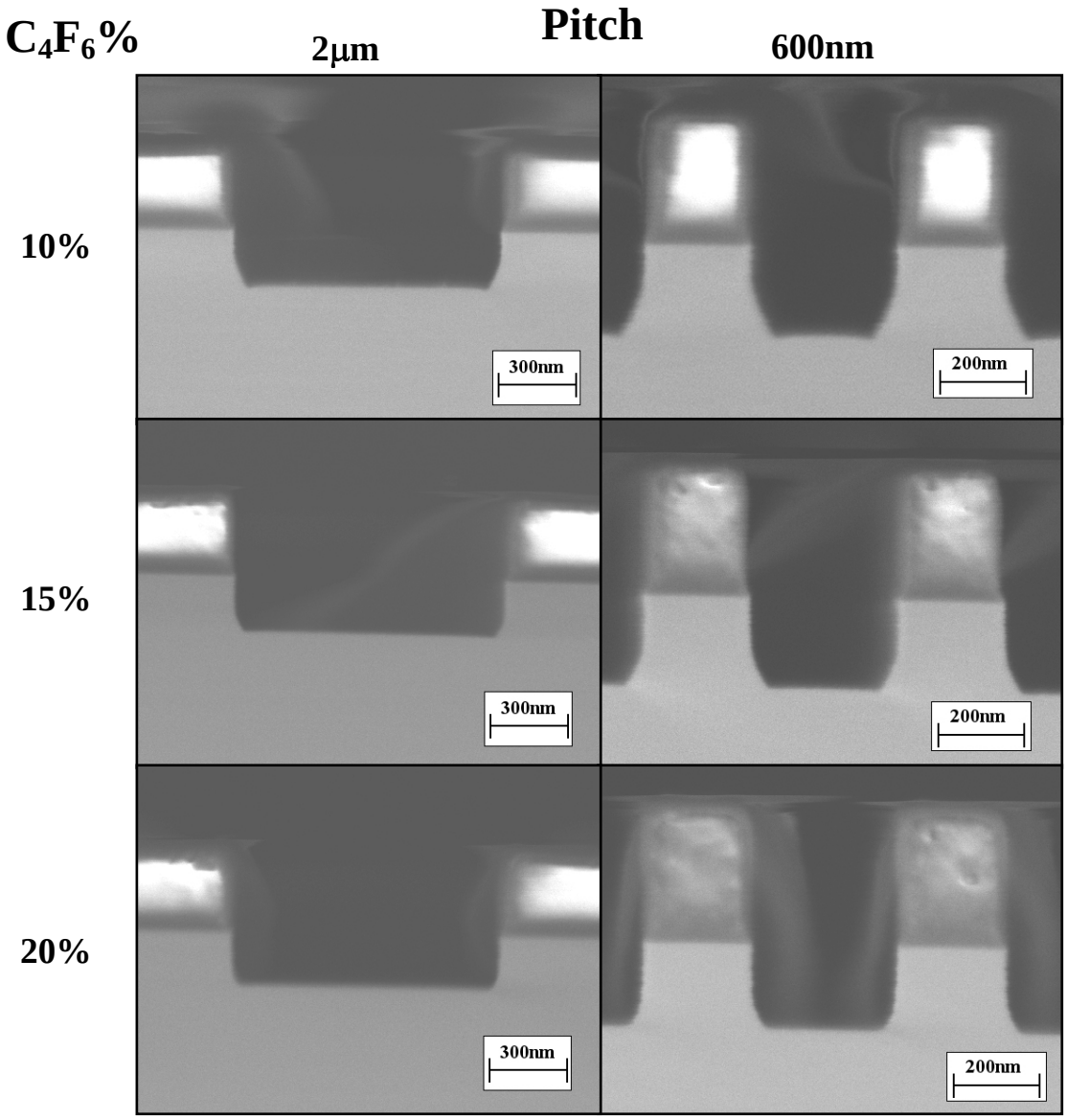

Figure 58. Cross section of silicon etched utilizing a mixture of Cl_2 and C_4F_6. The concentration of C_4F_6 in the recipe and the pitch of the trenches are labeled

the silicon and the resist as well as observing the sidewall profile. A 2 minute etch time was maintained for the optimization. A longer recipe was investigated after the optimization to develop the capability of etching deeper, higher aspect ratio features.

The first parameter tested was the RF power. The RF_1 power was raised from 3W in the base recipe to a value as high as 15W. The etch rate of the silicon and the resist and the selectivity of silicon over the resist is plotted in Figure 59. Both the silicon and the resist etch rate increased with RF_1 as expected since the RF_1 is the main power affecting the DC bias. By increasing the DC bias, the ions are accelerated more towards the sample resulting in stronger ion bombardment and sputtering. As seen by the selectivity curve, the silicon etch rate does not increase as much as the resist. This trend agrees well with the mechanism of the chlorine based etch. The chlorine does not

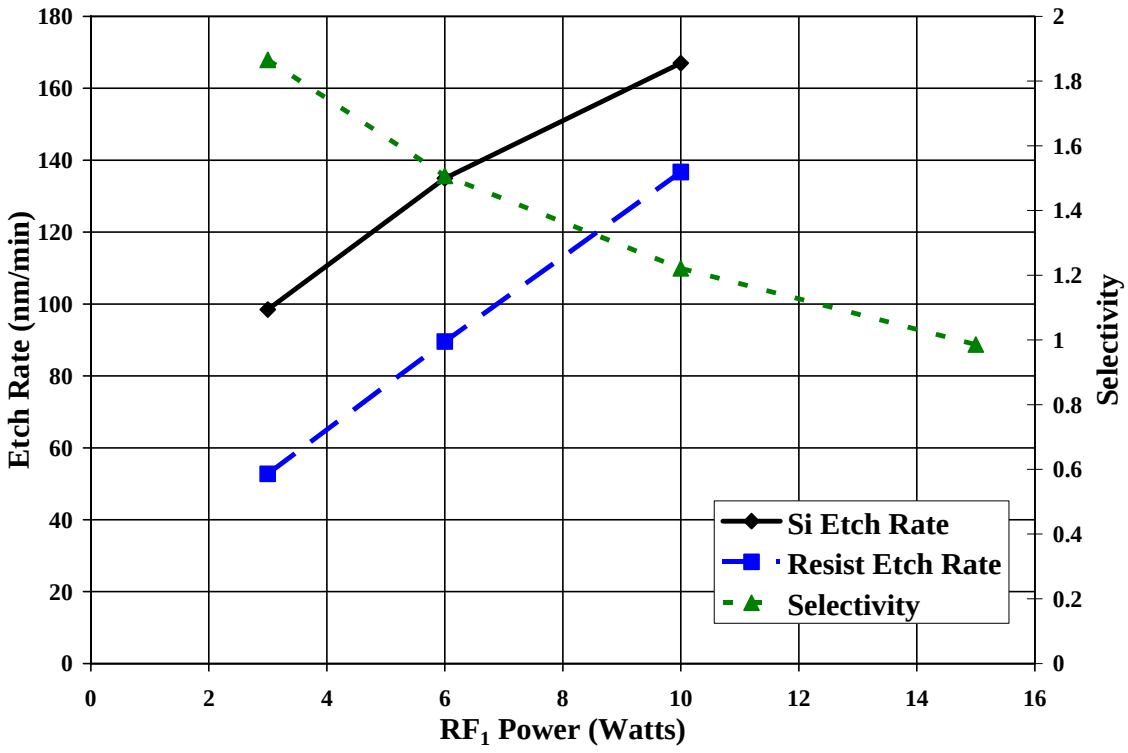

Figure 59. Etch rate and selectivity with respect to the RF_1 power

directly attack the resist, but the resist is a very soft material compared to silicon and sputters easily with increasing ion bombardment. Inorganic materials such as silicon are much harder to sputter, thus the increase in the silicon etch rate is not as high as for the resist due to the chemical nature of the silicon etching. At 15W RF_1 power, the entire 425 nm thick ZEP was etched in 2 minutes. Therefore, the etch rate of the silicon and the resist cannot be determined, but the selectivity can be estimated through the height of the remaining trench. As the RF_1 power was increased, the microtrenching effect started to appear due to a higher component of the etching occurring from the effects of ion bombardment. As expected from the original choice of RF_1, a lower RF_1 power increased the selectivity to the resist as the resist etching rate is a strong function of the RF_1 power. Using the 3W RF_1 power, the RF_2 power was varied from 400W to 900W and the results are shown in Figure 60. Within this range, the resist etch rate stayed relatively constant. The resist etch rate reached a maximum for 600W and was slightly lower for both higher and lower RF_2 power. The initial increase in the etch rate between 400W and 600W was attributed due to the higher density of ions with increasing RF_2. The subsequent decrease shows that there is a balance where the formation of polymerizing species from the C_4F_6 overwhelms the etching fluorine and chlorine species and results in a lower etch rate of the resist. The silicon etch rate increased linearly with RF_2 power from 400W to 800W, but saturated and decreased slightly when the power was raised to 900W. At high RF_2 power, the ion density was so high that the ion bombardment cannot keep up with the influx of ions and the silicon etch rate saturates[81]. To achieve good selectivity with the ZEP-520A resist, a low RF_1 power of 3W and a RF_2 power of around 800W was found to be optimal. All of the sidewall angles measured for

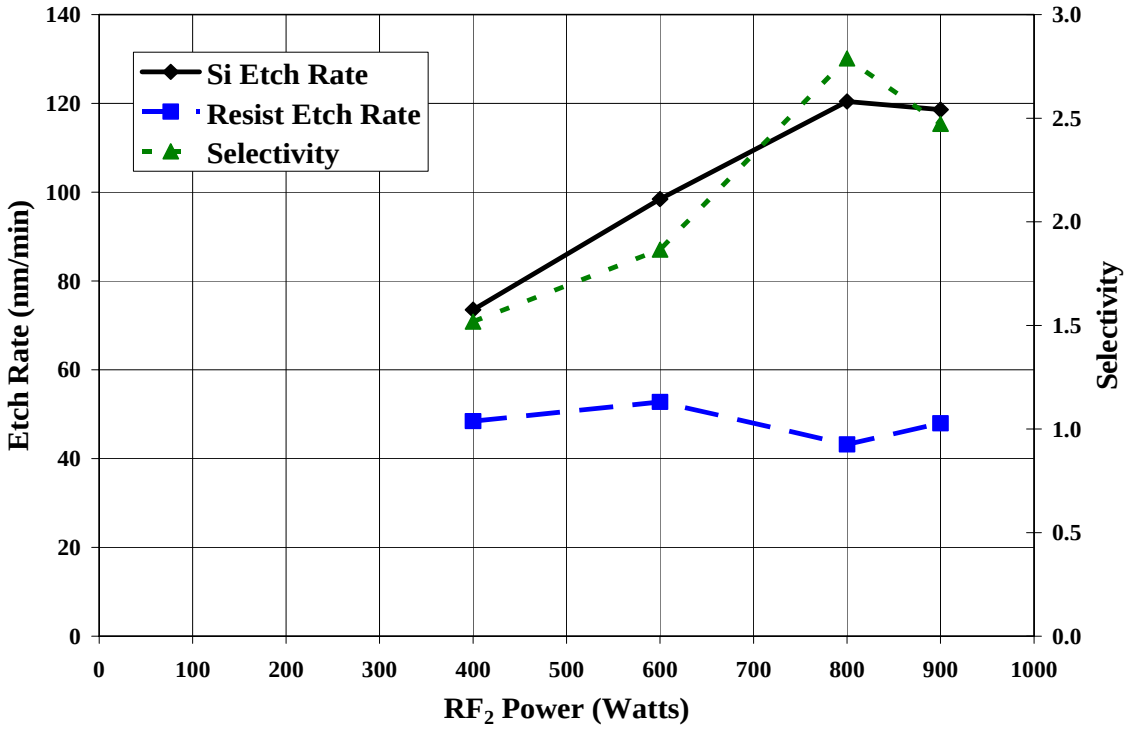

Figure 60. Etch rate and selectivity with respect to RF_2 power

this series of experiments were under 2° off vertical, with a positive slope, other than the 15W RF_1 sample which showed a larger angle of ~5° and the formation of microtrenches. This was expected as the higher RF_1 power setting results in more ions having the velocity necessary to graze off of the sidewalls and to increase the ion flux at the corners. The base recipe and the recipe's with higher RF_2 showed the best sidewall profile with a measured angle of under 1° off vertical. The case where RF_2 was dropped to 400W and the cases with higher RF_1 showed moderate results where the angle was, on average, within 2°. Table 2 at the end of this section presents an overview of all of the relevant parameters with the data for all of the recipes performed for the optimization.

Through the RF power optimization, both the etch rate and selectivity was found to be optimal with an RF_2 power of 800W. Further tests were conducted using the 800W

and 900W powers. The next parameters optimized were the gas flow rate and the process pressure. As mentioned earlier, the process pressure determines the density of gases in the chamber and their mean free path. The total gas flow dictates how quickly the gas mixture is cycled through the chamber. A lower process pressure results in a lower density of gaseous species which are affected by the RF power as well as a larger mean free path. Ions can obtain a higher velocity resulting in higher sputtering rates. Since sputtering is more effective for soft material such as the resist, a lower process pressure was expected to have worse selectivity with the resist. A higher gas flow rate results in faster recycling of the gas mixture which pumps out the etching by-products and increases the etch rate. The etch rates and the selectivity are graphed in Figure 61~63. The etch rates did not follow the expected trends as the effect of these parameters on the polymerization was dominant. The etch rate initially increased for a process pressure of 5mTorr and 2.5mTorr cases where the supply of chlorine was too low at a flow rate of 10sccm. However, for flow rates greater than 20sccm, the etch rate of silicon decreased for all pressures. This result suggests that the increased flow of the C_4F_6 gas increases the polymerization more than the benefit of removing the by-products. The effect of the resist etch rate emphasizes the increase in polymerization with increasing gas flow rate as the etching turns into a deposition for the two high flow recipes utilizing a 900W RF_2 power setting. Since the polymerizing gases attach to all surfaces they come in contact with, the increased replenishment of these species affects the etching process much more than the removal of the trace amounts of the etching by-products. The selectivity was not plotted for the cases where a net deposition occurred on the resist. However, the trend of increasing selectivity with increasing total gas flow is evident. The selectivity was

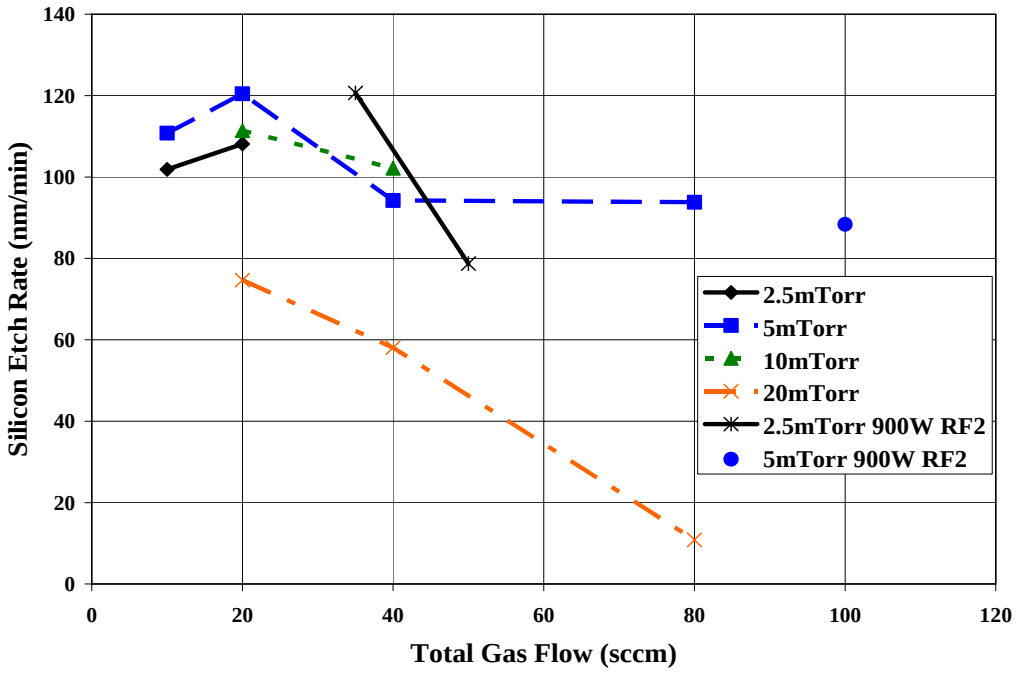

Figure 61. Silicon etch rate for different process pressures and RF_2 power with respect to total gas flow

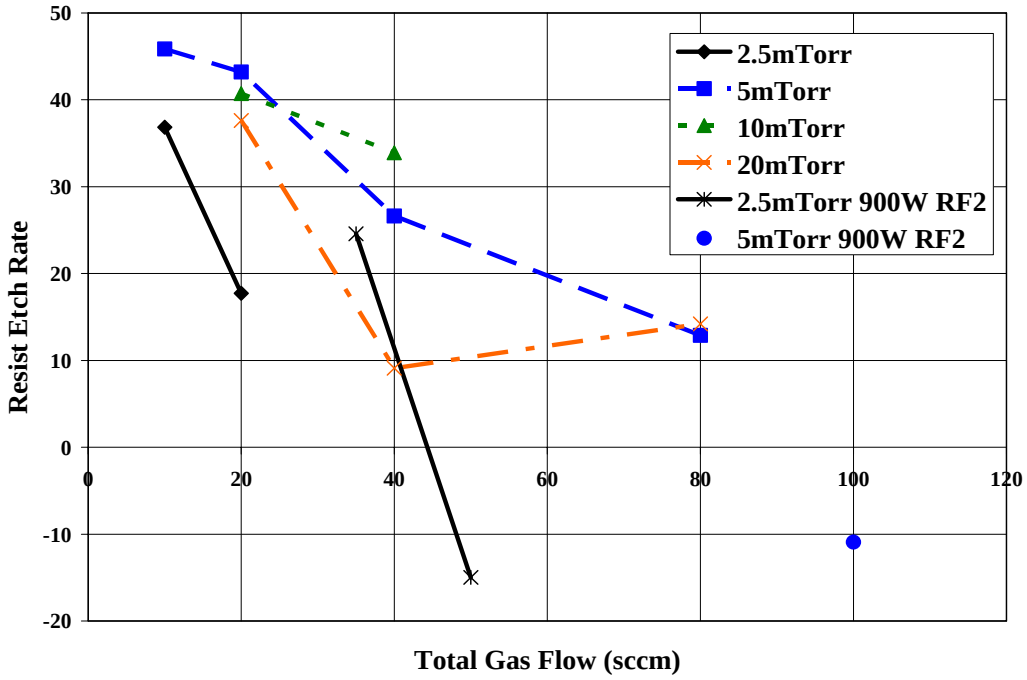

Figure 62. Resist etch rate for different process pressures and RF_2 power with respect to total gas flow

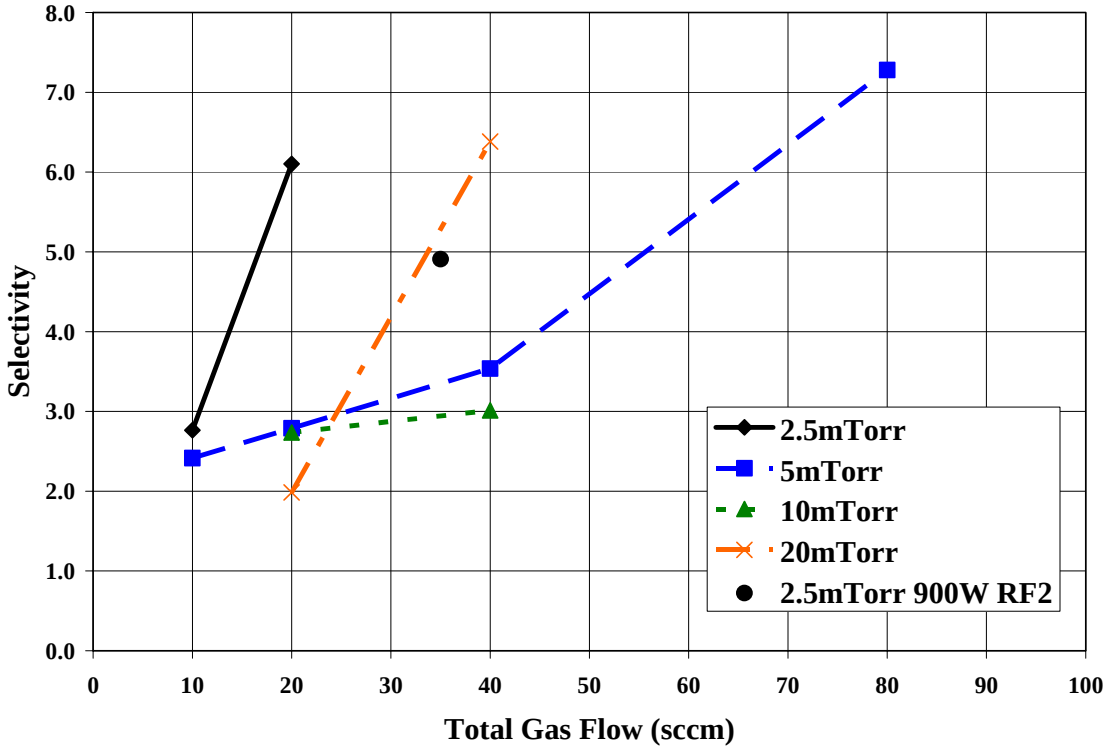

Figure 63. Selectivity of silicon versus ZEP-520A resist for different process pressures and RF_2 power with respect to total gas flow

enhanced due to the significant reduction of the resist etch rate while the silicon etch rate was less affected by the total gas flow. Even though the processes at 2.5mTorr showed a higher selectivity compared to recipes developed at higher pressures, the quality was lower with larger sidewall angles and some evidence of "grassing." The 20mTorr recipes exhibited a small undercut similar to the recipes containing CF_4 and CHF_3 as expected for a higher process pressure where isotropic etching conditions develop. A higher flow of C_4F_6 rounded the corners at the bottom of the sidewall while at lower concentrations, a sharp elbow developed. A higher flow of C_4F_6 also resulted in increased "grassing." Based on the optimization performed, three etches were chosen for device fabrication: Base recipe (3W RF_1, 600W RF_2, 5mTorr, 20sccm flow), base recipe with 800W RF_2, and base recipe with 800W RF_2 and 40sccm flow. The base recipe exhibited the most

consistent and repeatable sidewall profiles and was the preferred recipe. As the RF_2 and flow rates were increased, the recipes exhibited more variability with chamber cleanliness and less consistency. However, for cases where a thinner resist is required in the EBL exposure, the higher selectivity recipes are required.

A recipe for highly anisotropic shallow silicon etching was developed in the optimization experiments outlined above. Most of the recipes resulted in the removal of 150~200 nm of silicon, which is slightly short of the 200-300 nm depth range that is necessary for photonic crystal devices. Investigation of longer recipes revealed that the C_4F_6 gas contaminated the chamber and the etching characteristics start to change drastically after approximately 4 minutes. For longer etches, the C_4F_6 concentration and the RF_1 power had to be modified to maintain a vertical profile. This allowed an etching depth of approximately 350 nm utilizing the developed recipes, which is adequate for photonic crystal fabrication. The longer recipes provided insight into the mechanism of the Cl_2/C_4F_6 etch. Figure 64 shows the polymerization occurring on the sidewalls for a 4 minute recipe with 25% C_4F_6 concentration etch and for a 10 minute etch utilizing the 900W RF_2 and 100sccm total flow recipes. Both of these etches are highly polymerizing with the polymer buildup clearly visible. The 4 minute etch exhibits the mechanism of

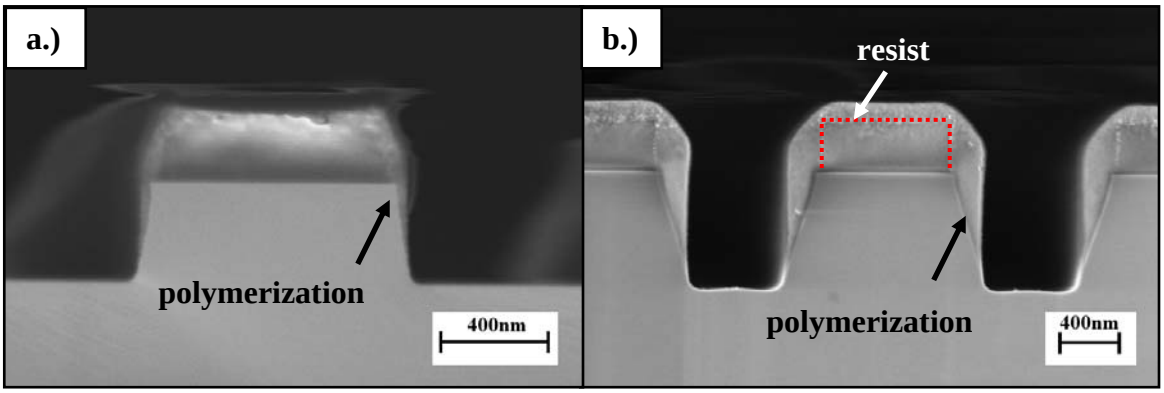

Figure 64. Polymerization on the side walls of deep etching recipes. a.) 4min recipe b.) 10min recipe

the profile control and the suppression of microtrenching. The polymer created a thin layer on the sidewall of the silicon, which prevented the chlorine ions from reflecting off of the sidewalls. The 10 minute recipe shows that for the first 100~150 nm of silicon etched, the profile is nearly vertical, but as the etch progressed, the sidewall angle gradually increased as polymerization builds on the sidewalls. To accommodate for the contamination during the etch, a lower C_4F_6 concentration with a higher total flow rate of 80sccm was investigated. The lower C_4F_6 concentration still maintained good selectivity with the resist, but, as depicted in Figure 65, microtrenching-like elbow shape occurred near the bottom of the trench as the concentration of C_4F_6 decreased. The C_4F_6 does not penetrate as deep as the fluorine and chlorine species, thus the profile becomes reentrant due to the fluorine and chlorine forming microtrenches at a depth where the C_4F_6 concentration has lowered to a sufficient degree. Successful anisotropic deep etching of silicon, shown in Figure 66, was achieved by ramping up both the concentration of C_4F_6 and the RF_1 power to help push the C_4F_6 molecules further down into the trench without having significant buildup of the polymerization on the resist.

The Cl_2/C_4F_6 etch was optimized to obtain highly selective, anisotropic etching of features in the size range required for photonic crystal device fabrication. It was verified that the recipes developed performed well for features down to 150 nm in width and up to 1.5 μm deep. Polymerization on the chamber walls makes long and deep etches difficult, but feature depth in the 200-300 nm range necessary for SOI based photonic crystal devices can be etched consistently with smooth, vertical sidewalls.

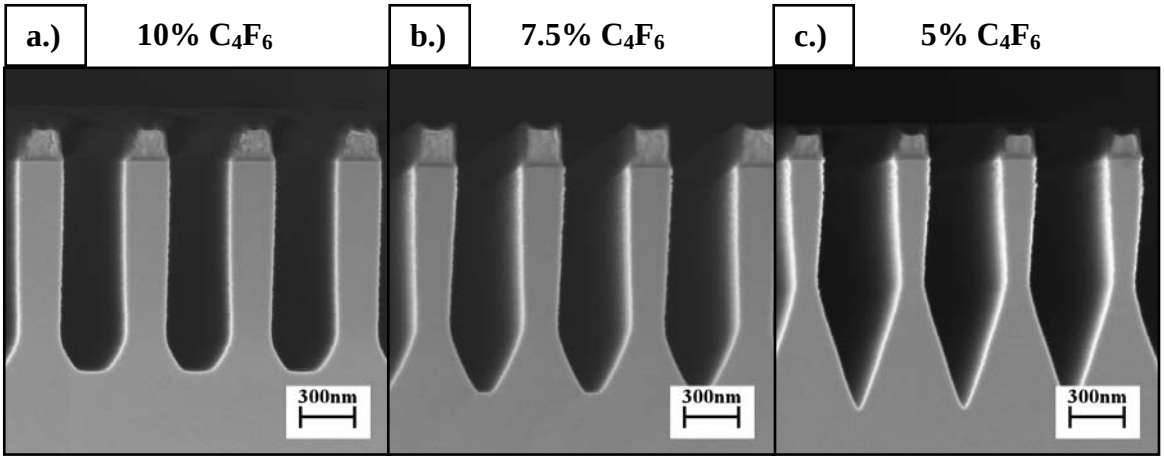

Figure 65. Deep etching characteristics of silicon showing increasing microtrenching with decreasing C_4F_6 concentration

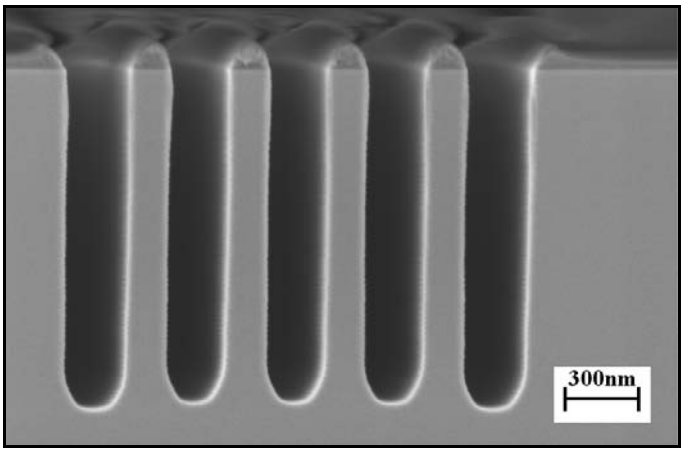

Figure 66. Deep vertical trenches etched by Cl_2/C_4F_6 plasma by ramping both the concentration of C_4F_6 and the RF_1 power from 10% to 20% concentration and 3W to 7.5W, respectively

Table 2. Overview of etches performed for optimization of etch rates, selectivity, and sidewall profile

RF_1 (W)	RF_2 (W)	Pressure (mTorr)	Cl_2 Flow (sccm)	C_4F_6 Flow (sccm)	Time (min)	Si Etch Rate (nm/min)	Resist Etch rate (nm/min)	Selectivity	Sidewall Angle	Comments
3	600	5	18	2	2	107.1	58.7	1.82	<1	Large elbow
3	600	5	17	3	2	106.9	55.5	1.93	<1	Large elbow
3	600	5	16	4	2	98.4	52.8	1.87	<1	Slight elbow
6	600	5	16	4	2	135.0	89.5	1.51	<2	Slight elbow
10	600	5	16	4	2	167.0	136.7	1.22	<2	Slight elbow
15	600	5	16	4	2	209.5	212.5	0.99	<5	Elbow and microtrenching
3	400	5	16	4	2	73.5	48.4	1.52	<2	Slight elbow
3	800	5	16	4	2	120.5	43.2	2.79	<1	Slight elbow
3	900	5	16	4	2	118.6	48.0	2.47	<1	Slight elbow
3	800	5	8	2	2	110.8	45.9	2.42	<1	Slight elbow
3	800	5	32	8	2	94.2	26.6	3.54	<2	Slightly rounded bottom
3	800	5	64	16	2	93.8	12.9	7.28	<2	Small amount of grass
3	900	5	80	20	2	88.4	-10.9	-8.09	<2	Small amount of grass
3	800	2.5	8	2	2	101.9	36.8	2.76	<1	Small amount of grass
3	800	2.5	16	4	2	108.1	17.7	6.10	<5	Rounded bottom
3	900	2.5	28	7	2	120.7	24.6	4.91	<5	Rounded bottom
3	900	2.5	40	10	2	78.7	-15.0	-5.25	>10	Wavy uneven bottom
3	800	10	16	4	2	111.4	40.7	2.74	<1	Slight elbow
3	800	10	32	8	2	102.2	33.9	3.01	<1	Slightly rounded bottom
3	800	20	16	4	2	74.7	37.6	1.98	>10	Undercut and angled
3	800	20	32	8	2	58.1	9.1	6.38	>25	Undercut and angled
3	800	20	64	16	2	10.8	14.2	0.76	N/A	Rough and barely etched

Device Etching

The etching recipes were developed on a single crystal silicon wafer. However, the devices need to be fabricated on an SoI. To verify that the developed recipe performs consistently on the ASoI, the same test patterns were made and etched using the base recipe. The results, displayed in Figure 67, verify that the recipe works adequately for ASoI substrates. In addition, the recipe etches silicon much faster than silicon oxide which allows the slight elbow on the sidewall to be etched away without transferring into the bottom oxide layer. The devices written in the EBL were etched utilizing the base etch for the ASoI wafer and the 800W RF_2 and 40sccm flow rate etch for the SoI wafer due to the resist coating thinner on this wafer. Figure 68 is a compilation of SEM pictures comprising of the overall device, a magnified view of the input waveguide, the interface between the input waveguide and the photonic crystal for an ASoI substrate. Also shown is the same interface in a device fabricated on an SoI substrate where the design was modified to place a gap between the end of the input waveguide and the photonic crystal to avoid the bleeding effect of the EBL cutting into the first layer of the photonic crystal, as seen in the case of the ASoI substrate. The magnified view of the input waveguide displays the smoothness of the sidewalls which is critical for low propagation loss in the waveguide region as well as inside the photonic crystal. The SEM images in Figure 68 are of the final device, after the post-etch processes were completed, as those processes were performed immediately after the etching step. The etching processes developed successfully transferred the device patterns into the SoI wafers and showed good sidewall smoothness for both the circles and the larger input and output waveguides.

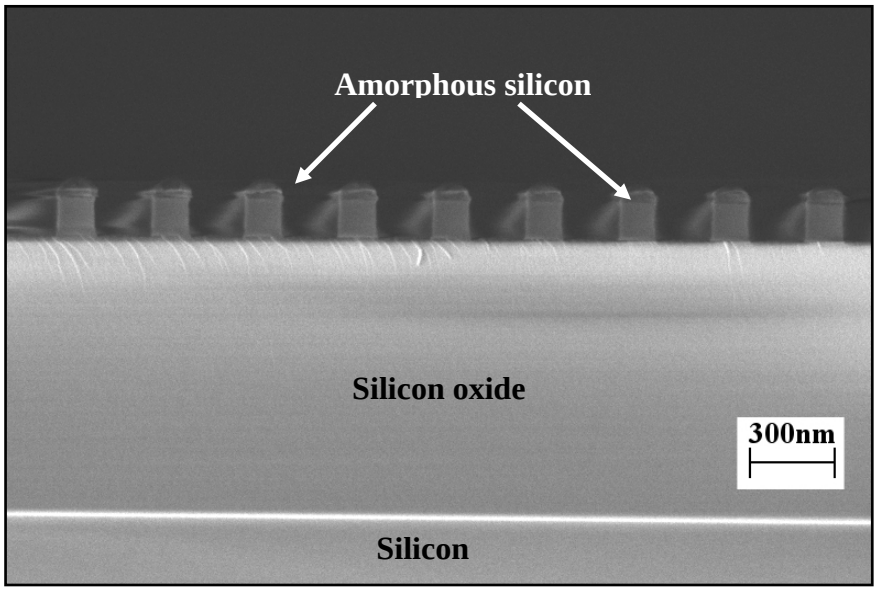

Figure 67. Test etch for verification of recipe consistency for ASoI device fabrication

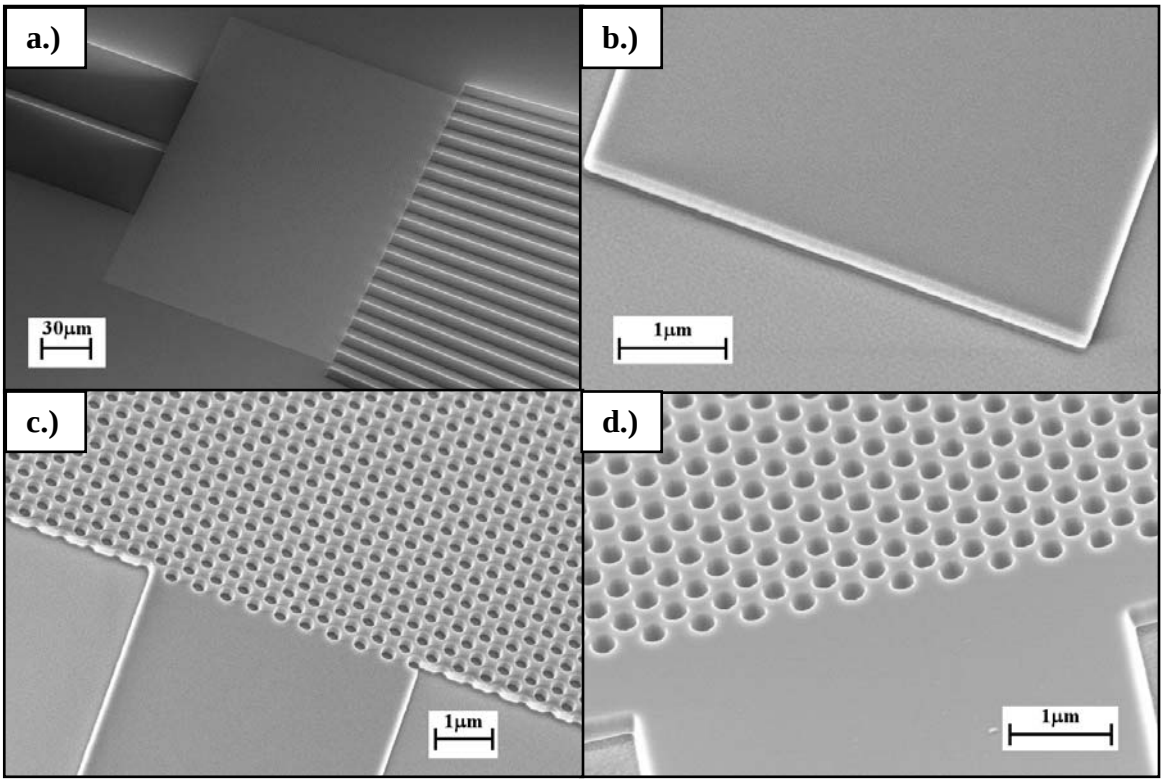

Figure 68. Compilation of SEM pictures of devices etched in ASoI and SoI wafers. a.) Low magnification overall view. b.) Magnified end of input waveguide. c.) Input interface of photonic crystal on ASoI. d.) Input end of photonic crystal on SoI with modified design.

Post-Etch Processing

After etching is complete, the photonic crystal devices still have several critical steps to complete before they can be measured. The first of these steps is the singulation of the device so that the input waveguide is accessible for light to be coupled in by a lens or a fiber. Wet etching of the bottom oxide to create larger index contrast or to completely etch out the bottom oxide to form an air bridge structure can occur either before or after the singulation. The removal of the ZEP-520A resist remaining from the plasma etching and the smoothing of the surface are additional steps which must be completed to finish the fabrication process.

Once the etching was completed, the next step is the singulation. The singulation was conducted at this point in the process since there is still a thin layer of resist left on the sample which protects the surface from the silicon particles produced in the cutting process. For samples with many small devices packed closely together, it is necessary to coat another layer of polymer to protect the devices from this type of contamination. The two methods investigated for cutting the sample were the dicing saw and cleaving with a diamond scribe. Even though the dicing saw gave a straight cut to the naked eye, at higher magnification, the edge of the sample showed chips and cracks on the order of 10 μm as expected due to the blade on the dicing saw having diamond particle sizes of several microns. The second method investigated was to cleave the sample using a diamond scribe. The main drawback of this method is the need to align the pattern exposure to the cleave plane of the single crystal silicon. With the facet on a silicon wafer having an accuracy of only ±5° to the 100 plane, the angular alignment of the cleave plane is uncertain. In addition, the waveguides must be made sufficiently long (>1

mm) for manual cleaving using a diamond scribe. This is detrimental to the repeatability and quantitative measurement of the device as the waveguide length will vary from sample to sample. The quality of the cleave plane was found to be inconsistent, even among the waveguides on the same sample as depicted in Figure 69. However, cleaving produced a significantly higher quality edge than the dicing saw and was the method utilized for singulation. A plasma etch method would be more desirable, but requires an additional mask step and was not investigated.

The second major post-etch processing which was required was to etch the bottom oxide. This step can be conducted either before or after device singulation to produce slightly different input waveguide structure. It was conducted to give a higher index contrast between the silicon device layer and the cladding since it lowers the average index of the bottom oxide in direct contact with the device. An air bridge structure created by etching away all of the bottom oxide is a symmetric structure with the highest index contrast and is closest to the theoretical 2D approximation. Also, even though the silicon was etched very smoothly by the plasma, the oxide develops a rough profile as seen in Figure 70. Since any roughness can be a source of scattering, the buffered oxide

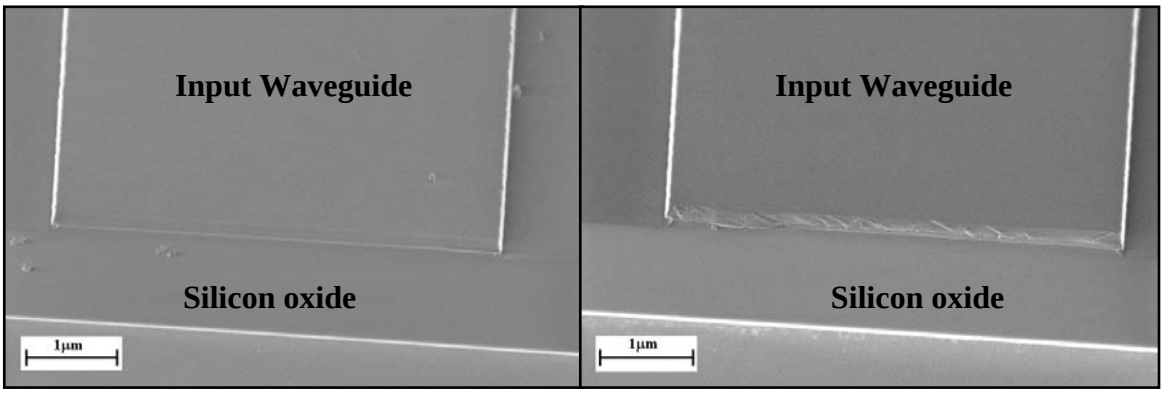

Figure 69. 45° angled view of the edge of a cleaved ASoI sample on two locations of the same sample

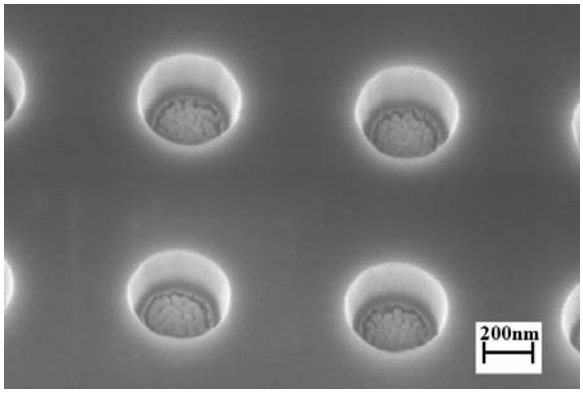

Figure 70. 30° angled view of holes etched in an SoI showing the rough surface of the bottom oxide

Etch (BOE) serves to distance this roughness as far as possible from the high index silicon layer. As an extension to the BOE undercut experiment on the bulk ASoI film, the test patterns for the etch recipe development with the rows of holes were subject to varying lengths of soak times in BOE to test the feasibility of creating an air bridge structure. These samples were already stripped of the resist before the wet etch. As illustrated in Figure 71, 3 minutes of etching resulted in an undercut structure without significantly attacking the ASoI. However, by 20 minutes of etching, significant eroding of the amorphous silicon layer resulted. Unlike crystalline silicon, the amorphous silicon can have local density fluctuations and areas with higher concentrations of oxygen as defects from the

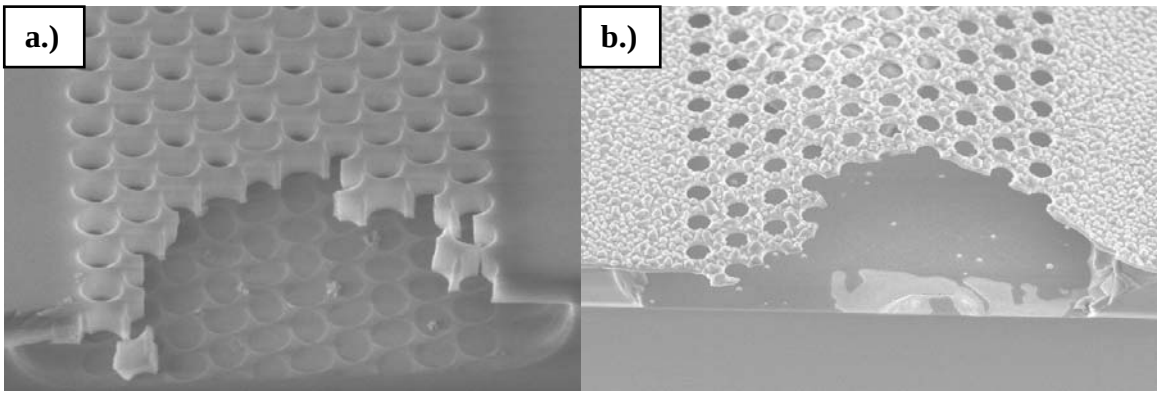

Figure 71. Circular patterns plasma etched into silicon with a.) 3 min. soak in BOE b.) 20min soak in BOE

deposition resulting in etching in a BOE solution. To avoid etching from the top surface, the resist layer on future samples was not removed before the wet etch. For small test patterns, complete undercutting of the structure was possible without sacrificing structural integrity. However, for large structures that were necessary to test bulk propagation effects such as self collimation, complete undercutting resulted in the structure tearing and deforming as shown in Figure 72. Therefore, a short BOE etch with 15~30s duration was performed on the devices to ensure that complete undercutting did not occur. At an etch rate of ~85 nm/min, this condition still undercuts the holes by ~20-50 nm, which is a significant fraction of the hole diameter and periodicity, which are ~200 nm and ~400 nm, respectively, for devices operating in the IR.

Once all of the processing was completed, the ZEP-520A resist left over from the etching must be removed. In addition, any thin film of polymerization left on the sidewall of the silicon layer needs to be removed. Heated oxygen plasma in the Gasonics Aura 1000 Asher stripped both polymers effectively using a 1 minute recipe. One additional step was performed on the devices fabricated. Even though the grown

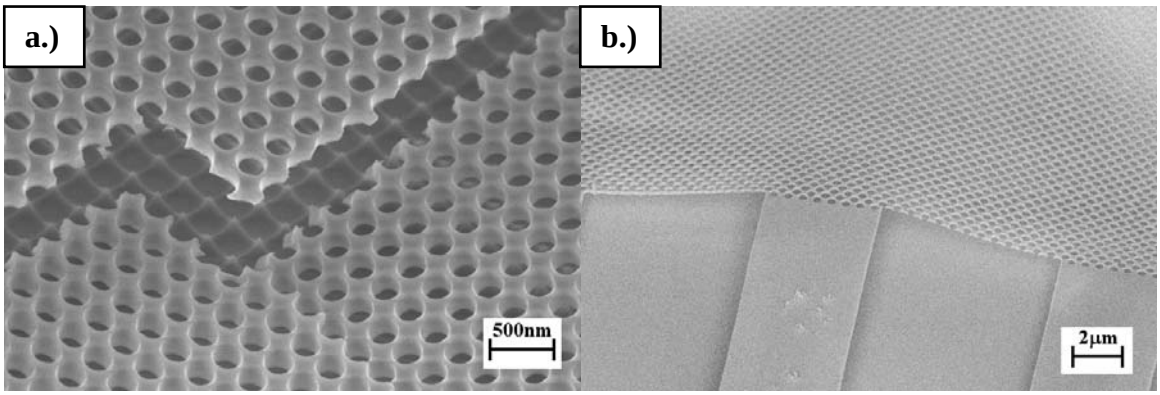

Figure 72. Tearing and deformation of photonic crystals that were completely undercut by BOE etching

amorphous silicon layer exhibited good surface roughness and uniformity, small granules of amorphous silicon was still clearly visible in the SEM image. Surface roughness was also apparent on the purchased SoI wafers. A plasma smoothing step was investigated and performed with a recipe of 15W RF_1, 600W RF_2, 5mTorr process pressure, 28sccm Ar, and 2sccm CF_4. This recipe primarily utilizes argon ions at a low process pressure with highly vertical ion trajectories. The fluorine ions also follow this trajectory giving a highly anisotropic etching with the ability to flatten the nanometer scale roughness of the surface. A 20 nm thick layer was etched off the top surface. An AFM scan shows that the small granular features have been etched away to improve the roughness to an RMS roughness value of 0.32 nm. The patterned area did not show any discernable rounding as shown in the images of the final device in c.) and d.) of Figure 68.

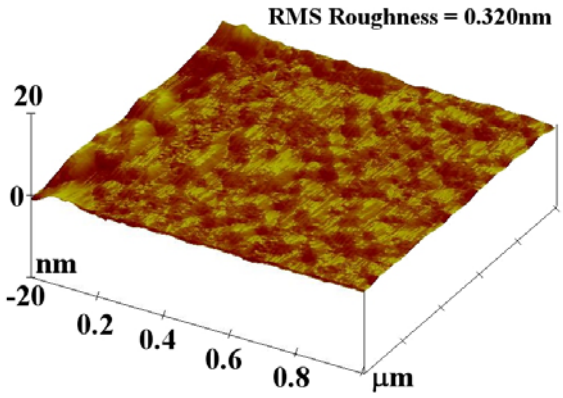

Figure 73. AFM scan of a smoothed ASoI wafer

Discussion

In this chapter, the fabrication procedures for 2D photonic crystals in ASoI and SoI wafers are outlined. Various parameters were optimized for the fabrication. Issues encountered include roughness and thermal stress for the fabrication of the ASoI substrate; proximity effect, stitching error, and exposure time in the EBL system; "grass,"

microtrenching, and sidewall profile in the plasma etching; and structural integrity and roughness in the wet etching and cleaving processes. Processes were developed to overcome these issues and successfully fabricate devices. Thermal oxidation and low temperature growth of amorphous silicon, coupled with a surface smoothing plasma etch, resulted in a low stress, smooth film with adequate surface roughness for the device. A unique etching recipe utilizing Cl_2 and C_4F_6 was developed and optimized to anisotropically etch silicon with the ZEP-520A resist. The measurement of the band structure and verification of the self collimation phenomenon was obtained as described in the next chapter. Future work in the fabrication area lies mainly in the lithography and CAD file design areas. A better understanding of the proximity effect and methods to design structures to correct for it is crucial to avoid a gradient in the hole sizes for the patterns written using the EBL. Also, singulation of the device utilizing lithography and plasma etching will improve the repeatability and consistency for quantitative characterization.

CHAPTER 4

MEASUREMENT OF 2-D PHOTONIC CRYSTAL PROPERTIES

Introduction

Measurement of 2-D photonic crystal properties has attracted extensive attention in the literature[23,34,35,83-85]. Techniques have been developed to measure the band structure properties in transmission and reflection with an off-plane incident beam[83-85]. Also, direct measurement of device functionality, such as filtering and switching, has been performed[16,23]. The measurement methods utilized in this thesis are band structure measurements utilizing specular reflectance[83,84] and direct observation of scattered light from an overhead view of the fabricated device. The measurements were correlated to simulation data generated using 3-D plane wave expansion and finite difference time domain methods.

Band Structure Measurements

The region of the band structure above the light cone, where components of the wave vector can couple to the propagation modes in free space, can be probed utilizing intensity measurements of the reflected beam. A square lattice photonic crystal having a lattice constant of 500 nm was fabricated on an ASoI substrate over a 1 mm by 1 mm square region. The measured dimensions of the photonic crystal were 284 nm average hole diameter, 178 nm thickness of the amorphous silicon, and ~60 nm hole depth in the oxide layer. The diameter and the depth of the hole in the oxide layer were measured in an SEM while the thickness of the amorphous silicon was measured utilizing thin film

interference. The diameters of the holes varied slightly from the edges and corners towards the middle of the square with a maximum deviation of approximately 5%. The smallest holes were observed on the corners of each pattern with the size becoming uniform around 100 μm inside the perimeter of the square. Since over 80% of the pattern showed good uniformity, the average hole size was calculated omitting the outer region exhibiting the smaller size. The effect of this hole size deviation is discussed in the results section. The measurement setup and the principle behind the band structure measurement are described followed by the measurement results and correlation with simulation data.

Principle of Operation

A specular reflection measurement was performed by illuminating the sample with a tungsten-halogen lamp as a broadband light source and recording the spectral distribution of the reflected light with a monochormator selecting the wavelengths entering the InGaAs detector. A schematic of the reflectivity measurement setup is given in Figure 74. An infrared fiber optic cable carried the signal from the lamp into a series of lenses which focused the light onto the sample at a specified incident angle. The light reflected in the incident plane was focused into another fiber which led to a monochromator. The monochromator utilized a grating and a slit to allow only the desired frequency to exit and be incident onto the detector. A scan of the reflectivity with respect to the wavelength was performed by controlling the monochromator with a personal computer. Due to the wavelength dependent intensity of the lamp, absorption in the fiber, and sensitivity of the detector, a reference scan was necessary for normalization.

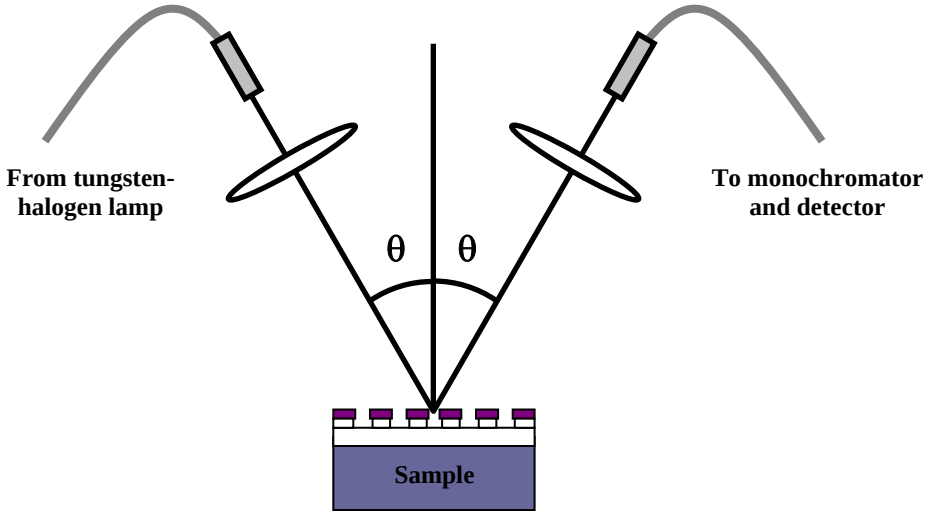

Figure 74. Measurement setup for the reflectivity measurements.

Figure 75 is a reference scan at an incident angle of 15° recorded for an aluminum coated silicon wafer. The scan spanned a wavelength range of 800~1700 nm in 1 nm increments. The steep drop-offs of the signal count at the beginning and end of the scan were due to the decreasing sensitivity of the InGaAs detector. In addition, absorption by O-H bonds from the water content in the IR fiber caused the series of small dips around 1240 nm and the large absorption peak centered at 1380 nm. A reflectivity value was obtained by dividing the raw data counts by the reference data counts taken at each incident angle prior to measurement of the sample.

The band structure of a 2-D photonic crystal can be probed through a series of reflectivity measurements taken at different angles. Transmission of an electromagnetic wave at a boundary occurs through conservation of the tangential component of the wave vector. The tangential component of the wave vector for a specular reflection measurement with respect to the sample surface is given by:

$$\left|\vec{k}_{\text{tangent}}\right| = \frac{\omega}{c}\sin(\theta) \qquad \textbf{Equation 31}$$

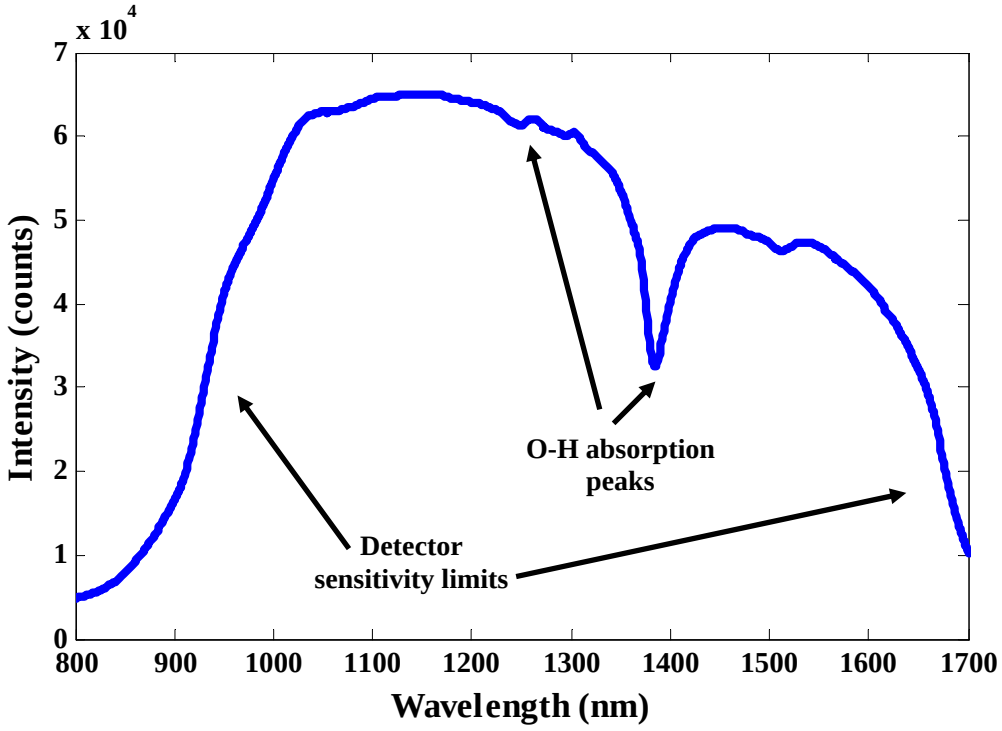

Figure 75. Reference scan for the reflectivity setup showing the effects of O-H bond absorption in the fiber and the detector sensitivity drop off

where ω is the frequency of the incident wave, c is the speed of light, and θ is the incident angle. An index of refraction of 1 for air is assumed in the formula. When this tangential wave vector corresponds to a photonic crystal mode, the incident light can couple into the slab resulting in a dip in the reflectivity curve. This condition is given by the equation:

$$\omega_{n,PC}\left(k_{n,\text{tangent}}\right) = \omega_{n,measurement} = \frac{k_{n,\text{tangent}}}{\sin(\theta)} \qquad \textbf{Equation 32}$$

where the frequencies and wave vectors have been normalized to the photonic crystal lattice parameter as described previously. Two illustrations in Figure 76 show the mechanisms of the coupling. A wave vector surface analysis similar to the one used for refraction, where the tangential component of the wave vector is conserved across an

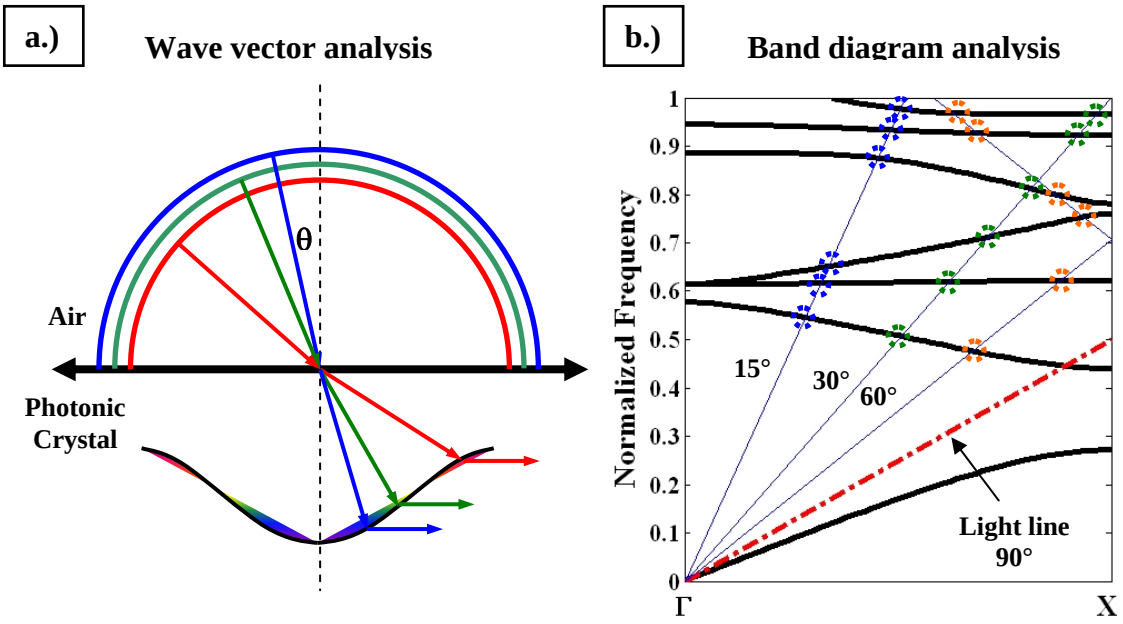

Figure 76. Two graphical illustrations for coupling of out of plane incident radiation into the photonic crystal for analysis of reflectivity data. a.) wave vector analysis b.) band diagram analysis

interface, shows which angle of incident radiation can couple into a photonic crystal mode. The illustration only shows one band, but the analysis needs to be conducted for all of the bands in the frequency range of the measurement. If the frequency of the light is too small, it is possible that the photonic crystal mode is outside of the radius of the wave vector surface in free space. This is the same condition as the light line argument for confinement of photonic crystal modes within the slab layer. Only modes outside the light line can be probed using the reflectivity setup. Scanning the wavelength in the reflectivity measurement corresponds to changing the radius of the semicircles in the air region such that at specific wavelengths, the tangential wave vector crosses the photonic band and light couples into the structure. Changing the angle moves this crossing point allowing the band structure to be probed. The main difference between this analysis and the conventional refraction angle analysis is that for each frequency, the mode in the photonic crystal is a point and not a curve, thus all modes propagate in the plane of the

structure. Even though the graphical representation implies a vertical component of the propagation, the curve drawn is not for a single frequency and can not be utilized to discern the propagation direction. A more powerful method of graphical analysis involves directly superimposing the scanning conditions onto the band diagram. For each angle, the frequency as a function of the tangential component of the wave vector is a straight line. The intersection of these straight lines with the band diagram gives the location of the dips in the reflectivity measurements. Once one of these lines crosses the first Brillouin zone, it can be folded back in the same manner as the bands in the photonic crystal as shown in the 60° case in Figure 76. Since the reflectivity can only measure the band structure outside of the light line, it can not directly measure the first band of the photonic crystal where self-collimation is expected. However, it can be used to directly measure the upper bands and correlate them to the simulation.

Results

The reflectivity measurements were performed in the Γ-X direction of the square lattice photonic crystal. For angles between 15° and 70° in 5° increments, two scans were performed in areas with and without the photonic crystal pattern. The results of the scans are compiled in Figure 77. The area without the photonic crystal displayed a thin film interference pattern as defined by the amorphous silicon, silicon dioxide, and the silicon substrate. The region with the photonic crystal displayed a similar interference pattern along with the absorption dips from the band structure of the photonic crystal. The measured reflectivity dip width ranged from 15~40 nm as opposed to an ideal very narrow frequency dip. This width is attributed to two factors. The first is the non-

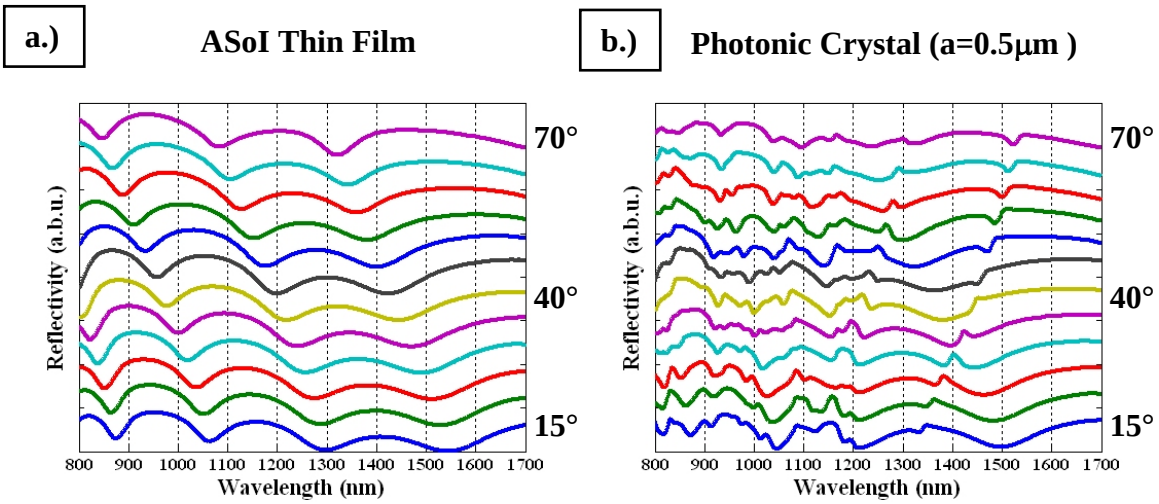

Figure 77. Reflectivity measurements on a.) a thin film region and b.) the photonic crystal region of an ASoI substrate with respect to the incident angle

uniformity in the hole diameter across the sample. The second factor is from the focusing of the incident light onto the sample resulting in a range of k vectors incident on the sample due to the small spot size. The center of the dips were identified by finding the zero values of the first derivative of the data after performing a subtraction of the running average to account for the average tilt of the curve in the vicinity of the dips. A threshold was applied to the magnitude of the first derivative to filter the noise in the data. This method identified the center of the dip while discarding broad peaks like those caused by the thin film interference. Isolated peaks can accurately be identified, but in the region of higher order bands, the curve was too complex and accurate peak identification became difficult. Figure 78a shows the band diagram plotted using the dips identified from the reflectivity measurement, and Figure 78b compares the measurement with theoretical calculations performed utilizing 3D FDTD and PWE simulation methods. The second band was compared to the simulation data which showed excellent fit of the shape of the curve but had a deviation of 5~8% in the frequency. Both simulations showed the band to be lower than the measured data. This indicates that the effective index of the sample

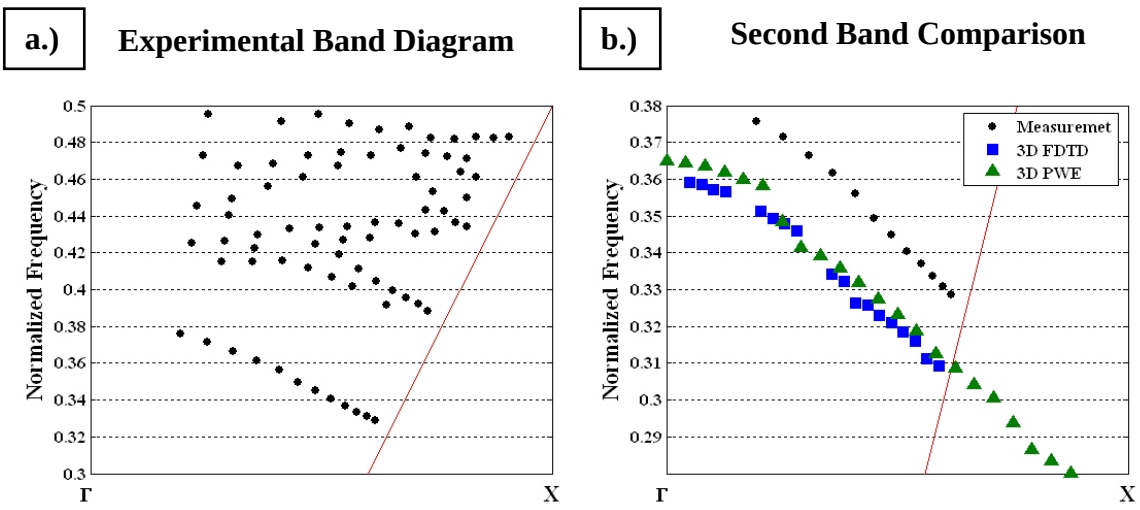

Figure 78. Band diagrams a.) obtained from the reflectivity measurements and b.) compared with simulation for the second band

was lower than the simulated slab. This lower effective index for the sample could result from porosity, impurities in the amorphous silicon, and small crystallites of single crystal silicon lowering the index of the amorphous silicon film. The deviation of the effective index of a slab can also be caused from the error in the measurement of the thickness of the sample. A Nanospec Film Analyzer 3000 was used to measure the thickness of the ASoI film, which is a three layer film comprised from the substrate, oxide layer, and the amorphous silicon layer. The film analyzer must fit the values for the thickness of the oxide layer along with the thickness of the amorphous silicon layer. The interference pattern was more strongly dependent on the thickness of the bottom oxide than the amorphous silicon and a good model fit could not be obtained for the amorphous silicon layer. The model with the best fit was chosen, but different models can result in a difference of the measured thickness by over 25%. Cross sectional measurement in an SEM gave a range of values from 120 nm to 170 nm for the ASoI substrate. Another source of error is the growth of a native oxide. Up to 3 nm of native oxide formed on the

samples prior to the measurement. Since the critical dimensions, such as the thickness and hole sizes are 178 nm and 284 nm respectively, the oxide layer has a significant volume and lowers the effective index of the photonic crystal region as the oxide index (n = 1.45) is much lower than the amorphous silicon (n = 3.73). The effect of other sources of error, such as uncertainty in the amount of undercut in the bottom oxide layer and uncertainty in the exact angle and orientation of the sample towards the incident beam, was small compared to the effect of deviations in the thickness and average index of the device layer. To determine the effect of a change in the latter parameters, an additional 3D FDTD simulation was conducted with the index of refraction and the thickness of the device layer lowered to 3.66 and 156 nm, respectively. The index of 3.66 was calculated by averaging the dielectric constant through the volume of the device layer with a 3 nm thick native oxide. The thickness value was obtained by averaging the values obtained from the SEM cross sections. The simulated data, shown in Figure 79, has excellent agreement with the measurement for the bands located around a normalized frequency of 0.43. The simulation match is worse for the lower bands since the refractive index of

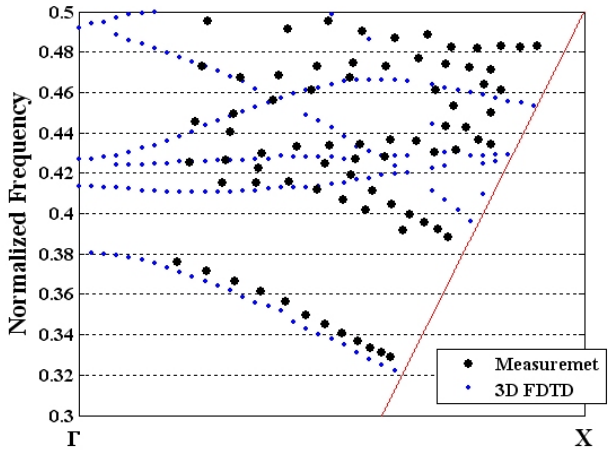

Figure 79. Overlay of the band diagram from the measurement and simulation utilizing values corrected for the thickness and the native oxide

amorphous silicon is a function of wavelength, with values ranging from 3.8 to 3.72 within the wavelength range of the scan. Thus the low bands have a slightly lower index than the value used in the simulation. Also, the reflectivity measurement shows additional bands which are not in the simulation are due to the reflectivity measurement detecting both TE and TM modes. The simulation only contains the TE modes as the TM modes are not confined in the device layer for this thickness of photonic crystal and are lost. The measured photonic crystal displays both excellent qualitative agreement in the shape of the band structure and excellent quantitative agreement after factoring in the variations in the thickness and the average index of refraction.

Self-Collimation Measurements

The self-collimation effect was verified utilizing the device fabricated as shown in Figure 68. The self-collimated beams were observed through a top view image taken with an IR camera. This section describes the design parameters and issues encountered in the fabrication of the device along with a description of the measurement set up and results. The samples exhibiting self-collimation were found to correlate very well with the simulation data.

Design

A schematic of the device designed to observe the self-collimation effect is shown in Figure 80. Due to the difficulty of controlling the spot size for directly focusing light into the photonic crystal, an input waveguide was designed with the desired beam width of 5 μm. The fundamental mode in a slab waveguide exhibits a single lobe in the center

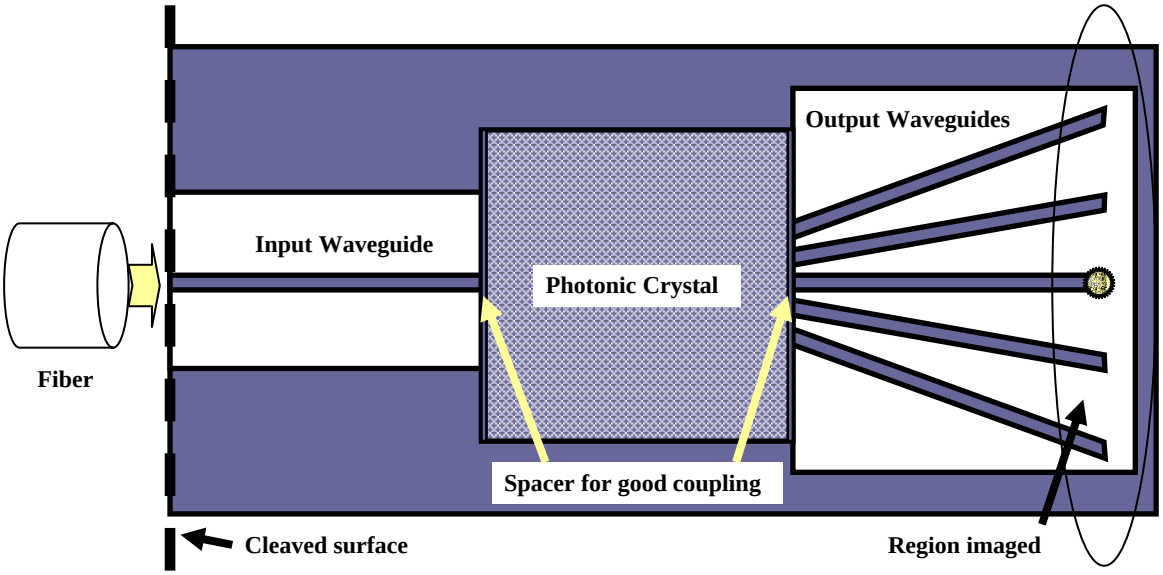

Figure 80. A schematic of the device design for observation of self-collimation.

which qualitatively approximates to a Gaussian beam. A space of 1 μm was placed between the end of the waveguide and the photonic crystal region. This region served to prevent any overexposure from the lithography from reaching the photonic crystal area as illustrated in the first iteration of samples shown in Figure 68c. These regions caused significant scattering of light in the measurement. After propagating through the photonic crystal, the beam spread is observed through coupling into multiple waveguides on the output end of the photonic crystal. For wavelengths exhibiting self-collimation, the intensity is only coupled into the center output waveguide. Samples were fabricated with a photonic crystal propagation length of 150 μm and lattice constants of 282.8, 353.6, and 424.3 nm, respectively. These periodicities were selected since the simulation results indicated that self-collimation on the top of the first band occurs at wavelengths between 3 and 4 times the lattice constant for a structure with air holes in a high index slab. Numerous samples were fabricated with varying EBL doses to obtain samples with a wide range of hole sizes. These samples also exhibited a gradient in the hole size from

the edge of the samples to the center of the sample. However, as discussed in the simulation section, the self-collimation effect is only weakly dependent for structures with a hole in the high index matrix, thus the effect can be observed even with the small amount of variation in the fabricated samples. The output waveguides were 5 μm in width and spacing with a small separation from the photonic crystal. The waveguides were fanned out to 15 μm apart to easily identify the ends using an IR camera. The output waveguide was terminated with a blank space. The light scatters off of the end of the waveguide and can be detected in an overhead view.

Measurement Setup

The measurement setup for the self-collimated beam measurement included infrared laser light sources in the form of a C-band laser (Agility 3105 CW), an L-band laser (Santur TL2010-L), and a 1310 nm laser diode (Thorlabs LPS-1310-FC). A cleaved single mode fiber carried the signals through polarization controlling paddles to the sample. A precision alignment stage with 3 piezoelectricity controlled axes, 2 additional micrometer controlled axes, and 4 manual adjustment axes was utilized for aligning the fiber to the sample and the microscope objective. The stage allowed independent movement of the fiber and sample in addition to focusing of the microscope objective. A Vidicon tube IR camera (Hamamatsu C2741-03) imaged the sample through a 40x microscope objective. The output was recorded on a personal computer utilizing a video capture card. A schematic of the experimental setup is shown in Figure 81.

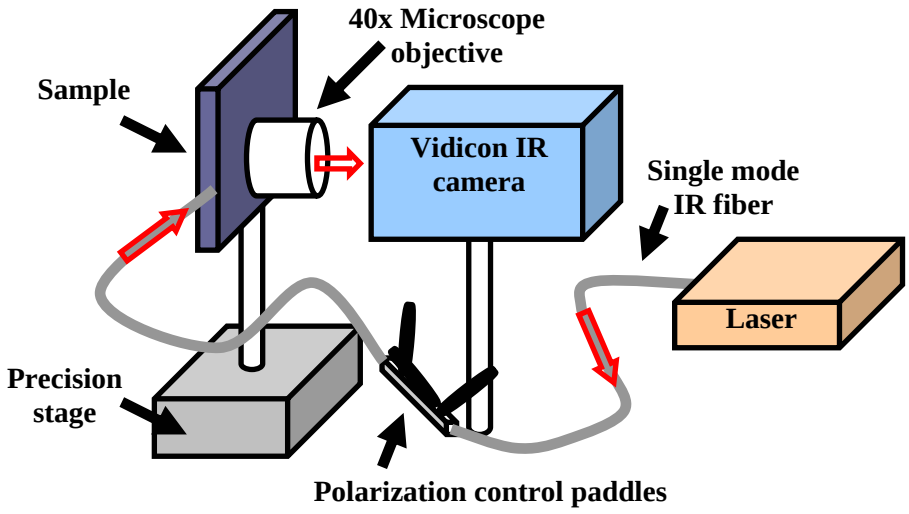

Figure 81. A schematic of the measurement setup for top view imaging of the photonic crystal device

Results

The incident light was directly coupled into the waveguide by bringing the source fiber in proximity to the cleave plane through the input waveguides. Figure 82 shows the images obtained from the IR camera at the various points of interest along the device. In the input plane, the fiber is clearly visible and the region with the input waveguide scatters light that failed to couple into a waveguide mode. Once the light is coupled into the input waveguide, there was no detectable scattering from the sidewalls of the waveguide. The low loss in the waveguides allowed the use of long input and output waveguides so as to isolate the coupling plane, photonic crystal, and the output measurement end from each other By using a single mode fiber and centering the fiber and the waveguide, the fundamental mode of the input waveguide will be the most strongly excited. The coupling of the fundamental mode was confirmed by observing the scattered light at the input plane of the photonic crystal, which displayed a single lobe characteristic. The alignment was obtained by maximizing the intensity of the

transmitted light. The light at the input of the photonic crystal corresponds to the modes of the input slab waveguide. The fundamental mode profile approximates a Gaussian profile with a beam width similar to the width of the waveguide. The beam will propagate and spread inside of the photonic crystal slab following:

$$w^2(z) = w_0^2\left[1+\left(\frac{\lambda_0 z}{\pi n w_0^2}\right)^2\right] \qquad \textbf{Equation 24}$$

Scattering was observed at the input and output ends of the photonic crystal where beam components that do not propagate in the next structure are scattered out of the plane of the device. An outline of the beam propagating through the photonic crystal could not be obtained due to the first band mode residing inside of the light cone and because the high quality of the device precluded roughness on the surface and the sidewalls that could scatter the beam. Even though propagation through the photonic crystal cannot be observed directly, beam spreading can be observed through the scattering at the inputs and outputs of the waveguides. At the input plane of the output waveguides, the air regions between the output waveguide result in scattering at the interface. In addition, components that enter the output waveguide which are not modes of the waveguide structure also scatter along the first 20-30 μm of propagation as seen by the center image of Figure 82. Finally, the ends of the output waveguides give an image free from scattering on the output end of the photonic crystal to measure the number of waveguides the beam spread into. Self-collimation will cause only the center waveguide to capture the incident beam intensity.

Two of the samples exhibited self-collimation. The first sample device was fabricated on a single crystal SoI substrate with measured device dimensions of 228 nm

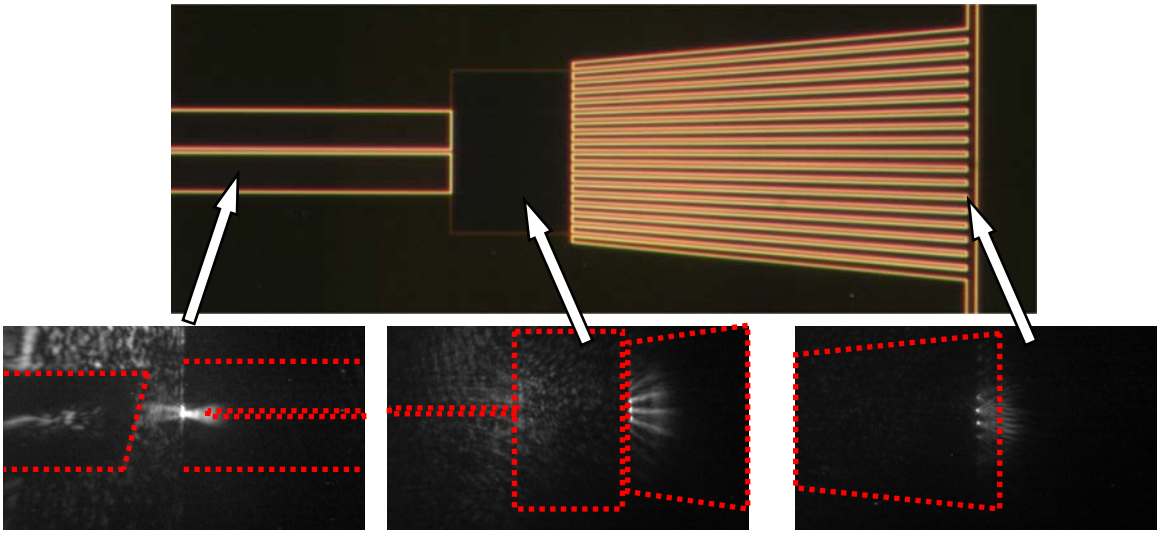

Figure 82. Top view IR images of the various regions of the photonic crystal device

thickness, 220 nm hole diameter, 85 nm hole depth in the bottom oxide, and a lattice parameter of 353.6 nm. The output recorded for this sample, in Figure 83, shows the dramatic effect self-collimation has on the output. In the reference sample, measured at 1560.6 nm, where there was a uniform block of silicon (with no photonic crystal) between the input and output waveguides, the beam spreads and couples into 5~6 output waveguides. For this photonic crystal, all wavelengths between 1528.8 and 1603.8 nm showed a significant concentration of intensity in the center waveguide for the TE mode. The TM mode at 1560.6 nm, displayed for comparison, behaved similarly to the reference. This is expected due to the mode occupying the lower portion of the first band where the behavior is similar to an isotropic material. Figure 84 shows the device with 424.3 nm lattice constant fabricated on the same substrate which revealed the band gap effect. For wavelengths under 1560.6 nm, the TE mode was nearly completely extinguished. For higher wavelengths, the beam spread out further than in free space and

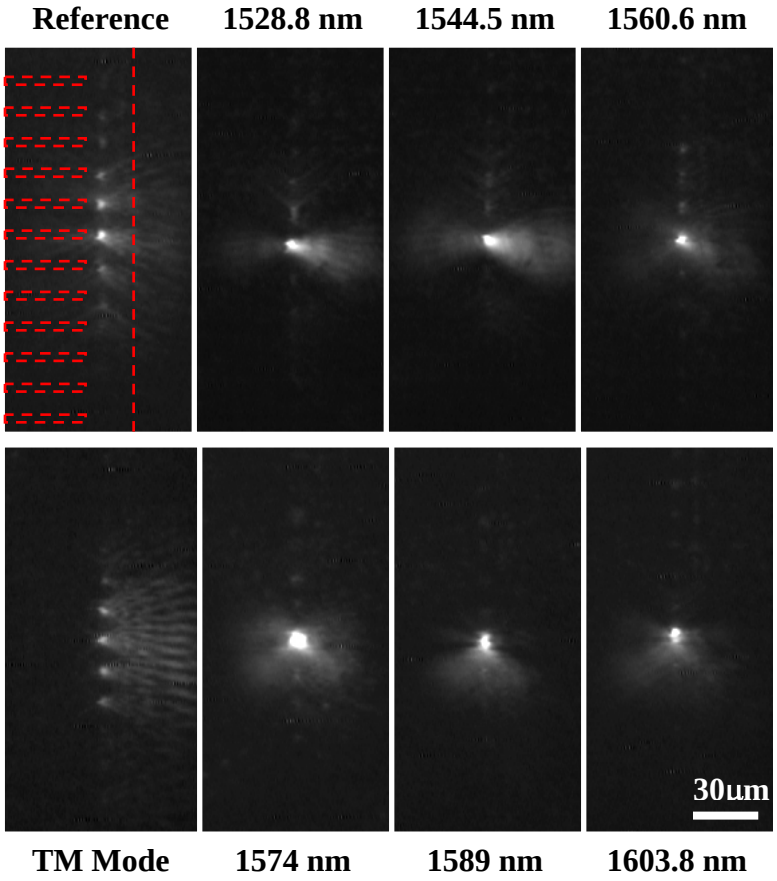

Figure 83. Output region imaged for the single crystal SoI showing self-collimation effect for the TE mode with an empty reference and a TM mode incident for comparison

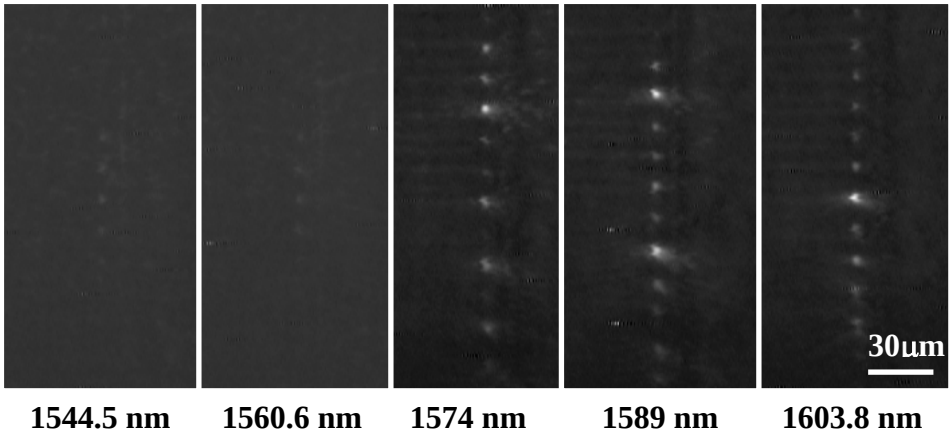

Figure 84. Output region imaged for the single crystal SoI with 424.3 nm lattice parameter showing the band gap and large divergence for wavelengths close to the band gap

showed an erratic fluctuation of the intensity. The large divergence effect is attributed to points near the band gap having a larger curvature in the wave vector contours than in free space and the intensity fluctuation was due to the components of the wave vector that were reflected for being outside of the wave vector contour range. The band diagram for the structure with self-collimation is given in Figure 85. Additional simulations were conducted to calculate the self-collimation point for this device and the location of the band gap for the larger periodicity device at 1550.9 and 1584.6 nm, respectively. The values showed an almost perfect fit to the measurement, where the slight deviation on the band gap boundary can be attributed to similar effects as those discussed in the reflectivity measurements.

The second set of samples that showed self-collimation was fabricated on an ASoI substrate. The dimensions for this sample were a thickness of 174 nm, hole diameter of 340 nm, hole depth in the bottom oxide of 65 nm, and a lattice parameter of 424.3 nm.

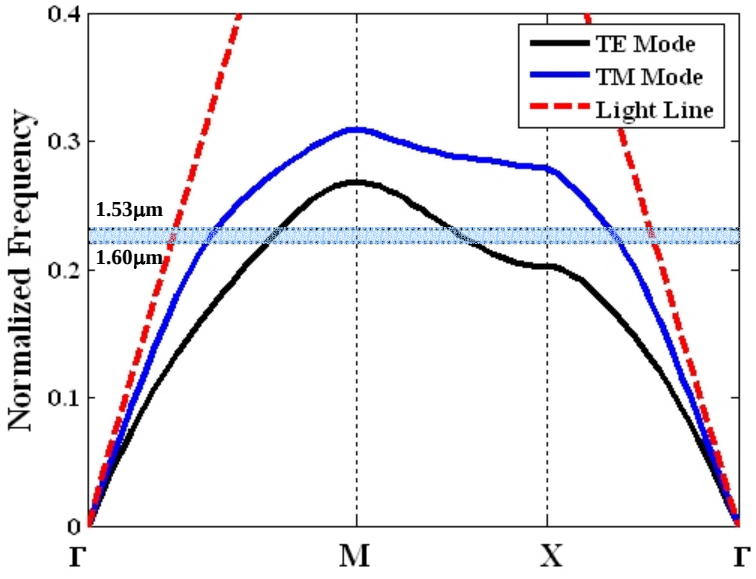

Figure 85. Band diagram of the first band for the TE and TM mode showing the frequency range measured showing the self-collimation effect

For these devices, only the TE mode could be observed. The TM mode could not be coupled into the waveguide since the amorphous silicon film was so thin that the TM mode was below the cutoff, which occurs even for the fundamental mode in an asymmetric slab structure. Figure 86 show a very low light level in the adjacent waveguides compared to devices on the SoI. This observation suggests that the low intensity in the adjacent waveguides for the SoI were from incomplete extinction of the TM mode appearing in the image. Since the ASoI inherently has no TM mode, the frequencies exhibiting self-collimation effect had no noise in the adjacent waveguides. The center wavelength for self-collimation was calculated to be 1629.9 nm for this structure, which is slightly higher than the predicted values, but is well within the tolerance of the measurement. The band diagram for this structure is displayed in Figure 87.

Discussion

The measurements of the photonic band structure in the large area photonic crystal slab, and the observation of the self-collimation and band gap effect in the waveguide device clearly displayed the quality of the fabricated devices and the accuracy of the simulations for modeling photonic crystal applications. The reflectivity measurement gave a strong, smooth signal requiring no amplification, and the waveguide device confined the light within the waveguide and the photonic crystal with no diffuse scattering occurring from surface and sidewall roughness. The waveguide device showed no discernable leakage or scattering, thus overcoming one of the main barriers to creating large area photonic crystal devices. Extensive development of the fabrication process

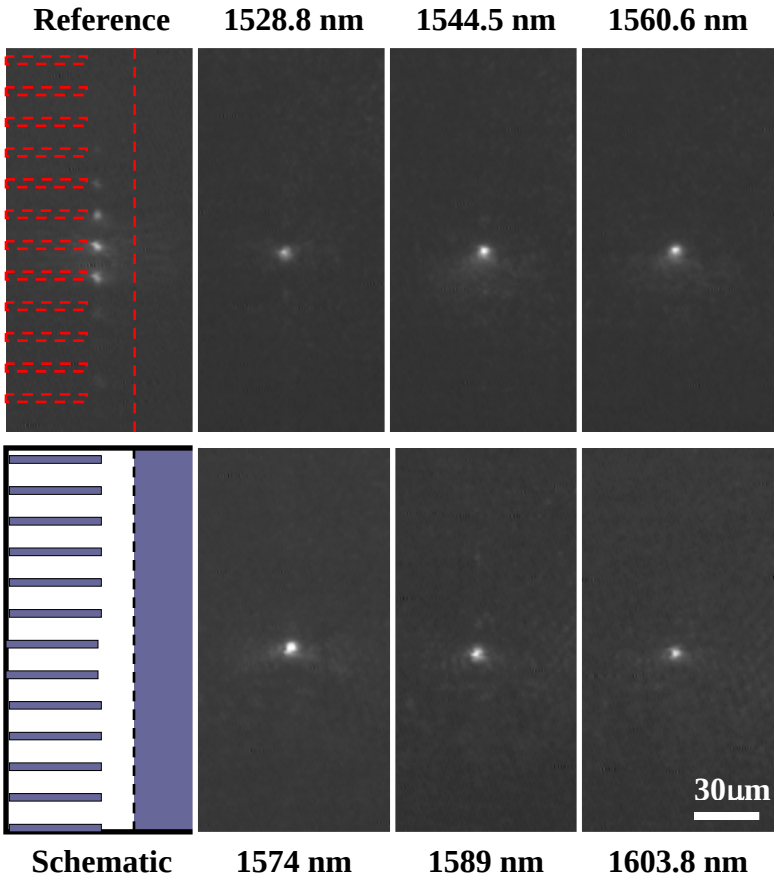

Figure 86. Output region imaged for the ASoI showing self-collimation effect for the TE mode with the reference and a schematic for comparison

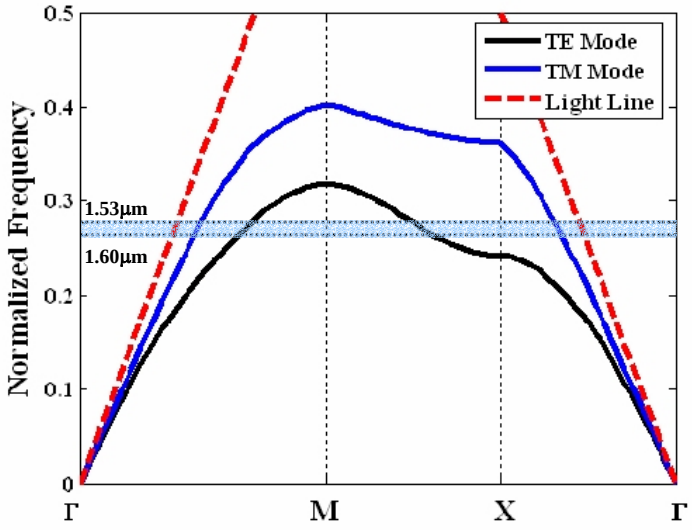

Figure 87. Band diagram for the ASoI sample showing self-collimation effect

and the design of structures with high tolerance to fabrication error were the keys to obtaining measurement values which had excellent agreement with the simulation and modeling results. The validation of the self-collimation effect and the verification of the quality of the fabricated devices open the possibility for more sophisticated devices and measurements. The two measurement techniques investigated in this thesis are the basis necessary for the systematic development of photonic crystal device design and characterization. The ability to directly measure the band diagram through reflectivity measurements allows verification of the band locations to ensure that phenomena observed in the devices are from the intended photonic bands. In addition, direct measurement of the band structure coupled with control of the bands through conformal deposition can tune the photonic bands to adjust for small deviations from theory. The measurement of the waveguide device demonstrates the feasibility of using top view images for the alignment and quality verification. The setup is not suitable for quantitative intensity measurements; however, it provides a definitive visual image for the demonstration of effects such as the self-collimation. Future work in the measurement area includes obtaining the capability of measuring quantitative data from the devices. Issues such as obtaining consistent coupling of the signal into the device and developing reliable referencing methods are two major issues for quantitative characterization. Improvements can also be added in the band structure measurement, such as incorporation of transmission measurements to cover incident angles between 0° and 15° that the reflectivity measurements cannot probe due to physical obstruction in the setup.

CHAPTER 5

CONCLUSION

The research in this thesis has successfully demonstrated the conception, design, fabrication, and measurement of self-collimated beams in two-dimensional square lattice photonic crystals. The relationship between the structural parameters and the optical properties of the photonic crystal was probed.

The theoretical modeling and simulation showed that propagation in a narrow range of frequencies covering the top of the first photonic band in these structures displayed an asymptotic transition in the material properties. A complete effective index model describing the amplitude and phase of a Gaussian beam was developed, analyzed, and verified utilizing the PWE and FDTD simulation methods. A wide range of square lattice structures were investigated for self-collimation properties revealing that self-collimation in the pillar structures is sensitive to both the index contrast and the pillar diameter, while the hole structure is only sensitive to the index contrast. The advantages of each type of structures were considered for the design of the simulated applications and the fabrication of the device. Two applications of self-collimated beams were demonstrated. Sharp 90° turns, non-coupling intersections, tolerance to misalignment and beam size, and broadband operation for an optical interconnect application were leveraged as advantages over traditional index guided waveguides. The ability to confine the beams allowed the extension of concepts and devices developed for free space optics to function at wavelengths on the same size order as the wavelength of light, as demonstrated in the Fabry-Perot interferometer. Photonic crystal Fabry-Perot

interferometers were found to have other benefits, such as a shorter distance necessary to achieve the desired free spectral range due to higher group velocity index of refraction in a photonic crystal.

The fabrication of photonic crystals required the utilization of state of the art electron beam lithography system to pattern the holes in the hundreds of nanometer size range. In addition to optimization of the lithography, a unique etching process utilizing a combination of Cl_2 and C_4F_6 was developed and characterized which displayed a vertical profile with a sidewall angle of under 1° from vertical and exceptionally smooth sidewalls for features as small as 150 nm. This combination of gases was characterized extensively to reveal that the C_4F_6 behaved as an ideal polymerization gas in the chlorine based recipes. The polymerization deposits preferentially on the sidewalls and the resist, but does not significantly deter the chlorine from etching the silicon underneath. The fluorine ions produced from the C_4F_6 is credited with smoothing the bottom and sidewalls as pure chlorine recipes develop roughness. One drawback of the recipe was the tendency for the polymerization to occur on the sidewalls of the chamber causing the gas ratios in the chamber to become more C_4F_6 rich as the etching progressed. This issue was resolved by ramping the concentration and RF power for long etching recipes allowing for anisotropic etching of silicon down to a depth of 1.5 μm with only a 400 nm thick resist layer. The quality of the device layer smoothness was also critical to a well functioning device, thus thermal oxidation, low temperature deposition, and a plasma smoothing step were utilized to achieve a RMS roughness of under 0.5 nm which was 3 orders of magnitude smaller than the wavelength of light in the photonic crystal, thus minimizing scattering.

The meticulous optimization of the fabrication process was the key to the success of the measurements. The reflectivity measurements gave strong, noise free signals which were utilized to plot the band structure with excellent match to the theory. The quality of the signal and the successful correlation with theory reveals the quality of the fabrication and the reliability of the simulation methods. A 150 μm long photonic crystal slab was utilized for verification of the self-collimation. The smooth sidewall of the etching was the key enabler in suppressing scattering losses from the roughness on both the photonic crystal and the input and output waveguides. The waveguide structure tested showed self-collimation and band gap effects within the range of frequencies predicted by the simulation.

The correlation of the simulation and experiment reveals the unique position photonic crystal research occupies, where the simulation techniques and the computing power are mature enough to provide accurate prediction of the effects which can be reproduced faithfully in the experiment. By operating in a region where the materials can be approximated by lossless media with a constant, or slowly varying, dielectric constant, the simulation can accurately account for all the properties of the device. Rarely, does such a combination of simplicity in the system combine with the elegance, functionality, and potential of periodic structures to create a field where fundamental studies and knowledge leads directly to a plethora of novel applications. The photonic crystal field has borrowed numerous concepts from physics, optics, and electromagnetism while reaping the rewards of the microelectronics industry in the tremendous growth of computing power and the technology to fabricate nanometer scale devices. The field has begun to position itself to give back to these areas, as fundamental experiments made

feasible by utilizing photonic crystals, can test and probe theories on the behavior of complex periodic structures. Also photonic crystal devices are being invented to augment and compliment the gamut of devices available in the technology sector. Photonic crystals provide both the scientific and engineering communities with limitless possibilities.

Within the content of the previous chapters, this thesis aims to lay the foundations for the components involved in photonic crystal research. The detailed methodology presented for each simulation method, fabrication equipment, and measurement technique stressed not only the basic principles of operation, but also the practical issues encountered in the use and development of each process. The primary goal of developing a model, characterizing the system, fabricating the device, and measuring its properties has been accomplished culminating in this thesis. It is the author's sincere desire that the work presented in this thesis will aid the future researchers and engineers tackling the rigorous endeavor of understanding the periodic world around us or the challenges of fabricating something so small that it cannot be seen without an electron microscope. The research conducted for this thesis is merely a small step for the scientific and engineering community to climb. This thesis concludes with the hope that the step created here will prove to be a sturdy foundation and one well traveled.

APPENDIX A

M-File: initTM2.m

```
function [G,Wavematrix]=initTM2(InvEpsi,n,g1,g2)
% Function: [G,Wavematrix]=initTM2(InvEpsi,n,g1,g2)
%
% This function performs the 2-dimensional fourier transform on the
%   InvEpsi matrix and then takes the n x n center terms and pads
%   the terms with (n-1)/2 zero's on each side of the matrix.
%   It also creates the G vector needed for the eigen value
%   calculations as well as the Wavematrix which is the matrix with
%   everything other than the k vector information for the eigen value
%   calculation.
%
% This function requires the following variables:
%
%    InvEpsi(d,d) = A square matrix of the inverse dielectric values
%    n = Number of Fourier coefficients (odd recommended)
%    g1 = primitive lattice vector 1
%    g2 = primitive lattice vector 2
%
% This function returns the following variables:
%
%   Wavematrix(n^2,n^2) = Wavematrix of values taken from Kappa
%   G(n^2) = G values from g1,g2 used for band diagram calculations
%
%


% Declare default values
if ismember('g1',who) == 0
    g1 = [1,0];
end
if ismember('g2',who) == 0
    g2 = [0,1];
end

d = size(InvEpsi);
AreaCell = norm(cross([g1,0],[g2,0]));
Kappa = fft2(InvEpsi);
Kappa = fftshift(Kappa)/(d(1))^2/AreaCell;
if mod(n,2)==1
    tempK = zeros(2*n-1);
    tempK(n/2+.5:3*n/2-.5,n/2+.5:3*n/2-.5)=Kappa(d/2-
n/2+1.5:d/2+n/2+.5,d/2-n/2+1.5:d/2+n/2+.5);
    Kappa = tempK;
else
    tempK = zeros(2*n);
    tempK(n/2:3*n/2-1,n/2:3*n/2-1)=Kappa(d/2-n/2+1:d/2+n/2,d/2-
n/2+1:d/2+n/2);
    Kappa = tempK;
end
```

```
n = size(Kappa);
n = floor((n(1)+1)/2);

%Create b vectors
b1 = cross([g2,0],[0 0 1])/(dot([g1,0],cross([g2,0],[0 0 1])));
b2 = cross([0 0 1],[g1 0])/(dot([g1,0],cross([g2,0],[0 0 1])));

% Process to create G function
tempvec = n:-1:1;
tempvec = tempvec-ceil(n/2);
tempvec = tempvec.*(b1(1)+b1(2)*i);
tempmatrix = rot90(tempvec(ones(1,n),:),3);
tempvec = n:-1:1;
tempvec = tempvec-ceil(n/2);
tempvec = tempvec.*(b2(1)+b2(2)*i);
tempmatrix = tempmatrix + tempvec(ones(1,n),:);
G = rot90(tempmatrix(:));

%Creates the Wavematrix
for c = 1:n
    for c2 = 1:n
        tempmatrix = Kappa(c2:c2+n-1 , c:c+n-1);
        Wavematrix(n^2-((c-1)*n+c2)+1,:)= rot90(tempmatrix(:));
    end
end
```

M-File: solveTM2.m

```
function [sol]=solveTE2(Wavematrix,G,Kpoint,band)
% Function: [sol]=solveTE2(Wavematrix,G,Kpoint,band)
%
% This function runs the solver for the TE case of the 2D photonic
crystals
%
% This function requires the following variables
%
%   Wavematrix(n^2,n^2) = Values of the fourier coefficient for solving
%   G(1,n^2) = lattice variables used for band calculations
%   Kpoint = Value of k point to solve for the band
%   band = Number of bands to solve for (default = 6)
%
% This script will return the following variable:
%
%   sol = The lowest "band" number of solutions at the Kpoint
%



n = size(Wavematrix);
n = sqrt(n(1));

opts.disp=0;
Efactor = (abs(G+Kpoint)).^2;
waveE=Wavematrix.*Efactor(ones(1,n^2),:);
sol=rot90(eigs(sparse(waveE),band,0.00000000001,opts));
sol = sort(sqrt(abs(sol)));
```

APPENDIX B

M-file script: PREP_A.m

```
%   This SCRIPT prepares the PML and other constants necessary to
%       perform the 2D FDTD with PML in both X and Y directions. This
%       script prepares for the TE mode (Ez, Hx, Hy). This script
%       creates the variable parameters for the PML.
%
%       (This type is useful for simulating devices)
%
%   This script requires the following inputs:
%
%       EPSIZ(A,B) = Inverse of the dielectric constant for EZ
%       DX = spacing parameter in both X,Y
%
%   Options for this script are the following:
%
%       PMLS = PML size (default 10)
%       PMLM = PML order (default 4)
%
%   This SCRIPT will create all the necessary variables to directly
%   perform the FDTD code used by the function "A2DE" and "A2DES".
%   This is only for the TE (EZ,HX,HY) case. All unnecessary
%   variables will be cleared so be careful not to use a variable name
%   that is cleared at the end of this script.
%
%



E0 = 1e7/4/pi/(2.997925e8)^2;
U0 = 4e-7*pi;
C = 2.997925e8;
DT=DX/C/sqrt(2);
EPSIZ=EPSIZ./E0;
S=size(EPSIZ);

if ismember('PMLS',who)==0
    PMLS=10; % Default PML size
end
if ismember('PMLM',who)==0
    PMLM=4;  % Default PML order
end
if ismember('SMFACTOR',who)==0
    SMFACTOR=1;
end
SMAX =  (PMLM+1)*.8/sqrt(U0/E0)/DX*SMFACTOR;
DC2=DT/DX;


SV1 = [1-1/PMLS:-1/PMLS:1/PMLS].^PMLM.*SMAX;
SV1=[SV1,fliplr(SV1)];
SV2 = [1-1/PMLS/2:-1/PMLS:1/PMLS/2].^PMLM.*SMAX;
```

```
SV2=[SV2,fliplr(SV2)];

% Define PML values for EZ
ST=SV1(ones(S(1),1),:);
EC1 = [S(1)+1:S(1)*PMLS,(S(2)-(PMLS-1))*S(1)+1:S(1)*S(2)]';

% % TEMP
% ST(:)=ST(:).*(EPSIZ(EC1)*E0);
% % TEMP
EZY1=zeros(S(1),2*PMLS-2);
EZY2=zeros(S(1),2*PMLS-2);
EZY1(:)=(2*E0-ST(:)*DT)./(2*E0+ST(:)*DT);
EZY2(:)=2./(2*E0+ST(:)*DT).*(EPSIZ(EC1)*E0);
EZY1=EZY1(2:end,:);
EZY2=EZY2(2:end,:);
EZY2=EZY2.*DC2;

ST=SV1(ones(S(2),1),:);
DZX1=zeros(S(2),2*PMLS-2);
DZX2=zeros(S(2),2*PMLS-2);
DC1 = [S(2)+1:S(2)*PMLS,(S(1)-(PMLS-1))*S(2)+1:S(2)*S(1)]';
EPZT=EPSIZ.';
% % TEMP
% ST(:)=ST(:).*(EPZT(DC1)*E0);
% % TEMP
DZX1(:) = (2*E0-ST(:)*DT)./(2*E0+ST(:)*DT);
DZX2(:) =(2*E0.*DC2)./(2*E0+ST(:)*DT);
DZX1=DZX1.';
DZX2=DZX2.';
DZX1=DZX1(:,2:end);
DZX2=DZX2(:,2:end);
DZX2(:,1:PMLS-1)=DZX2(:,1:PMLS-1)./DC2;
DZX2(:,end-PMLS+2:end)=DZX2(:,end-PMLS+2:end)./DC2;

% Define PML values for HX
ST2=SV2(ones(S(1),1),:);
BC1 = [1:S(1)*PMLS,(S(2)-PMLS)*S(1)+1:S(1)*S(2)]';
BXY1=zeros(S(1),2*PMLS);
BXY2=zeros(S(1),2*PMLS);
BXY1(:) = (2*E0-ST2(:)*DT)./(2*E0+ST2(:)*DT);
BXY2(:) =(2*E0*DT)./(2*E0+ST2(:)*DT)./DX;
BXY1=BXY1(2:end,:);
BXY2=BXY2(2:end,:);

ST=SV1(ones(S(2),1),:);
HC1 = [S(2)+1:S(2)*PMLS,(S(1)-(PMLS-1))*S(2)+1:S(2)*S(1)]';
HXX1=zeros(S(2),2*PMLS-2);
HXX2=zeros(S(2),2*PMLS-2);
HXX1(:)=(1+ST(:)./E0./2.*DT)/U0;
HXX2(:)=(1-ST(:)./E0./2.*DT)/U0;
HXX1=HXX1.';
HXX2=HXX2.';

% Define PML values for HY
```

```
EC1=[S(1)+1:S(1)*PMLS,(S(2)-(PMLS-1))*S(1)+1:S(1)*S(2)]';
EC2=[1:S(2)*PMLS,(S(1)-PMLS)*S(2)+1:S(1)*S(2)]';
ST=SV1(ones(S(1),1),:);
ST2=SV2(ones(S(2),1),:);

HYX1=zeros(S(2),2*PMLS);
HYX1(:)=(2*E0-ST2(:)*DT)./(2*E0+ST2(:)*DT);
HYX1=HYX1(2:end,:).';

HYX2=zeros(S(2),2*PMLS);
HYX2(:)=2*E0./(2*E0+ST2(:)*DT)./U0;
HYX2=HYX2(2:end,:).';
HYX2=HYX2.*DC2;

HYY1=zeros(S(1),2*PMLS-2);
HYY1(:)=(2*E0+ST(:)*DT)./(2*E0.*U0);
HYY1(1:PMLS,1:PMLS-1)=HYY1(1:PMLS,1:PMLS-1).*HYX2(1:PMLS,1:PMLS-
1).*U0./DC2;
HYY1(end-PMLS+1:end,1:PMLS-1)=HYY1(end-PMLS+1:end,1:PMLS-
1).*HYX2(PMLS+1:end,1:PMLS-1).*U0./DC2;
HYY1(1:PMLS,PMLS:2*PMLS-2)=HYY1(1:PMLS,PMLS:2*PMLS-2).*HYX2(1:PMLS,end-
PMLS+2:end).*U0./DC2;
HYY1(end-PMLS+1:end,PMLS:2*PMLS-2)=HYY1(end-PMLS+1:end,PMLS:2*PMLS-
2).*HYX2(PMLS+1:end,end-PMLS+2:end).*U0./DC2;

HYY2=zeros(S(1),2*PMLS-2);
HYY2(:)=(2*E0-ST(:)*DT)./(2*E0.*U0);
HYY2(1:PMLS,1:PMLS-1)=HYY2(1:PMLS,1:PMLS-1).*HYX2(1:PMLS,1:PMLS-
1).*U0./DC2;
HYY2(end-PMLS+1:end,1:PMLS-1)=HYY2(end-PMLS+1:end,1:PMLS-
1).*HYX2(PMLS+1:end,1:PMLS-1).*U0./DC2;
HYY2(1:PMLS,PMLS:2*PMLS-2)=HYY2(1:PMLS,PMLS:2*PMLS-2).*HYX2(1:PMLS,end-
PMLS+2:end).*U0./DC2;
HYY2(end-PMLS+1:end,PMLS:2*PMLS-2)=HYY2(end-PMLS+1:end,PMLS:2*PMLS-
2).*HYX2(PMLS+1:end,end-PMLS+2:end).*U0./DC2;

HYX2=HYX2(:,PMLS:end-PMLS+1);

clear DC1 EC1 EC2 BC1 EPXT EPYT EPZT HC1 PMLM SMAX SMFACTOR ST ST2 SV1
SV2;


HC2 = DC2/U0;

if(ismember('SIGMAZ',who))==0
    SIGMAZ=0;
end

if max(max(SIGMAZ))==0
    EZ2 = EPSIZ(2:end,PMLS+1:end-PMLS+1);
    EZ2(PMLS:end-PMLS+1,:)=EZ2(PMLS:end-PMLS+1,:).*DC2;
else
    EZ1=(1-SIGMAZ(PMLS+1:end-PMLS+1,PMLS+1:end-
PMLS+1)*DT.*EPSIZ(PMLS+1:end-PMLS+1,PMLS+1:end-
```

```
PMLS+1)./2)./(1+SIGMAZ(PMLS+1:end-PMLS+1,PMLS+1:end-
PMLS+1)*DT.*EPSIZ(PMLS+1:end-PMLS+1,PMLS+1:end-PMLS+1)./2);
    EZ2   =   EPSIZ(2:end,PMLS+1:end-PMLS+1)./(1+SIGMAZ(2:end,PMLS+1:end-
PMLS+1).*DT./2.*EPSIZ(2:end,PMLS+1:end-PMLS+1));
    EZ2(PMLS:end-PMLS+1,:)=EZ2(PMLS:end-PMLS+1,:).*DC2;
end

clear SIGMAZ EPSIZ EPSIY EPSIX E0;
EZ=zeros(S(1),S(2));
HX=zeros(S(1),S(2));
HY=zeros(S(1),S(2));
BXY=zeros(S(1)+1-2*PMLS,2*PMLS);
BX=zeros(2*PMLS-2,S(2));
BY=zeros(S(1),2*PMLS-2);
DZ=zeros(2*PMLS-2,S(2)-1);

clear S;
pack;
```

Mex-file: a2de.c

```
#include "mex.h"

void   ezfdtd(double   *EZ,double   *HY,double   *HX,double   *DZ,double
*EZ2,double *EZY1,double *EZY2,double *DZX1,double *DZX2,int PMLS, int
m, int n)
{
  int i,j,pmls,mm1=m-1,grids=m-2*(PMLS)+1,gridn=n-2*PMLS+1;
  double TEMP;

    EZ+=m;
    HY+=m;
    HX+=m;
    for(pmls=1;pmls<PMLS;pmls++)
    {
        EZ++;HY++;HX++;
        for(j=1;j<PMLS;j++)
        {
            TEMP=*DZ * *DZX1+*DZX2* ((*HY-*(HY-1))-(*HX-*(HX-m)));
            *EZ=*EZ * *EZY1 + *EZY2*(TEMP-*DZ);
            *DZ=TEMP;
            HX++;HY++;EZ++;DZ++;DZX1++;DZX2++;EZY1++;EZY2++;
        }

        for(j=0;j<grids;j++)
        {
            *EZ=*EZY1* *EZ+*EZY2*
                ((*HY-*(HY-1))-(*HX-*(HX-m)));
            EZ++;EZY1++;EZY2++;HY++;HX++;
        }

        for(j=1;j<PMLS;j++)
        {
            TEMP=*DZ * *DZX1+*DZX2* ((*HY-*(HY-1))-(*HX-*(HX-m)));
            *EZ=*EZ * *EZY1 + *EZY2*(TEMP-*DZ);
            *DZ=TEMP;
            HX++;HY++;EZ++;DZ++;DZX1++;DZX2++;EZY1++;EZY2++;
        }
    }
    for(i=0;i<gridn;i++)
    {
        EZ++;HX++;HY++;
        for(j=1;j<PMLS;j++)
        {
            TEMP=*DZ * *DZX1+*DZX2* ((*HY-*(HY-1))-(*HX-*(HX-m)));
            *EZ += *EZ2*(TEMP-*DZ);
            *DZ=TEMP;
            HX++;HY++;EZ++;DZ++;DZX1++;DZX2++;EZ2++;
        }

        for(j=0;j<grids;j++)
        {
            *EZ+=*EZ2*((*HY-*(HY-1))-(*HX-*(HX-m)));
```

```
            EZ++;EZ2++;HY++;HX++;
        }

        for(j=1;j<PMLS;j++)
        {
            TEMP=*DZ * *DZX1+*DZX2* ((*HY-*(HY-1))-(*HX-*(HX-m)));
            *EZ += *EZ2*(TEMP-*DZ);
            *DZ=TEMP;
            HX++;HY++;EZ++;DZ++;DZX1++;DZX2++;EZ2++;
        }

    }
    for(pmls=1;pmls<PMLS;pmls++)
    {
        EZ++;HX++;HY++;
        for(j=1;j<PMLS;j++)
        {
            TEMP=*DZ * *DZX1+*DZX2* ((*HY-*(HY-1))-(*HX-*(HX-m)));
            *EZ=*EZ * *EZY1 + *EZY2*(TEMP-*DZ);
            *DZ=TEMP;
            HX++;HY++;EZ++;DZ++;DZX1++;DZX2++;EZY1++;EZY2++;
        }

        for(j=0;j<grids;j++)
        {
            *EZ=*EZY1* *EZ+*EZY2*
                ((*HY-*(HY-1))-(*HX-*(HX-m)));
            EZ++;EZY1++;EZY2++;HY++;HX++;
        }

        for(j=1;j<PMLS;j++)
        {
            TEMP=*DZ * *DZX1+*DZX2* ((*HY-*(HY-1))-(*HX-*(HX-m)));
            *EZ=*EZ * *EZY1 + *EZY2*(TEMP-*DZ);
            *DZ=TEMP;
            HX++;HY++;EZ++;DZ++;DZX1++;DZX2++;EZY1++;EZY2++;
        }
    }
}

void   hxfdtd(double   *EZ,double   *HX,double   *BX,double   *BXY,double
*BXY1,double  *BXY2,double  *HXX1,double  *HXX2,double  BC2,double  HC1,
double U0,int PMLS, int m, int n)
{
  int i,j,pmls,grids=m-2*PMLS+1,gridn=n-PMLS;
  double TBX;

    for(pmls=0;pmls<PMLS;pmls++)
    {
        EZ++;
        HX++;
        for(j=1;j<PMLS;j++)
        {
            TBX = *BXY1* *BX+*BXY2*(*EZ-*(EZ+m));
            *HX+= (*HXX1*TBX- *HXX2* *BX);
            *BX=TBX;
```

```
        BX++;EZ++;HX++;HXX1++;HXX2++;BXY1++;BXY2++;
    }

    for(j=0;j<grids;j++)
    {
        TBX = *BXY1* *BXY+*BXY2*(*EZ-*(EZ+m));
        *HX+=(TBX- *BXY)/U0;
        *BXY=TBX;
        BXY++;EZ++;HX++;BXY1++;BXY2++;
    }

    for(j=1;j<PMLS;j++)
    {
        TBX = *BXY1* *BX+*BXY2*(*EZ-*(EZ+m));
        *HX+= (*HXX1*TBX- *HXX2* *BX);
        *BX=TBX;
        BX++;EZ++;HX++;HXX1++;HXX2++;BXY1++;BXY2++;
    }
}
for(i=PMLS;i<gridn;i++)
{
    EZ++;
    HX++;
    for(j=1;j<PMLS;j++)
    {
        TBX = *BX+BC2*(*EZ-*(EZ+m));
        *HX+= (*HXX1*TBX- *HXX2* *BX);
        *BX=TBX;
        BX++;EZ++;HX++;HXX1++;HXX2++;
    }

    for(j=0;j<grids;j++)
    {
        *HX+=HC1*(*EZ-*(EZ+m));
        HX++;EZ++;
    }

    for(j=1;j<PMLS;j++)
    {
        TBX = *BX+BC2*(*EZ-*(EZ+m));
        *HX+= (*HXX1*TBX- *HXX2* *BX);
        *BX=TBX;
        BX++;EZ++;HX++;HXX1++;HXX2++;
    }
}
for(pmls=1;pmls<PMLS;pmls++)
{
    EZ++;
    HX++;
    for(j=1;j<PMLS;j++)
    {
        TBX = *BXY1* *BX+*BXY2*(*EZ-*(EZ+m));
        *HX+= (*HXX1*TBX- *HXX2* *BX);
        *BX=TBX;
        BX++;EZ++;HX++;HXX1++;HXX2++;BXY1++;BXY2++;
    }
```

```
        for(j=0;j<grids;j++)
        {
            TBX = *BXY1* *BXY+*BXY2*(*EZ-*(EZ+m));
            *HX+=(TBX- *BXY)/U0;
            *BXY=TBX;
            BXY1++;BXY2++;EZ++;HX++;BXY++;
        }

        for(j=1;j<PMLS;j++)
        {
            TBX = *BXY1* *BX+*BXY2*(*EZ-*(EZ+m));
            *HX+= (*HXX1*TBX- *HXX2* *BX);
            *BX=TBX;
            BX++;EZ++;HX++;HXX1++;HXX2++;BXY1++;BXY2++;
        }
    }
    EZ++;
    HX++;

    for(j=1;j<PMLS;j++)
    {
        TBX = *BXY1* *BX+*BXY2*(*EZ);
        *HX+= (*HXX1*TBX- *HXX2* *BX);
        *BX=TBX;
        BX++;EZ++;HX++;HXX1++;HXX2++;BXY1++;BXY2++;
    }

    for(j=0;j<grids;j++)
    {
        TBX = *BXY1* *BXY+*BXY2* *EZ;
        *HX+=(TBX- *BXY)/U0;
        *BXY=TBX;
        BXY1++;BXY2++;BXY++;EZ++;HX++;
    }

    for(j=1;j<PMLS;j++)
    {
        TBX = *BXY1* *BX+*BXY2*(*EZ);
        *HX+= (*HXX1*TBX- *HXX2* *BX);
        *BX=TBX;
        BX++;EZ++;HX++;HXX1++;HXX2++;BXY1++;BXY2++;
    }
}

void hyfdtd(double *EZ, double *HY, double *BY, double *HYY1,double
*HYY2,double *HYX1,double *HYX2,double HC2, double BC2,int PMLS, int m,
int n)
{
  int i,j,pmls,grids=m-2*PMLS,gridn=n-2*PMLS+1;
  double TBY;

    EZ+=m;
    HY+=m;
    for(pmls=1;pmls<PMLS;pmls++)
```

```
{
    for(j=0;j<PMLS;j++)
    {
        TBY = *BY+BC2*(*(EZ+1)-*EZ);
        *HY = *HY* *HYX1 + *HYY1*TBY-*HYY2* *BY;
        *BY=TBY;
        EZ++;BY++;HY++;HYX1++;HYY1++;HYY2++;
    }

    for(j=0;j<grids;j++)
    {
        TBY = *BY+BC2*(*(EZ+1)-*EZ);
        *HY += *HYY1*TBY-*HYY2* *BY;
        *BY=TBY;
        EZ++;BY++;HY++;HYY1++;HYY2++;
    }

    for(j=0;j<PMLS;j++)
    {
        TBY = *BY+BC2*(*(EZ+1)-*EZ);
        *HY = *HY* *HYX1 + *HYY1*TBY-*HYY2* *BY;
        *BY=TBY;
        EZ++;BY++;HY++;HYX1++;HYY1++;HYY2++;
    }
}
for(i=0;i<gridn;i++)
{
    for(j=0;j<PMLS;j++)
    {
        *HY = *HY* *HYX1 + *HYX2* (*(EZ+1)-*EZ);
        EZ++;HY++;HYX1++;HYX2++;
    }

    for(j=0;j<grids;j++)
    {
        *HY += HC2*(*(EZ+1)-*EZ);
        HY++;EZ++;
    }

    for(j=0;j<PMLS;j++)
    {
        *HY = *HY* *HYX1 + *HYX2* (*(EZ+1)-*EZ);
        EZ++;HY++;HYX1++;HYX2++;
    }
}
for(pmls=1;pmls<PMLS;pmls++)
{
    for(j=0;j<PMLS;j++)
    {
        TBY = *BY+BC2*(*(EZ+1)-*EZ);
        *HY = *HY* *HYX1 + *HYY1*TBY-*HYY2* *BY;
        *BY=TBY;
        EZ++;BY++;HY++;HYX1++;HYY1++;HYY2++;
    }

    for(j=0;j<grids;j++)
```

```
        {
            TBY = *BY+BC2*(*(EZ+1)-*EZ);
            *HY += *HYY1* TBY-*HYY2* *BY;
            *BY=TBY;
            EZ++;BY++;HY++;HYY1++;HYY2++;
        }

        for(j=1;j<PMLS;j++)
        {
            TBY = *BY+BC2*(*(EZ+1)-*EZ);
            *HY = *HY* *HYX1 + *HYY1*TBY-*HYY2* *BY;
            *BY=TBY;
            EZ++;BY++;HY++;HYX1++;HYY1++;HYY2++;
        }
        TBY = *BY-BC2*(*EZ);
        *HY = *HY* *HYX1 + *HYY1*TBY-*HYY2* *BY;
        *BY=TBY;
        EZ++;BY++;HY++;HYX1++;HYY1++;HYY2++;
    }
}



/* The gateway routine */
void mexFunction(int nlhs, mxArray *plhs[],
                 int nrhs, const mxArray *prhs[])
{
  double *EZ,*HX,*HY,*DZ,*BX,*BXY,*BY;
  double *EZ2,*EZY1,*EZY2,*DZX1,*DZX2;
  double *HYX1,*HYX2,*HYY1,*HYY2;
  double *HXX1,*HXX2,*BXY1,*BXY2;
  double U0, HC2,BC2;
  int mrows,ncols,PMLS;

  /*                                                                  Inputs
EZ,HY,HX,DZ,BY,BX,BXY,EZY1,EZY2,DZX1,DZX2,HYX1,HYX2,HYY1,HYY2,HXX1,HXX2
,BXY1,BXY2,EZ2,HC2,U0,BC2,PMLS */

  /*  Check for proper number of arguments. */
  /* NOTE: You do not need an else statement when using
     mexErrMsgTxt within an if statement. It will never
     get to the else statement if mexErrMsgTxt is executed.
     (mexErrMsgTxt breaks you out of the MEX-file.)
  */
  if (nrhs != 24)
    mexErrMsgTxt("Twenty-four inputs required.");
  if (nlhs != 0)
    mexErrMsgTxt("Zero output required.");

  /* Get the scalar input */
  HC2 = mxGetScalar(prhs[20]);
  U0 = mxGetScalar(prhs[21]);
  BC2 = mxGetScalar(prhs[22]);
  PMLS = mxGetScalar(prhs[23]);
```

```
  /* Create a pointer to the input matrix */
  EZ = mxGetPr(prhs[0]);
  HY = mxGetPr(prhs[1]);
  HX = mxGetPr(prhs[2]);
  DZ = mxGetPr(prhs[3]);
  BY = mxGetPr(prhs[4]);
  BX = mxGetPr(prhs[5]);
  BXY = mxGetPr(prhs[6]);
  EZY1 = mxGetPr(prhs[7]);
  EZY2 = mxGetPr(prhs[8]);
  DZX1 = mxGetPr(prhs[9]);
  DZX2 = mxGetPr(prhs[10]);
  HYX1 = mxGetPr(prhs[11]);
  HYX2 = mxGetPr(prhs[12]);
  HYY1 = mxGetPr(prhs[13]);
  HYY2 = mxGetPr(prhs[14]);
  HXX1 = mxGetPr(prhs[15]);
  HXX2 = mxGetPr(prhs[16]);
  BXY1 = mxGetPr(prhs[17]);
  BXY2 = mxGetPr(prhs[18]);
  EZ2 = mxGetPr(prhs[19]);


  /* Get the dimensions of the matrix input */
  mrows = mxGetM(prhs[0]);
  ncols = mxGetN(prhs[0]);

  /* Call the C subroutine. */
  ezfdtd(EZ,HY,HX,DZ,EZ2,EZY1,EZY2,DZX1,DZX2,PMLS,mrows,ncols);
  hyfdtd(EZ,HY,BY,HYY1,HYY2,HYX1,HYX2,HC2,BC2,PMLS,mrows,ncols);
  hxfdtd(EZ,HX,BX,BXY,BXY1,BXY2,HXX1,HXX2,BC2,HC2,U0,PMLS,mrows,ncols);

}
```

TE Mode FDTD Library

The code utilized to perform the 2D TE mode (corresponds to the TM slab mode) FDTD calculations for this thesis is available for the Matlab environment. Please contact the author for a copy at tsuyoshi.yama@gmail.com.

APPENDIX C

TRAVELER FOR THE FABRICATION PROCESS

	Steps & Recipes	Expectations	Equipment	Recipe / Description	Run Status
0	Wafers out of the box			p-type 100 15-22ohm/cm^2	
1	Solvent cleaning: methanol, acetone, IPA. 30s each+ DI rinse between	Remove particles and organic contamination from wafer	General use fumehood		
2	Wet Oxidation	Grow >1um of oxide for isolation	Lindberg furnace tube 3	6hrs wet oxidation at 1175°C	
3	Measurement of oxide thickness	Thickness > 1um	Nanospec		
4	Growth of amorphous silicon	Grow 200-400nm of amophous silicon	Unaxis PECVD	TY_SI150.prc - 150°C	
5	Measurement of silicon thickness	Thickness at design thickness	Nanospec		
5	Spin E-beam resist (ZEP-520A)	~400nm of resist	Spinner in EBL facility	3000rpm / 60sec	
6	E-beam pattern writing	Write devices	E-beam Lithography	Shot pitch 5, 1nA or 2nA optimal current	
7	Pattern development	Development of pattern	Fume hood beside EBL	ZED-N50 developer (n-Amyl acetate) - 2min soak, IPA rinse	
8	Visual pattern check	Make sure pattern developed	Olympus microscope	Look for uniformity and roughness	
9	Coarse singulation of devices	Rough cut around patterns to make smaller pieces for further processing	Diamond scribe and tweezers		
10	Mounting of samples to carrier wafer (Plasmatherm ICP)	Mount in center for good uniform plasma etch	Hotplate, tweezers, cool greese	Mount on carrier wafers processed with thick oxide on Unaxis PECVD	
11	ICP Etching of silicon	Anisotropic etching of silicon	Plasmatherm ICP (left)	TGYSI.prc - Chlorine based Si etch, use nanospec to measure silicon	
12	15-30sec BOE etch	Undercut structure slightly for smoothing and isolation	General Uuse fumehood	Length of time depends on thickness of bottom oxide (~85nm/min etch rate BOE)	
13	Singulation of devices	Cleave devices	Diamond scribe and tweezers		
14	Resist removal	Remove the resist and any particles from the processes	Gasonic Asher	Recipe A : 1min	
15	Smoothing	Smooth surface	Plasmatherm ICP (left)	TY_SMTH.prc - Optional, can also be used to thin device	

APPENDIX D

JOBDECK FILE FOR EBL

```
;-----------------------------------------------------
 JOB/W  'YOSHI',4          ; 4 inch cassette
;-----------------------------------------------------

        PATH Yoshi
              ARRAY      (-18000,4,12000)/(0,1,0)
                        ASSIGN A(3) -> ((*,*))
              3: ARRAY   (0,2,764)/(0,1,0)
                        ASSIGN A(4) -> ((1,1))
                        ASSIGN A(7) -> ((2,1))
              4: ARRAY   (0,2,439)/(0,1,0)
                        ASSIGN A(6) -> ((1,1))
                        ASSIGN A(5) -> ((2,1))
              5: ARRAY   ( 0,1,0 )/( 750,4,500 )
                        ASSIGN  A(11) -> ((1,1))
                        ASSIGN  A(8) -> ((1,2))
                        ASSIGN  A(9) -> ((1,3))
                        ASSIGN  A(10) -> ((1,4))
              6: ARRAY   ( 0,2,182 )/( 3000,25,250 )
                        ASSIGN  P(1) -> ((1,1),SHOT1)
                        ASSIGN  P(2) -> ((2,10),SHOT5)
                        ASSIGN  P(2) -> ((2,12),SHOT5)
                        ASSIGN  P(2) -> ((2,14),SHOT5)
                        ASSIGN  P(2) -> ((2,16),SHOT5)
                        ASSIGN  P(1) -> ((1,25),SHOT1)
              7: ARRAY   ( 0,2,240 )/( 3000,25,250 )
                        ASSIGN  P(1) -> ((2,1),SHOT1)
                        ASSIGN  P(3) -> ((1,10),SHOT5)
                        ASSIGN  P(3) -> ((1,12),SHOT5)
                        ASSIGN  P(3) -> ((1,14),SHOT5)
                        ASSIGN  P(3) -> ((1,16),SHOT5)
                        ASSIGN  P(1) -> ((2,25),SHOT1)
              8: ARRAY   ( 0,1,0 )/( 75,4,50 )
                        ASSIGN  P(4) -> ((*,*),SHOT2)
              9: ARRAY   ( 0,1,0 )/( 75,4,50 )
                        ASSIGN  P(5) -> ((*,*),SHOT3)
              10: ARRAY   ( 0,1,0 )/( 75,3,75 )
                        ASSIGN  P(6) -> ((*,*),SHOT4)
              11: ARRAY   (0,1,0)/(75,2,150)
                        ASSIGN P(7) -> ((*,*),SHOT5)
              ARRAY   ( -4000,3,3500 )/( 4000,3,3500 )
                        ASSIGN  A(12) -> ((1,1),SHOT1)
                        ASSIGN  A(13) -> ((2,1),SHOT1)
                        ASSIGN  A(14) -> ((3,1),SHOT1)
                        ASSIGN  A(15) -> ((1,2),SHOT1)
                        ASSIGN  A(16) -> ((2,2),SHOT1)
                        ASSIGN  A(17) -> ((3,2),SHOT1)
                        ASSIGN  A(18) -> ((1,3),SHOT1)
                        ASSIGN  A(19) -> ((3,3),SHOT1)
```

```
            12: ARRAY   (0,10,100)/(0,10,100)
                        ASSIGN P(8) ->((*,*))
            13: ARRAY   (0,10,99)/(0,10,99)
                        ASSIGN P(9) ->((*,*))
            14: ARRAY   (0,10,100)/(0,10,100)
                        ASSIGN P(10) ->((*,*))
            15: ARRAY   (0,10,98)/(0,10,98)
                        ASSIGN P(11) ->((*,*))
            16: ARRAY   (0,11,90)/(0,11,90)
                        ASSIGN P(12) ->((*,*))
            17: ARRAY   (0,10,100)/(0,10,100)
                        ASSIGN P(13) ->((*,*))
            18: ARRAY   (0,24,43)/(0,27,37)
                        ASSIGN P(14) ->((*,*))
            19: ARRAY   (0,12,80)/(0,11,92)
                        ASSIGN P(15) ->((*,*))
            AEND
      PEND

;-----------------------------------------------------
;       Layer Definition
;-----------------------------------------------------

      LAYER   1
        P( 1 )  'Yoshi_SAW.v30'
        P( 2 )  'Yoshi_IN_ZEP.v30'
        P( 3 )  'Yoshi_OUT_ZEP.v30'
        P( 4 )  'Yoshi_PC20v2.v30'
        P( 5 )  'Yoshi_PC25v2.v30'
        P( 6 )  'Yoshi_PC30v2.v30'
      SPPRM 4.0,,,,1.0,1
      STDCUR  10;10nA
      SHOT1: MODULAT ((0,0))
      SHOT2: MODULAT ((0,250),(1,0))
      SHOT3: MODULAT ((0,250),(1,0))
      SHOT4: MODULAT ((0,250),(1,0))
      SHOT5: MODULAT ((0,0))

      Layer  2
        P( 8 )  'yoshi_10100.v30'
        P( 9 )  'yoshi_9099.v30'
        P( 10 )  'yoshi_8100.v30'
        P( 11 )  'yoshi_7098.v30'
        P( 12 )  'yoshi_6090.v30'
        P( 13 )  'yoshi_5100.v30'
        P( 14 )  'yoshi_43_37.v30'
      P( 15 )      'curt6030.v30'
      SPPRM 4.0,,,,1.0,1
      STDCUR  10;10nA
      SHOT1: MODULAT ((0,200))
      SHOT2: MODULAT ((0,300),(1,0))
      SHOT3: MODULAT ((0,300),(1,0))
      SHOT4: MODULAT ((0,300),(1,0))
      SHOT5: MODULAT ((0,50))

END
```

APPENDIX E

SCHEDULER FILE FOR EBL

```
MAGAZIN 'YOSHI'

#1
%4A
JDF     'yoshi',1
ACC 100
CALPRM '100kv_10na_0'
DEFMODE 2      ;2_stage deflection
RESIST 200
SHOT A,10
OFFSET (0,30000)

#1
%4A
JDF     'yoshi',1
ACC 100
CALPRM '100kv_10na_0'
DEFMODE 2      ;2_stage deflection
RESIST 200
SHOT A,10
OFFSET (0,17500)

#1
%4A
JDF     'yoshi',1
ACC 100
CALPRM '100kv_10na_0'
DEFMODE 2      ;2_stage deflection
RESIST 200
SHOT A,10
OFFSET (0,5000)

#1
%4A
JDF     'yoshi',1
ACC 100
CALPRM '100kv_1na_jan05'
DEFMODE 2      ;2_stage deflection
RESIST 200
SHOT A,10
OFFSET (0,-7500)

#1
%4A
JDF     'yoshi',2
ACC 100
CALPRM '100kv_1na_jan05'
DEFMODE 2      ;2_stage deflection
RESIST 200
```

```
SHOT A,10
OFFSET (-25000,-22500)

#1
%4A
JDF     'yoshi',2
ACC 100
CALPRM '100kv_1na_jan05'
DEFMODE 2      ;2_stage deflection
RESIST 200
SHOT A,10
OFFSET (0,-22500)

#1
%4A
JDF     'yoshi',2
ACC 100
CALPRM '100kv_1na_jan05'
DEFMODE 2      ;2_stage deflection
RESIST 2000
SHOT A,6
OFFSET (25000,-22500)

#1
%4A
JDF     'yoshi',2
ACC 100
CALPRM '100kv_1na_jan05'
DEFMODE 2      ;2_stage deflection
RESIST 2500
SHOT A,6
OFFSET (0,-37500)


END 1
```

REFERENCES

1 Richard P. Feynman, *QED, The Strange Theory of Light and Matter,* Penguin Books, London, (1990).

2. Yablonovitch, Eli. "Inhibited spontaneous emission in solid-state physics and electronics." *Physical Review Letters*, **58**, 2059 (1987).

3. John, Sajeev. "Strong localization of photons in certain disordered dielectric superlattices." *Physical Review Letters*, **58**, 2486 (1987).

4. Yang, Suxia, et.al. "Focusing of sound in a 3D phononic crystal." *Physical Review Letters,* **93**,. 024301 (2004).

5. Jeong, Taek Seong, et.al. "Experimental measurement of water wave band gaps." *Applied Physics Letters,* **85, 1**645 (2004).

6. Kittel, Charles. *Introduction to Solid State Physics*. 7th ed., New York: John Wiley & Sons, Inc., 1996.

7. Hummel, Rolf E. *Electronic Properties of Materials*. 3rd ed., New York: Springer-New York, Inc., 2001.

8. Smith, Glenn S. *An Introduction to Classical Electromagnetic Radiation*. Cambridge: Cambridge University Press, 1997.

9. Fink, Y. et al. "A dielectric omnidirectional reflector." *Science,* **282**, 1679 (1998).

10. Cregan, R. F. et al. "Single-mode photonic band gap guidance of light in air." *Science,* **285**, 1537 (1999).

11. Fleming, J. G., et.al. "All-metallic threedimensional photonic crystals with a large infrared bandgap." *Nature,* **417**, 52 (2002).

12 Mekis, A. *et al.* High transmission through sharp bends in photonic crystal waveguides. *Physics Review Letters,* **77**, 3787 (1996).

13 Fan, S. H., et. al. "Channel drop tunneling through localized states." *Physics Review Letters,* **80**, 960 (1998).

14 Johnson, S. G. et al. "Elimination of cross talk in waveguide intersections." *Optics Letters,* **23**, 1855 (1998).

15 Fan, S. H., et. al. "Waveguide branches in photonic crystals." *J. Opt. Soc. Am. B-Opt. Phys.,* **18**, 162 (2001).

16 Notomi, M., et. al. "Si-based photonic crystals and photonic-bandgap waveguides," *IEICE Trans. Electron*, **E85-C**, 1025 (2002).

17 Lin, S. Y., et. al. "Experimental demonstration of guiding and bending of electromagnetic waves in a photonic crystal," *Science,* **282**, 274-276 (1998).

18 Charlton, M.D.B, et. al, "Experimental Investigation of Photonic Crystal Waveguide Devices and Line-Defect Waveguide Bends," *Materials Science and Engineering B,* **74**, 17-24, (2000).

19 Meade, R.D., et. al. "Novel application of photonic band gap materials: Low-loss bends and high Q cavities," *Applied Physics Letters,* **75**, 4753-4755 (1994).

20 Smith, C.J.M., et. al. "In-Plane Microcavity Resonators with Two –Dimensional Photonic Bandgap Mirrors." *IEE Proc.- Optoelectron.*, **145**, 6, (1998).

21 Sabouroux, P., G. Tayeb, and D. Maystre. "Experimental and Theoretical Study of Resonant Microcavities in Two-Dimensional Photonic Crystals." *Optics Communications*, **160**, 33-36, (1999).

22 Y. Akahane, et.al. "Design of a channel drop filter by using a donor-type cavity with high-quality factor in a two-dimensional photonic crystal slab," *Applied Physics Letters,* **82**, 1341-1343 (2003).

23 Song, Bong-Shik, Susumu Noda, Takashi Asano, "Photonic Devices Based on In-Plane Hetero Photonic Crystals." *Science,* **300**, 1537, (2003).

24 W. Park and C. J. Summers, "Extraordinary Refraction and Dispersion in 2D Photonic Crystal Slabs", *Optics Letters***, 27**, 1397 (2002).

25 Wu, Lijun, et. al. "Superprism Phenomena in Planar Photonic Crystals." *Journal of Quantum Electronics*, **38**, 915-918 (2002).

26 W. Park and C. J. Summers, "Tunable Giant Refraction in Superlattice Photonic Crystal Waveguides Infiltrated with Liquid Crystal", *Applied Physics Letters,* **84**, 2013, (2004)

27 Kosaka, H. *et al."* Superprism phenomena in photonic crystals." *Physical Review B,* **58**, R10096 (1998).

28 Lin, S. Y., et.al. "Highly dispersive photonic bandgap prism." *Optics Letters,* **21**, 1771 (1996).

29 Wu, Lijun, Michael Mazilu, and Thomas Krauss. "Beam steering in planar-photonic crystals: From superprism to supercollimator." *Journal of Lightwave Technology*, **21**, 561-566 (2003).

30 Kosaka, Hideo, et. al. "Self-collimating phenomena in photonic crystals." *Applied Physics Letters*, **74**, 1212-1214 (1999).

31 Chen, Caihua, et. al. "Optimized bending efficiency of self-collimated beams in non-channel planar photonic crystal waveguides." *Optics Express*, **11**, 3153-3159 (2003).

32 Witzens, Jeremy, Marko Lončar, and Axel Scherer. "Self-collimation in planar photonic crystals." *IEEE Journal of Selected Topics in Quantum Electronic,* **8**, 1246-1257, (2002).

33 Yu, Xiafang. "Bends and splitters for self-collimated beams in photonic crystals." *Applied Physics Letters,* **83**, 3251-3253 (2003).

34 Prather, Dennis W., et.al. "Dispersion-based optical routing in photonic crystals." *Optics Letters*, **29**, 1, 50-52, (2004).

35 Pustai, David, et.al. "Analysis of splitters for self-collimated beams in planar photonic crystals." *Optics Express*, **12**, 9, 1823-1831, (2004).

36 Yamashita, T. and C. Summers. "Evaluation of self-collimated beams in photonic crystals for optical interconnect." *Journal of Selected Areas in Communication*, Accepted Sept. (2004).

37 Pendry, J. B. "Negative refraction makes a perfect lens." *Physical Review Letters,* **85**, 3966 (2000).

38 Notomi, M. "Negative refraction in photonic crystals." *Opt. Quantum Electron.* **34**, 133 (2002).

39 Luo, C. Y., et.al. "All-angle negative refraction in a three-dimensionally periodic photonic crystal." *Applied Physics Letters,* **81**, 2352 (2002).

40 Ashcroft, N. W. & Mermin N. D. "Solid State Physics." Saunders College, Philadelphia, (1976).

41 Yablonovitch, E., Gmitter, T. J. & Leung, K. M. "Photonic Band-Structure - the Face-Centered-Cubic Case Employing Nonspherical Atoms." *Physical Review Letters,* **67**, 2295 (1991).

42 Yablonovitch, E. and Leung, K. M. "Hope for Photonic Bandgaps." *Nature* **351**, 278 (1991).

43 Chelnokov, A., et. al. "Near-infrared Yablonovite-like photonic crystals by focused-ion-beam etching of macroporous silicon. *Applied Physics Letters,* **77**, 2943 (2000).

44 Blanco, A., E. Chomski, et. al. "Large-Scale Synthesis of a Silicon Photonic Crystal with a Complete Three-Dimensional Bandgap Near 1.5 Micrometeres." *Nature*, vol. 45, pp. 437-440, 2000.

45 Toader, O. & John, S. "Proposed square spiral microfabrication architecture for large three-dimensional photonic band gap crystals." *Science,* **292**, 1133 (2001).

46 Aoki, K. *et al.* "Microassembly of semiconductor three-dimensional photonic crystals." *Nature Materials,* **2**, 117 (2003).

47 Fleming, J. G. & Lin, S. Y. "Three-dimensional photonic crystal with a stop band from 1.35 to 1.95 microns." *Optics Letters,* **24**, 49 (1999).

48 Lin, S. Y. *et al.* "A three-dimensional photonic crystal operating at infrared wavelengths." *Nature,* **394**, 251 (1998).

49 Noda, S., Tomoda, K., Yamamoto, N. & Chutinan, A. "Full three-dimensional photonic bandgap crystals at near- infrared wavelengths." *Science,* **289**, 604 (2000).

50 Yamamoto, N., Noda, S. & Chutinan, "A. Development of One Period of a Three-Dimensional Photonic Crystal in the 5-10 μm Wavelength Region by Wafer Fusion and Laser Beam Diffraction Pattern Observation Techniques." *Japan Journal Applied Physics* **37**, L1052 (1998).

51 McNab, Sharee, Nikolaj Moll, and Yurii A. Vlasov. "Ultra-low loss photonic integrated circuit with membrane-type photonic crystal waveguides." *Optics Express*, **11**, 22, 2927-2939, (2003).

52 Joannopoulos, John D., Robert Meade, and Joshua Winn. *Photonic Crystals: Molding the Flow of Light*. New Jersey: Princeton University Press (1995).

53 Kasap, Safa O. *Optoelectronic and Photonis*. New Jersey: Prentice-Hall, Inc., (2001).

54 Sakoda, Kazuaki. *Optical Properties of Photonic Crystals*. W. Rhodes Ed. New York: Springer –New York, (2001).

55 Notomi, M. and T. Tamamura. "Direct Visualization of Photonic Band Structure for Three-Dimensional Photonic Crystals." *Physical Review B,* **61**, 11, 7165-7168, (2000).

56 Chan, C.T., Q.L. Yu, and K.M. Ho. "Order-N Spectral Method for Electromagnetic Waves." *Physical Review B*, **51**, 23, 16,635-16,642, (1995).

57 Taflove, Allen and Susan C. Hagness. *Computational Electrodynamics: The Finite-Difference Time-Domain Method*. 2nd ed., Boston: Artech House, Inc., (2000).

58 Qiu, Min and Sailing He. "FDTD Algorithm for Computing the Off-Plane Band Structure in a Two-Dimensional Photonic Crystal with Dielectric or Metallic Inclusions." *Physics Letters A,* **278**, 348-354, (2001).

59 Qui, Min. "Effective index method for heterostructure-slab-waveguide-based two-dimensional photonic crystals." *Applied Physics Letters*, **81**, 1163-1165 (2002).

60 Jonscher, A.K. *Dielectric Relaxation in Solids*. Chelsea Dielectrics Press Ltd., London, (1996).

61 Iizuka, Keigo. *Elements of Photonics*. vol. II, Wiley-Interscience, New York, (2002).

62 S. G. Johnson, S. Fan, P. R. Villeneuve, J. D. Joannopoulos, L. A. Kolodziejski, "Guided modes in photonic crystal slabs," *Physical Review B,* **60**, 5751-5758 (1999).

63 Verdeyen, Joseph T. *Laser Electronics* 3rd ed. Prentice Hall, Upper Saddle River, (1995).

64 Shin, S. Y. and L. B. Felsen, "Gaussian beams in anisotropic media," *Applied Physics Letters,* **5**, 239-250 (1974).

65 Fleck, J. A. Jr., and M. D. Feit, "Beam propagation in uniaxial anisotropic media," J. Opt. Soc. Am., **73**, 920-926 (1983).

66 Veselago, V. G. "Electrodynamics of Substances with Simultaneously Negative Values of Sigma and Mu." *Soviet Physics Uspekhi-Ussr,* **10**, 509 (1968).

67 Pendry, J. B. et. al. "Extremely low frequency plasmons in metallic mesostructures." *Physics Review Letters*, **76**, 4773 (1996).

68 Smith, D. R., et. al. "A composite medium with simultaneous negative permeability and permittivity." *Physics Review Letters*, **84**, 4184 (2003).

69 Shelby, R., D. R. Smith, and S. Schultz, "Experimental verification of a negative index of refraction." *Science*, **292**, 77 (2001)**.**

70 Vorckel, A., et. al. "Asymmetrically Coupled Silicon-On-Insulator Microring Resonators for Compact Add-Drop Multiplexers," *IEEE Photonic Technology Letters,* **15**, 921-923 (2003).

71 Mikulskas, I., et. al., "Fabrication of Photonic Strucutres by Means of Interference Lithography and Reactive Ion Etching," *Applied Surface Science*, **186**, 599-603 (2002).

72 Prodan, L. et. al. "Large-area two-dimensional silicon photonic crystals for infrared light fabricated with laser interference lithography." *Nanotechnology*, **15**, 639-642 (2004).

73 Divilansky, Ivan. et. al. "Fabrication of two-dimensional photonic crystals using interference lithography and electrodeposition of CdSe." *Applied Physics Letters*, **79**, 21, 3392-3394 (2001).

74 Frey, Wolfgang. et. al. "Ultraflat nanosphere lithography: A new method to fabricate flat nanostructures." *Advanced Materials*. **12**, 20, 1515-1519 (2000).

75 Businaro, L. et. al. "High-resolution complex structures for two-dimensional photonic crystals realized by x-ray diffraction lithography." *Journal of Vacuum Science Technology B*, **21**, 2, 748-753 (2003).

76 Dood, M. et. al. "Amorphous silicon waveguides for microphotonics." *Journal of Applied Physics*, **92**, 2, 649-653 (2002).

77 Schropp, Ruud E. I. and Miro Zeman. "New developments in amorphous thin-film silicon solar cells." *IEEE Transactions on Electron Devices*, **46**, 10, 2086-2092 (1999).

78 Campbell, Stephen A. *The Science and Engineering of Microelectronic Fabrication.* 2nd ed. New York: Oxford University Press, 2001.

79 "JBX 9300 FS Electron Beam Lithography System," JEOL USA, June 2005 http://www.jeolusa.com/eb/eblprods/jbx9300fs.html.

80 Hoekstra, Robert, et. al. "Microtrenching resulting from specular reflection during chlorine etching of silicon." *Journal of Vacuum Science Technologies B*, **16**, 4, 2102-2104 (1998).

81 Lee, Ju Hoon, et. al. "Study of shallow silicon trench etch process using planar inductively coupled plasmas." *Journal of Vacuum Science Technologies B*, **15**, 3, 573-578 (1997).

82 Choe, Jae Y., Irving P. Herman, and Vincent M. Donnelly. "Analysis of the etching of silicon in an inductively coupled chlorine plasma using laser thermal desorption." *Journal of Vacuum Science Technologies B*, **15**, 6, 3024-3031 (1997).

83 Astratov, V. N., et. al. "Photonic band-structure effects in the reflectivity of periodically patterned waveguides." *Physical Review B*, **60**, 24, 16255-16258 (1999).

84 Astratov, V. N., et. al. "Heavy photon dispersions in photonic crystal waveguides." *Applied Physics Letters*, **77**, 2, 178-180 (2000).

85 Coquillat, D., et. al. "Observations of band structure and reduced group velocity in epitaxial GaN-sapphire 2D photonic crystals." *Applied Physics B*, **73**, 591-593 (2001).